An Empirical Model for Mode-1 Internal Tides Derived from Satellite Altimetry: Computing Accurate Tidal Predictions at Arbitrary Points Over the World Oceans

by Brian D. Dushaw

Technical Memorandum
APL-UW 1-15
July 2015

Applied Physics Laboratory University of Washington
1013 NE 40th Street Seattle, Washington 98105-6698

NASA Grant NNX13AE27G

ACKNOWLEDGMENTS

This work was supported by grant NNX13AE27G (2013–2015) from the National Aeronautics and Space Administration. The farfield component of the Hawaiian Ocean Mixing Experiment and the deployment of the associated acoustic tomography arrays was supported by grants OCE-9819527 and OCE-9819525 from the National Science Foundation. The project for the tidal analysis of the altimetry data was initially supported by grant OCE-0647743 from the National Science Foundation. ONR grants N00014-09-1-0446 and N00014-12-1-0183 supported work on acoustics and acoustic tomography in the central North Pacific and Philippine Sea. Analysis of AMODE tides, barotropic and baroclinic, was supported by NSF grants OCE-9415650 and OCE-9720680. I am grateful to Z. Zhao for providing the estimates of internal tides from the IWAP program. P. Worcester and M. Dzieciuch provided the tomography data obtained in the Philippine Sea in 2009 and 2010–2011.

Questions concerning this report may be addressed to:

Brian D. Dushaw
Applied Physics Laboratory
University of Washington
1013 N.E. 40th Street, Seattle, WA 98105-6698
U.S.A.
(206) 543-1300

dushaw@apl.washington.edu

After 1 September 2015:

Brian D. Dushaw
The Nansen Environmental and Remote Sensing Center
Thormøhlens gate 47
Bergen, Norway
N-5006

brian.dushaw@nersc.no

This report was formatted in GNU groff version 1.22.2.

ABSTRACT

A global estimate for harmonic constants of mode-1 internal tides is described, enabling accurate predictions of internal tide amplitude and phase in most regions of the world's oceans. The estimates are derived from TOPEX/POSEIDON altimetry, building on a frequency-wavenumber tidal analysis technique described by Dushaw et al. (2011) [B. D. Dushaw, P. F. Worcester, and M. A. Dzieciuch, 2011. On the predictability of mode-1 internal tides, *Deep-Sea Res. I*, **58**, 677–698]. This technique obtains tidal harmonic constants for the six largest tidal constituents (M_2, S_2, N_2, K_2, O_1, K_1) and the first two internal wave modes simultaneously. The global solution requires reasonably accurate intrinsic properties of low-mode internal waves, which depend on local inertial frequency, stratification and depth. These properties are derived using the 2009 World Ocean Atlas and Smith–Sandwell global seafloor topography. To account for regional variations in internal wave properties, the global solution for internal tides is obtained by knitting together solutions obtained in 11°×11° overlapping regions. In any area of the ocean, the internal tide field generally consists of the interference pattern formed by the superposition of several or many wavetrains. Inasmuch as accurate tidal estimates are derived from the satellite altimetry, a remarkably marginal observational approach for determining properties of these waves, it is evident that the phases of the interference patterns are stable, indicating extraordinary temporal coherence. The timescales of the interference patterns are faster than the internal tide waves themselves. Over ocean basins, wavetrains traveling in particular directions can be determined, which show spatially coherent wavetrains extending across these basins and suffering little loss in amplitude. The global solution is tested against point-wise, along-track estimates for the internal tide, with satisfactory comparisons obtained between the two results. Along-track estimates are error prone, however, hence they provide for only a weak test. From the harmonic constants derived in the global solution, time series are predicted for several existing observations of mode-1 internal tides in the Atlantic and Pacific oceans. The clearest in situ measurements are provided by ocean acoustic tomography, but point measurements provided by moored thermistor arrays or mooring crawlers provide a complementary, if error prone, observation of mode-1 tides. Good predictability for both amplitude and phase, or as good as could be expected given the vagaries of ocean observation, is obtained in all cases. Some of these predictions are obtained for time series recorded about a decade before or after the altimetry data used to derive the global solution, consistent with extraordinary temporal coherence.

TABLE OF CONTENTS

LIST OF FIGURES

Global Estimated Internal Tides

Regional Estimates and Along-track Solution Testing

Predictions for Comparison to Observed Time Series of Mode-1 Amplitude

ELECTRONIC SUPPLEMENTS (DRAFT)

This report includes supplemental materials comprising the global internal tide estimates, associated digital data, and example software for how to read and compute the digital data sets. The data files and software scripts rely on the use of the Matlab software package. The supplemental materials are freely available from the URL http://www.apl.uw.edu/tm115. As of this writing, Version 1.1 of this report, this supplemental material is preliminary and will likely continue to evolve to become more user friendly.

The supplemental material consists of:

(1) This PDF document, 20 MB.

(2) A set of animations.

(3) A set of time series of acoustic tomography measurements, perhaps 30 small files. The tomography time series of internal tide estimates have not been previously readily available.

(4) The global estimates for modes 1 and 2 internal tides. These are large data files. About 10 Matlab data files totaling about 2 GB. These files can be used to compute harmonic constants for the tidal constituents, hence also compute tidal predictions.

(5) Global internal tide properties determined using the 2009 World Ocean Atlas, 9.2 MB, including wavelength sea-surface height, phase speed, group speed, equivalent depth, and energy density for M_2, S_2, O_1, and K_1 frequencies and for modes 1 and 2. This is a Matlab data file.

(6) Small Matlab scripts to illustrate how to read and plot those data. The Matlab script that was used for computing internal tide modes from the NOAA World Ocean Atlas.

PROLOGUE

I began my graduate research in oceanography in the late 1980s with the Acoustical Oceanography Group at the Scripps Institution of Oceanography led by Walter Munk and Peter Worcester. Munk put me to work examining the signals of barotropic tidal currents recorded during the 1987 Reciprocal Tomography Experiment (RTE87). The problem of tidal signals in deep-ocean acoustic transmissions dates to at least 1974 (Weinberg et al. 1974, Dyson et al. 1976, Munk et al. 1981, Headrick et al. 1993). In 1987 the ability of reciprocal tomography to measure currents was unknown, and the tides were a convenient way to test these measurements. Estimating these currents requires computing the difference in the travel times of reciprocal rays, and it was not known whether the properties of long-range acoustic propagation allowed for sufficient precision for the signals of currents to be obtained. It was quickly apparent that the differential travel times were extraordinarily accurate, with quite good comparisons between estimated tidal current harmonic constants and those computed from the Schwiderski tidal model from the mid-1980s (Dushaw et al. 1994a, 1995). The precision stemmed from the stability of the reciprocal rays, so that the internal wave fluctuations of temperature along the two ray paths cancelled almost identically when the travel time differences were computed. Pairs of reciprocal ray paths, i.e., the paths followed by oppositely traveling acoustic signals, separate by less than internal wave correlation length, even over O(1000 km) ranges, giving nearly identical contributions from those fluctuations to the two rays. Without this property, the temperature fluctuations of internal waves would overwhelm the small current signals. Reciprocal tomography provides the most accurate measure of tidal current available (Dushaw et al. 1994b, Dushaw et al. 1997, Stammer et al. 2014). The measurement qualities of the tomography ray paths are ideally matched to large-scale barotropic currents. Conversely, the comparisons between tomographic measurements and present-day numerical ocean models for tides have shown that the tidal currents predicted from these models are remarkably accurate, at least in the open ocean.

Corresponding to the differential travel times, the sum of reciprocal travel times were also computed. This quantity isolates the signals of temperature variations from those of currents. The dominant variations from temperature are caused by the mesoscale, or in the case of the RTE87 experiment, the seasonal cycle as the upper ocean of the central North Pacific warmed as summer progressed. These low-frequency signals were 100–200 ms in travel time. Surprisingly, the high-frequency travel time variations (frequencies greater than about 0.5 cpd) computed from the RTE87 data showed tidal variations as well, with signals similar to the differential travel times. These tidal variations were coherent in time. At one of our weekly group meetings discussing these data, Munk declared "internal tides are not phase-locked" (ca. 1990); the signals were a puzzle. After extensive diagnostic studies, it was apparent that the signals were real. One danger was that there were errors in the required corrections for mooring motion, since moorings often move in response to tidal current, but there were no apparent problems with that analysis. Further, travel time variations corresponding to the ray traveling near the sound channel axis, rather than deep-turning rays, were significantly larger. Mooring motion corrections affect all travel times equally to first order. The larger signal of the near-axis ray occurred because this ray traveled greater distances through depths where the mode-1 temperature amplitude was largest. These observations were the first of the radiation of coherent internal tides far into the interior of the North Pacific from the Hawaiian Ridge and the Aleutians (Dushaw et al. 1995b). This property had been foreshadowed by an analysis of Mid-Ocean Dynamics Experiment (MODE) data by Hendry (1977) (see also Hendershott 1981) in the North Atlantic some 20 years earlier. While Hendry made a careful examination of the coherence of the tides with the MODE data, these data were not of sufficient quality or record length to discern the extraordinary coherence of the mode-1 internal tides. It may be worth noting that the 6–7°C large-scale warming of the upper ocean during summer 1987 apparently had little effect on the coherence of the observed tidal signals. Indeed, the coherence of the internal tide signals was almost as great as that for the barotropic tidal currents. The clarity of the tidal signal in the tomography data arises for the same reason the barotropic tide signal is so great: the acoustic rays sample the large-scale, depth average, hence these measurements are a natural filter for the temperature expression of the lowest internal wave mode. The interpretation of the tomographic measurements has remained unchanged and unchallenged for the past 20 years.

INTRODUCTION

This report describes a global solution for the mode-1 internal tides, enabling these tides to be predicted at arbitrary points and times in most regions of the world's oceans. This solution is derived from TOPEX/POSEIDON (T/P) sea surface height (SSH) measurements using the frequency-wavenumber tidal analysis described by Dushaw et al. (2011). That publication is a prerequisite to this report. The report begins with the prologue above for two reasons. First, the discovery of the radiation of the coherent internal tide waves far into the ocean's interior was through employing acoustic tomography (Dushaw et al. 1995b). The well-known result by Ray and Mitchum (1996, 1997) was not unrelated. Second, as discussed by Dushaw et al. (2011), quality, unambiguous in situ measurements of mode-1 internal tides are difficult to obtain. Moored observations employing thermistors or current meters have difficulty resolving a clear mode-1 signal. Such observations even have difficulty accurately resolving the simplest of all oceanographic signals, the barotropic tidal currents (Stammer et al. 2014). Any claim for the ability to predict the mode-1 internal tides from a model, requires a means of testing those predictions. Measurements by acoustic tomography provide a clear, unambiguous measurement of this tidal variability, hence these measurements can be used to test model predictions.

One apparent controversy about these internal waves concerns their degree of temporal coherence. For example, even though the tidal variations observed by tomography over the 120-day record length of the RTE87 experiment exhibited extraordinary coherence, an anonymous reviewer of the 1995 tomography paper challenged the notion of coherent internal tides. A quantitative measure of that coherence indicated that any temporal variations in tidal phase of that time series were less than could be determined by the available record length (Dushaw et al. 1995b). Despite mounting evidence that these tide waves are extraordinarily coherent (referring solely to mode-1 waves), the belief that these waves have a significant, but unobservable, "incoherent component" seems to persist (Zhao et al. 2010; Ray and Zaron 2011; Zaron and Egbert 2014). This belief has been starkly contradicted by the coherence of mode-1 internal tides as observed by acoustic tomography (Dushaw et al. 1994a, Dushaw et al. 1995a, Dushaw et al. 1995b, Dushaw and Worcester 1998, Dushaw 2000, Dushaw 2003, Dushaw et al. 2006, Dushaw et al. 2011, Philippine Sea observations reported here). It is obvious that some degree of incoherence is induced by mesoscale variations (e.g., Zaron and Egbert 2014) and other effects, but the overall evidence still indicates such incoherence is so small as to render incoherent contributions perhaps inconsequential. Even though the belief in the "incoherent component" to the mode-1 internal tides has persisted for at least 20 years, no clear measured examples of this property are available. At the very least, a clearer definition as to what is meant by incoherence is required; there are widely varying perceptions of the degree of incoherence. The issue is complicated by the challenge of obtaining clear, unambiguous measures of mode-1 signals. An analysis of data from the Internal Waves Across the Pacific project concluded that mode-1 internal tides were incoherent beyond several hundred kilometers north of the Hawaiian Ridge (Zhao et al. 2010), for example, but, as will be discussed below, this conclusion was incorrect. By general scientific principles, before someone can claim the existence of some phenomena, such as the "incoherent component", there should be some evidence for its existence.

The extraordinary spatial and temporal coherence of mode-1 internal tides stems from their basic physical properties: phase speed and wavelength; these are fast, large-scale waves. Semidiurnal internal tides have a phase speed of about 3.5 m/s, which is much faster than any ordinary ocean variability. A frequent misunderstanding concerns the Doppler shift, which has sometimes been cited as a means by which tidal phase is distorted. A moving medium cannot induce a Doppler shift; a moving source or receiver is responsible for this phenomena. (An accelerating medium can induce a Doppler shift.) The wavelength of semidiurnal internal tides is 150–160 km, while diurnal internal tides have wavelengths of 100's of km. Thus, their wavelengths are larger than the typical mesoscale. Rainville and Pinkel (2006) used ray tracing methods to determine the trajectories of mode-1 internal tides through a mesoscale environment determined by satellite altimetry. They found that, "the path of mode 1 is only slightly affected by typical [mesoscale] currents, although its phase becomes increasingly random as the propagation distance from the source increases." But in this case the wavelength of the radiation is larger than the scales of the variations, which is a violation of the basic assumptions of geometric ray theory. Ray theory is a high-frequency, high-wavenumber approximation. The study of Zaron and Egbert (2014) was partly intended to remedy this particular issue. The effects of the mesoscale variations on semidiurnal mode-1 properties were determined by Dushaw (2002), who used a 12-year time series of monthly hydrographic measurements obtained by the Hawaiian Ocean Time Series (HOT) program 100-km north of Oahu. At the point of the HOT measurements, the mode-1 and mode-2 phase speeds were determined to be 3.26 ± 0.08 and 1.71 ± 0.04 m/s, respectively, values that give the mean and RMS of the mode-1 phase speed over the 12 year duration. Even at this single point, the variations in phase speed were only a few percent (with these values likely overestimated by the perennially limited, noisy hydrographic data). Moreover, the actual effects of variations determined at a single point on phenomena with a wavelength larger than the mesoscale are likely to be reduced considerably.

THE INTERPRETATION OF BEAMS

In many ways, one's perception of the coherence or incoherence of mode-1 internal tides depends on how one interprets the apparent internal-tide "beams", or the narrow, filamental regions of large internal-tide amplitude that extend great distances into the ocean's interior. Numerous papers have noted these beams, with the interpretation that these are stand-alone jets of large amplitude that emanate from specific points of topography where large internal tides are generated. From this perspective, both coherent and incoherent elements can contribute to this beam; the degree of coherence cannot be determined by the available data.

A moment of contemplation will lead one to disregard this interpretation, however. Specifically, there is no physical mechanism by which a beam can be confined to a narrow geometry in this interpretation. Waves that are generated at specific "hot spots" emanate as circular waves.

An example of this type of wave can be seen in this report in the southward propagating wavetrain that emanates as ever-expanding circular waves from a specific point in the Aleutian Islands. Isolated narrow beams of large amplitude are not possible by ordinary linear wave theory.

A more physical interpretation is that these so-called beams are an artifact of the interference of many wavetrains. Along such topographic features as the Hawaiian Ridge, wavetrains are generated at many locations with similar initial phase. As these waves radiate from disparate locations they overlap and interfere to form beams. A simple superposition of three monochromatic wavetrains illustrates how these beams may be formed (Figure 1). Rainville et al. (2010) provided an analysis of beams emanating south from the Hawaiian Ridge by the superposition of several independent wavetrains. A similar example of this phenomena is that of wave patterns of tsunamis that span the Pacific basin (Figure 2). The filamental patterns of the tsunami wavetrains are a product of wave interference; no one would ever claim these features to be beams of tsunami energy.

The interpretation of a beam as an interference effect, rather than an isolated phenomena, is more than just an incidental nuance. For these beams to exist as observed, extraordinary wave coherence is required, not just in the constituent waves themselves, but also in their interference patterns, that is, the *differences* between the phases of the underlying waves must be stable. As observed by altimetry, the interference patterns around the Hawaiian Islands have been stable for decades. In particular, the phase information of wavetrains emanating from the Aleutians interfering with wavetrains radiating northward from Hawaii to form standing waves is readily determined, even after these wavetrains have crossed the Pacific basin. When one considers that these interference patterns are recovered using the altimetry data, even with weak signal (near zero SNR) and sparse 10-day repeat cycle, the extraordinary coherence of these wavetrains is readily apparent. The interference pattern is one of the most sensitive and unstable phenomena in nature. If the mode-1 internal tide had the sort of incoherent component that has often been suggested, the resulting interference patterns would be thoroughly unstable, rendering the internal tide unobservable by altimetry.

It has been common in the literature to depict the internal tide waves by their energy flux vectors, with images of complicated flows of energy and large energy fluxes within the internal tide beams. While these results are not entirely wrong, they are not entirely right either. When energy fluxes are computed in this point-wise fashion, a complicated pattern of energy fluxes results, even though the wave field may result from a simple interference pattern of a few monochromatic waves (Figure 1). The complicated pattern of energy flux vectors is not physical. Just as one would not usually compute energy fluxes that varied in time as a consequence of the interference of multiple tidal frequencies, energy fluxes that vary in space from the interference of multiple wavenumbers are not entirely physical. This issue is described further in a section below. In Figure 1, there are only three energy flux vectors.

An acoustic analogy may provide an alternative illustration of the point. Consider a vertical line of acoustic sources that have been programmed to transmit signals that form an acoustic beam. The essential aspect of such a beam is that the acoustic signals are coherent and with just the right phases so that the acoustic waves from the various sources superimpose constructively to form the beam. The beam arises from a consipiracy of phases in the interfering spherical waves that emanate from the acoustic sources. Suppose, on the other hand, one had tried to save money and bought bargain acoustic sources that turned out to be flawed such that the individual sources were only about 80% coherent. With these flawed sources, a stable acoustic beam would be impossible to obtain. Rather, the beam would be poorly defined and fluctuate randomly in space. Internal tide beams are formed in a similar manner, and the sort of "incoherent component" commonly discussed in the literature would necessarily lead to unstable beams. If such unstable beams were observed by altimetry with 10-day repeat cycle, they would be indistinguishable from random noise. The observations show quite narrow, well-defined, stable beams, however, which argues for extraordinary coherence.

With this interpretation of the mode-1 baroclinic tidal field, together with the results described in this report and in Dushaw et al. (2011), the analysis and conclusions of Tian et al. (2006) appear less than conclusive. In the Tian analysis, the altimetry data were used to determine tidal energy fluxes, from which the mixing rate caused by the M_2 internal tide in the upper ocean was estimated. However, the energy fluxes were computed spatially only coarsely, which makes little sense for a tidal field composed of regions of large and small amplitude as a consequence of interference effects. Further, the gradients of these fluxes were then computed to obtain dissipation estimates, a dubious proposition under the circumstances. As noted by Dushaw et al. (2011) and below, no apparent or obvious change in the internal tide radiation is apparent near the 30° latitudes where Tian et al. (2006) reported enhanced mixing.

The interpretation of the internal tide field as an extraordinarily coherent superposition of many interfering waves is the primary motivation, and justification, for the kinematic tidal model discussed next. This model for the internal tide waves is constructed as a general linear superposition of a near-continuum of waves. Inverse techniques, otherwise known as weighted least squares, are then employed to fit this general model to the available data to obtain optimal solutions, or estimates, for the internal tide wave field.

KINEMATIC TIDAL MODEL

The frequency-wavenumber tidal analysis described by Dushaw et al. (2011) is a *kinematic* tidal model in the sense that it obtains a spatially continuous fit to a complicated, but linear, traveling wave field, without regard to dynamics. To that end, the model consists of a superposition of a large number of traveling plane waves. The origins of the model are in the preliminary mapping calculation of Dushaw (2002), where a number of self-inconsistencies with the along-track tidal harmonic constants were identified. In particular, when tidal harmonic constants are obtained point-wise along the altimeter tracks, harmonic constants obtained at the same point, but from ascending or descending tracks, often disagree significantly. The 2002 analysis was, in turn, done in response to the monochromatic wave result of Ray and Cartwright (2001). Contemplating objective mapping techniques commonly employed for analysis of acoustic tomography data, it was clear to me that a more systematic, objective approach to deriving the internal tide fields was possible. A frequency-wavenumber tidal analysis resolves the issues or technical problems identified by Dushaw (2002). The frequency-wavenumber tidal analysis has caused some confusion in some quarters (e.g., Zhao et al. 2012, Zaron and Egbert 2014, and others). The approach is a close cousin to ordinary objective mapping techniques, or to the problem of fitting arbitrary functions by Fourier series. In the present case, the basis functions used for the fit are traveling waves with tidal frequency and wavenumbers near the theoretically expected wavenumbers. The topic of wavenumbers is described below. The mapping technique is only briefly reviewed here; see Dushaw et al. (2011) for a more thorough discussion. See also Wunsch and Stammer (1995) and Wunsch (2010).

In addition to resolving the technical inconsistencies discussed by Dushaw (2002), the frequency-wavenumber analysis has a number of advantages over the "wavelet" approach of Zhao and Alford (2009), Zhao et al. (2012) (a technique based on the original analysis of Ray and Cartwright (2001)). The basis functions employed adhere to the dispersion relation for mode-1 internal tide waves, hence the resulting solution does as well. One positive aspect of this approach is therefore the elimination of the persistent problem of aliasing of mesoscale variability into the tidal solution (Arbic et al. 2012). (With a 10-day repeat cycle, tidal variability measured at a point is indistinguishable from 60-day mesoscale variability.) This point is discussed further below. All tidal frequencies are simultaneously included in the fit, thus reducing the chance of noise from the cross-talk of signals from nearby tidal frequencies. The objective analysis is designed to obtain a continuous, self-consistent solution. The continuous solution, including all major tidal frequencies, is ideal for obtaining tidal predictions at arbitrary points and times (including for obtaining tidal predictions for line-averaged data); the solution is designed to obtain interpolated values that are consistent with the observations. With the discontinuous, local approach of Zhao and Alford, interpolated estimates are not likely to be consistent with the original observations. Indeed, the interpretation of the internal tide described above, together with the approach to analysis described by Dushaw et al. (2011) and in this report, has led to the only available accurate predictions for mode-1 internal tides as of this writing.

In this kinematic model for the analysis of the altimeter data for the internal tide, the sea-surface height at any point and time (x_i, t_j) is modeled as,

$$\eta(x_i, t_j) = \sum_{n,m=1}^{N,M} f_n(t_j) A_{n,m} \cos(\omega_n t_j - k_m \cdot x_i - G_{n,m} + (V_{0n} + u_n(t_j))) + \varepsilon \qquad (1)$$

for frequencies ω_n and wavenumbers k_m. The lunar node factor f_n, and equilibrium argument $V_{0n} + u_n$ associated with each tidal frequency (e.g., Schureman 1958) are included explicitly. The analysis thus treats wavenumber and frequency on an equal basis, with a simultaneous fit in both time and space. The weighted least squares fit is made to the along-track altimeter data to derive the harmonic constants for each wavenumber and frequency. Six tidal frequencies, four semidiurnal and two diurnal, were included. The Appendix describes some of the computational details. The choice of wavenumbers used in the fit is discussed in the next section. From such a solution, harmonic constants for any constituent, or predictions for time series of sea-surface height, at any point can be derived. For example, to derive harmonic constants $A_{M_2}(x)$ and $G_{M_2}(x)$ for the M_2 internal tide at position x, set

$$\eta_{M_2}(x, t) = A_{M_2}(x)\cos(\omega_{M_2} t - G_{M_2}(x)) \qquad (2)$$

$$= A_{M_2}(x)\cos(G_{M_2}(x))\cos(\omega_{M_2} t) + A_{M_2}(x)\sin(G_{M_2}(x))\sin(\omega_{M_2} t)$$

equal to (1), using only the M_2 solution for the $A_{n,m}$ and $G_{n,m}$. Set $\omega_{M_2} t = 0$ to obtain the cosine component harmonic constant, or $\omega_{M_2} t = \pi/2$ to obtain the sine component.

To be padantic about the meaning and implementation of Equation (1), the process is, in principle, no different than fitting the equation for a line, $y = mx + b$, to data. This simple model can be fit to data to estimate the two parameters m and b. Once those estimates are obtained, it is a simple matter to "predict" the value for y for any given value of x. The kinematic model is different only in that it has a large number of unknown parameters, but it remains a linear model. The model is fit to the altimeter data by least squares to estimate values for the parameters A and G. Once those parameters are found, it is a simple matter (although a challenging bookkeeping problem) to obtain a prediction for η for any given values x and t. The process is, in principle, little different than ordinary tidal prediction.

GLOBAL PROPERTIES OF INTERNAL TIDES

Application of the kinematic model to obtain global estimates for the mode-1 internal tides requires accurate values for the relevant internal wave properties. Two specific quantities that are required are the internal tide wavelength and the relation between sea surface height and internal displacement, that is, the relation between SSH and internal mode amplitude. A number of other properties are also useful, including the phase speed and energy density associated with the internal wave modes. As summarized below, the relevant quantities determining local properties are stratification (buoyancy), ocean depth, and latitude (see also Chelton et al. 1998). The large impact of ocean depth on these properties is apparent, but stratification plays an equally important role. Figure 11 shows the global ocean depths as determined by the Smith-Sandwell version 8.2 topographic atlas (Smith and Sandwell 1997). Global stratification was determined by the 2009 World Ocean Atlas (Antonov et al. 2010, Locarnini et al. 2010). As noted above, variations in mode properties caused by the mesoscale are minimal. As discussed in the next section, some spread in wavenumber values is employed to account for deviations from local climatology from the World Ocean Atlas estimates and other effects. Insofar as acoustic propagation is concerned, a phenomena not dissimilar from internal wave mode propagation, the properties of the World Ocean Atlas more accurately encompass the conditions of propagation than most numerical ocean models (Dushaw et al. 2013).

Theory

The analysis described in this report employed the description of internal tide modes given by Hendershott (1981). For the sake of convenience, the basic equations are restated here (the notation is the same as Dushaw et al. 1995). The displacement modes of the internal tide are given by solutions to the eigenvalue problem with tidal frequency ω:

$$\frac{d^2F(z)}{dz^2} + q^2(N^2(z) - \omega^2)F(z) = 0, \tag{3a}$$

with the bottom and free surface boundary conditions

$$F(D) = 0 \qquad\qquad \frac{dF(0)}{dz} - gq^2F(0) = 0, \tag{3b}$$

where q^2 is the eigenvalue, $N(z)$ is the buoyancy frequency, D is the ocean depth, and g is the gravitational acceleration. The eigenvalues and eigenfunctions were determined using Matlab computer code employing Numerov's method (Jensen et al. 1994). The surface boundary condition determines the surface expression of the internal tide modes, of course; this constraint determines the internal displacement from the surface signal observed by altimetry. The solutions to the differential equation are a linear superposition of a set of eigenfunctions, or modes, $F_n(z)$ with eigenvalues q_n^2. Here,

$$q_n^2 = \frac{k_n^2}{\omega^2 - f^2}, \tag{4}$$

where k_n is the mode n wavenumber, ω is frequency, and f is the inertial frequency. The internal tides are evanescent above the latitude where $\omega = f$, which implies the diurnal tides do not freely propagate above about 30°N. The eigenvalues can also be written as $q_n^2 = 1/(gD_n)$, where D_n are the baroclinic depths equivalent to the barotropic depth, D, with $D_n \ll D$ (Hendershott, 1981). Because $N^2 \gg \omega^2$, the frequency dependence can be ignored and the $F_n(z)$ are independent of ω. The displacement at frequency ω_p, where $\{ \omega_p \}$ is the set of tidal constituent frequencies, is represented as

$$\zeta_p(x, t) = \sum_{n=1}^{n=\infty} A_{pn} F_n(z) \exp i(k_{pn} \cdot x - \omega_p t + \phi_{pn}). \tag{5}$$

and the total internal tidal displacement is the sum of ζ_p over p. The ϕ_{pn} is the phase of the nth mode at frequency ω_p. The displacement modes $F_n(z)$ are normalized according to the expression

$$\int_D^0 F_n^2(z) N^2(z) dz = D\bar{N}^2, \text{ where} \tag{6a}$$

$$\bar{N} = \frac{1}{D} \int_D^0 N(z) dz. \tag{6b}$$

With this normalization, the amplitude of the internal tide mode is roughly equivalent to the maximum internal displacement of the mode.

The temperature and sound speed modes are obtained by multiplying the displacement modes by the negative of the potential temperature or sound speed gradient, respectively. Thus,

$$T_n(z) = -F_n(z) \frac{d\theta(z)}{dz} \tag{7}$$

$$C_n(z) = -F_n(z) \frac{dc_\theta(z)}{dz,} \tag{8}$$

where $\theta(z)$ is the potential temperature and $c_\theta(z)$ is the potential sound speed. These modes determine the temperature or sound speed signals associated with the internal tide displacements. Tidal signals observed by a thermistor are therefore dependent on the potential temperature gradient local to the instrument.

The baroclinic current modes are given by,

$$U_{pn}(z) = \left(\frac{\omega_p}{k_{pn}} \right) \frac{d}{dz} F_n(z). \tag{9}$$

Although baroclinic currents are not discussed in this report, it may be noted that the ability to predict mode-1 surface or displacement signals necessarily implies that the currents associated with these signals can also be predicted.

Energy

With displacement determined by the product of the mode amplitudes with the vertical mode functions, the potential energy for the nth mode is

$$PE = \frac{1}{2}\int_D^0 \rho(z)N^2(z)(A_nF_n(z))^2dz. \qquad (10)$$

Average values for potential energy are typically obtained from time series, which for a simple sinusoid introduces another factor of 1/2. Since the ratio of potential energy to kinetic energy is to good approximation $(\omega^2 - f^2)/(\omega^2 + f^2)$, the kinetic energy follows directly. For plane waves, the energy flux is the energy density times the group velocity.

The eigenvalue equation (3) was solved for the world's oceans at one-degree resolution, corresponding to the World Ocean Atlas resolution, using the major tidal frequencies. From these global solutions, mode-1 wavelengths (Figures 11–13), phase speeds (Figures 14–16), group speeds (Figures 17–19), sea-surface height associated with unit mode amplitude (Figure 20–22), equivalent depths (Figure 23–15), and energy density associated with unit mode amplitude (Figures 16–18) were computed. The same quantities were computed for mode 2 as well (Figures 29–34). The theoretical wavelengths were used to adapt the kinematic model to match local conditions. The sea-surface height values estimated from altimetry data can be used to determine mode amplitude. Inferred values for mode amplitude can then be directly used to determine internal tide energy density from the pre-computed energy density maps.

The theoretical solutions appear to accurately correspond to in situ ocean conditions. In comparisons between the altimetric estimates and acoustic tomography, the quantities of SSH, mode amplitude, or acoustic travel time can be used interchangeably, for example. Each quantity stems from the same internal tide displacement, and they equivalently determine this displacement.

The global maps of Figures 11–34 show that mode properties vary considerably, depending on depth and stratification. Mode wavelength gets longer at higher latitudes, of course; semidiurnal turning latitudes are around 75°. A large region in the Southern Ocean southwest of South America with quite different mode properties than surrounding waters may correspond to "mode water" that is present there (S. Gille, personal communication 2014); weaker such effects seem apparent south of the Gulf Stream and Kuroshio. Figure 52 shows that the SSH associated with unit mode amplitude varies considerably, with much weaker SSH signal at higher latitudes. This decrease in signal has been mistaken for mode decay (Dushaw et al. 2011), but it is a simple effect from stratification. Mode-2 properties vary differently than mode-1 properties, e.g., wavelength, because these modes are sensitive to different stratification properties in depth.

AN OPTIMIZED CHOICE OF WAVENUMBERS

While the least-squares fit of the kinematic model to the altimeter data is an "objective analysis", the precise choice of wavenumbers employed for the model affects the quality of the solution. The solution is tempermental to the set of wavenumbers employed, which is not surprising given the weak SNR of the data and the less than optimal temporal sampling. As noted by Dushaw et al. (2011), stronger assumptions for the model lead to better, more robust solutions, but only if those assumptions are correct. The wavenumbers used here were chosen to be near the theoretical semidiurnal O(1/150 km^{-1}) and diurnal O(1/500 km^{-1}) wavenumbers. To account for errors in climatology, the modest influence of the mesoscale on mode properties, variations of latitude and depth, and other such effects, it was desireable to use a wavenumber model that is a narrowband, rather than a line, spectrum. Physically, the width of this spectrum is also determined by internal tide incoherence, which is likely to be quite small. The choice of wavenumber spectrum in practice is by trial and error, together with physical intuition. Quantitative criteria for determining which particular wavenumber set works better than others are challenging to define, but two available data sets are the point-wise, along-track estimates, and the in situ time series obtained by thermistors or acoustic tomography. The along-track estimates are error prone, however, hence these estimates hardly comprise a "gold standard" measurement. Similarly, determining the internal tide from thermistors is also error prone, given the difficulties in obtaining a high-quality resolution for the individual modes from these data. Nevertheless, by trial and error a reasonably effective selection for wavenumbers is possible.

In these tests and in the global solution for internal tides reported here, 7 years of the T/P record spanning 2001–2007 were used for the frequency-wavenumber tidal analysis, together with the T/P tandem track data. The available records for this project span 1992–2008; the tandem track record spans 2002–2005. Point-wise, along-track harmonic constants were determined using the entire record length; the different record lengths employed for the two analyses may account for some of the observed differences between them. As noted by Dushaw et al. (2011), a three-year record length is the minimum for determining tidal harmonic constants at a point in the altimeter data.

The process of testing solutions against the available data leads to quite narrow widths for the spectrum (Figure 3). Four sets of wavenumbers are employed. From large to small wavenumber, these sets are: mode-2 semidiurnal, mode-1 semidiurnal, mode-1 diurnal, and barotropic. These sets of wavenumbers are also frequency dependent, of course, hence each tidal frequency is associated with its own wavenumbers. Nominal wavenumbers for the barotropic tides were used to account for any residual tidal variability stemming from errors in the barotropic tide model used to remove these signals. The AVISO altimeter data were employed (http://aviso.oceanobs.com/; Dibarboure et al. 2009, Dushaw et al. 2011); the barotropic tide signals are preremoved from these data using a global tidal model. The set of wavenumbers was omnidirectional, as indicated in Figure 3. To maximize the number of directions encompassed by the spectrum, a "twist" in wavenumber directions within the band was employed, though the actual effectiveness of this scheme is likely marginal. Solutions that optimally match both along-track estimates and acoustic tomography measurements require a very narrow band spectrum. (A line-spectrum model produces poor results, however.) In this global solution, the assumed semidiurnal, mode-1 wavenumber width was ±4% of the theoretical wavelength, while the semidiurnal, mode-2 wavenumber width was ±2% of the theoretical wavelength; these widths are indicated in Figure 3. The mode-2 wavelengths are about half those of mode-1, so the actual widths are similar. The large number of wavenumbers requires considerable memory resources to complete the calculation, which ultimately limits the total number of wavenumbers that can be employed.

Many of the solutions described below were subsequently parsed to show just northward, southward, eastward, or westward wavenumbers, employing the wavenumbers indicated in Figures 4-7. The separation of the solution into these components reveals much cleaner, coherent wave patterns, reinforcing the notion that these wave fields are interference patterns, that is, the interference patterns have stable phase.

As part of the process of deciding upon an effective set of wavenumbers, two numerical experiments were conducted to test the sensitivity of the solution to wavenumber spectrum width (Figure 8) and mean wavelength (Figures 9, 12). As these quantities were varied, the misfits with respect to the point-wise, along-track estimates were computed. The region north of the Hawaiian Ridge was used for this test. Figures 8 and 9 include two curves, blue and red, corresponding to the cosine and sine components of harmonic constants, respectively. The point-wise estimates are error prone, however, hence they do not represent the reliable values one normally wants when judging misfits. They are, however, the data we have available as a test.

In testing the spectrum width, a large misfit is obtained for a very narrow spectrum, indicating the mapped values are rather poor. The misfit falls rapidly until a spectral width about 3-4% of wavelength is reached, with the misfit remaining constant or decreasing slightly with greater spectral width. With a wide spectrum, the least-squares fit approaches an ordinary objective map, which is what we want to avoid. We are attempting to fit traveling waves with well-defined frequency and wavelength. Allowing for a wide spectrum fits additional variance, to be sure, but this variance is not likely to be associated with the desired internal-tide signal. The misfit does not trend toward zero, indicating the mapped values disagree significantly with the point-wise estimates for any spectral width. This is consistent with the finding of Dushaw (2002) who found the point-wise estimates to be inherently self-inconsistent with large disagreement at cross-over points; they are error prone. A large misfit between point-wise and mapped harmonic constants is therefore to be expected. As described by Dushaw et al. (2011), one aim of the frequency-wavenumber analysis is to obtain more accurate, self-consistent solutions than these along-track estimates.

In testing the mean wavelength, the best fit to the point-wise estimates occurred for wavelengths within a few percent of the theoretical values. The minimum misfit was centered on the theoretical values. The disagreements with the point-wise estimates for center wavelengths deviating by more than about 10% of the theoretical wavelength are significantly larger. The best fits to the along-track data are for mean wavelength centered on the theoretical value.

The optimal wavenumber spectra determined by this trial-and-error process differ in many details from those described in Dushaw et al. (2011). The changes reflect refinement or evolution towards more accurate solutions; tide predictions computed for comparison to a variety of in situ data were noticably improved. It is not claimed that the ultimate, best-possible wavenumber set has been obtained.

A Comment on the Diurnals

The empirical model described here employs simple sinusoids as the basis functions for fitting the observations. Such functions are not correct near the turning latitudes, however. These latitudes are about 30° for the diurnal frequencies and about 75° for the semidiurnal frequencies (Hendershott 1981, Dushaw and Worcester 1998, Dushaw 2006; see also Wunsch and Gill 1976). The functional form of the meridional currents of internal waves at their turning latitude is approximated by Airy functions along the meridional direction, hence displacements are given as the latitudinal derivative of these Airy functions. Displacements are greatly suppressed near the turning latitudes; alternatively, these are inertial waves. As a practical matter, merely for expediency at the expense of accuracy, the diurnal waves are modeled in the present estimate using sinusoids with long wavelengths near their turning latitudes (Figures 14, 23). Such a model is not correct however, and the functional form of the diurnal waves near the turning latitude has been observed (Dushaw and Worcester 1998, Dushaw 2006). An important improvement to the model will be to implement a scheme to approximate, or otherwise accurately account for, the functional form of the diurnal wave displacements near their turning latitudes. The diurnal variations are small in most regions, so modeling errors are mostly inconsequential. In some regions, such as the Philippine Sea, diurnals make significant contributions to sea surface height, however, and correctly modeling their functional form may be essential for accurate tidal predictions.

A GLOBAL TIDAL ESTIMATE

The previous analysis by Dushaw et al. (2011) focussed on particular regions corresponding to those for which measurements were available. The present analysis aims at obtaining a global solution for internal tides, a solution that is uniform, continuous, and self-consistent. The global solution described in this report is a single, self-consistent solution encompassing all regions, the six largest tidal constitutents, and the lowest two internal tide modes. All these tidal frequencies and modes are fit to the altimetry data simultaneously. Ideally, one would also compute a continuous global solution at once, but such a solution by the frequency-wavenumber tidal analysis is not possible. First, the memory requirements of such a calculation would be prohibitive. Second, this tidal analysis cannot accomodate the spatially-varying mode parameters (e.g., Figure 12), other than by increasing the wavenumber bandwidth. The larger the area to be mapped, the more complicated the wavefield, hence the greater the number of wavenumbers that must be employed. Put another way, the wavenumber content of the global internal tide field is not uniform, or statistically stationary, over the regions of the globe.

The Global Solution

To obtain a global solution, therefore, the ocean basins were divided into 11°×11° squares that overlap by 2° (Figure 10). The choice of 11° is arbitrary; it is a large area, but not so large that the nature of the internal tide would normally change significantly within it. (The choice for area does not have to be square.) These mapped areas were then knitted together using a cosine taper, to continuously transition from one region to the other (Figures 36–41). For the M_2 constituent (Figure 36), this merging does not introduce any obvious artifacts; the solution appears continuous. For the weaker constituents, with significantly less available signal level, obvious discontinuities become apparent. The mean wavenumbers employed for the wavenumber spectrum of each region were determined using the average wavelength within the region. In most regions of the ocean, this average reasonably represents the internal tide waves, but some regions encompass significant variations in depth, with corresponding variations in mode properties. One such area is east of New Zealand with the Chatham Rise and Campbell Plateau (c.f., Figure 58). These shallow regions correspond to much shorter wavelengths than in the open ocean. For this "first pass" at a global solution, however, these complications were set aside. Accurate estimates for complicated regions such as around New Zealand likely require a tailored regional solution. Note that these mapped estimates are complicated, relatively small-scale, interference patterns that often look unintelligible on printed paper. The figures of the interfereing wavetrains look more clear on a computer screen, and clearest as animations.

Even though each 11°×11° region is estimated independently from the others, the merged tidal fields (for M_2 and S_2 frequencies anyways) are smooth and continuous across the overlapping areas. Further, because all aspects of the tidal estimate can be readily parsed or separated (these are linear waves), wavetrains in particular directions can be separated from other wavetrains (Figures 42–45). Thus, while in the subtropical North Atlantic a complicated internal tide field is obtained, parsing this solution to just show the southward wavenumbers obtains a beautiful cylindrical wave pattern emanating from the Azores and propagating almost to the north coast of Brazil (Figures 36, 43; Figures 60, 61). This continuous wavetrain crosses several regions for which the internal tides were mapped independently. Incoherent contributions to the internal tide would render an interference pattern unstable, hence impossible to observe by altimetry. It is clear that even the interference patterns are phase stable.

Constituents smaller than S_2 have very weak signals that appear to be impossible to extract (Figures 38, 39). Nevertheless, the estimate for N_2 (Figure 38) shows that the mesoscale aliasing problem noted by others has been mostly eliminated. One of the main aims of the frequency-wavenumber tidal analysis was to reduce or eliminate this aliasing problem (Dushaw et al. 2011). M_2 (12.42 hr period) and N_2 (12.66 hr period) frequencies are similar and the tidal fit is agnostic between them. The mapped estimates for N_2 have variability much weaker than for M_2. The smaller estimates for N_2 would not occur if mesoscale aliasing were significant.

In animations of these waves, basin-scale interference features are readily apparent. One predominate feature is the band of standing waves between Hawaii and the Aleutians, resulting from the waves that emanate from those places (Figure 36; Figure 47; Figure 56). This interference band spans the North Pacific basin, north to south. As seen in animations of these waves, the time scales of these inteference features are much faster than those of the waves themselves, as expected of interference effects. The fast time scales of these interference patterns may mean that internal tide signals alias to frequencies other than the 60-day band normally associated with tidal aliasing. That these features are teased from the altimetry data, with its parsimonious 10-day sampling, again demonstrates remarkable temporal and spatial coherence.

Correcting for the effects of varying stratification shows that, for equal internal displacement, the sea-surface height signals of internal tides are much greater in tropical and subtropical latitudes than at high latitudes (Figures 21–23). Thus, while the internal tides emanating from French Polynesia appear to be quite large, the corresponding internal amplitudes are relatively weaker than they would be at higher latitudes (Figure 46). The internal amplitudes of the waves around Hawaii are larger than those around French Polynesia, contrary to what is apparent from sea-surface height (compare Figures 36, 46). At high latitudes the sea-surface signature is particularly weak. One artifact of this property is that the conversion of SSH to internal amplitude in the Southern Ocean amplifies a noisy, weak signal; the variations in amplitude at high southern latitudes seen in Figure 46 are not meaningful.

There is no indication of loss of energy at the "critical latitude" near 30° as an indication of parametric subharmonic instability (PSI) (MacKinnon and Winters 2005; MacKinnon et al. 2013; Tian et al. 2006). Indeed, there are no discernable systematic changes to any properties of semidiurnal mode-1 internal tides at this latitude.

Although internal tide waves are readily seen to propagate across ocean basins, such as the North Pacific, it is also apparent from Figure 36 that their amplitude appears to be greatly diminished in the equatorial Pacific. Waves from either Hawaii and French Polynesia do not appear to propagate effectively through equatorial regions. This loss of estimated signal may be caused by the rapid equatorial wave variations or current systems. The effect on internal tides may be either this rapid variability disrupting the coherence of internal tide waves near the equator, or merely a masking of the sea-surface height signature of internal tides in equatorial regions by this noise.

The Solution in Particular Regions: Along-Track Testing

The nature of the internal tide solution is more clearly illustrated by examining the solution in particular regions of interest. As above, separating the tidal solutions into directions of propagation reveals remarkably coherent wavetrains that are otherwise masked by the interference patterns from multiple wavetrains. In addition, it is obviously important to test the accuracy of the tidal solution. One way to do this is to compare the estimated harmonic constants to the point-wise, along-track estimates for harmonic constants. These along-track estimates are error prone at all spatial scales, so they do not provide for an ideal test (Dushaw 2002). Nevertheless, the two different solutions should be reasonably, though not exactly, consistent. The along-track comparisons for the regional solutions described here show a satisfactory agreement, indicating that the estimates from frequency-wavenumber tidal analysis are at least consistent with the tidal signals in the altimetry data; the zero-order test. It may be noted that comparing the estimates to the original data is hopeless in as much as these tidal signals account for just a few percent of the variance (Dushaw et al. 2011).

Central North Pacific. The central North Pacific has been the region most often examined for internal tide signals because of the original 1987 tomography measurements there, the discovery of these signals in the altimetry records there (Ray and Mitchum 1996, 1997), and the Hawaiian Ocean Mixing Experiment (HOME) that was subsequently conducted there (Luther et al. 1999, Pinkel et al. 2000, Rudnick et al. 2003) (Figure 47). Mapped harmonic constants and along-track estimates for the M_2 constituent are reassuringly consistent (Figures 47, 48), given the expected O(1-cm) errors in the along-track estimates (Dushaw 2002). The along-track values indicated in Figure 47 are frequently shown as a single curve, but such a curve corresponds to only one component of the harmonic constants, usually $A * \cos(G)$. It is important to compare both components for an accurate assessment, however (Figure 48). These are traveling waves that have a well-defined relation between cosine and sine components that the point-wise, along track estimates do not necessarily respect. A significant disagreement between mapped and point-wise estimates in one component is likely because of inconsistent values in the other component. As noted above, the mapped solution is consistent with traveling waves by design. One source of discrepancy between mapped and point-wise, along-track values is that the mapped values shown in Figure 48 correspond to mode-1 only, whereas in certain regions significant mode-2 signals have been documented, particularly south of Hawaii (Figure 49) (Johnston et al. 2003, Dushaw et al. 2011). Mode-2 signals are estimated simultaneously with mode-1 signals with the frequency-wavenumber analysis.

The term "traveling waves" also encompasses standing waves, formed by the interference of waves traveling in opposite directions. The harmonic constants shown in the tracks of Figure 48 indicate the wave field occasionally has standing wave characteristics (Dushaw et al. 2011). Traveling waves have equal amplitude in cosine and sine components by definition. A difference in amplitudes between these components indicates standing wave effects, e.g., around 47°N on Track 79 (Figure 48). The existence of these standing wave elements indicates that the internal tide waves are so coherent in the central Pacific that the phase differences between oppositely traveling waves are stable, so that even the poor altimetry sampling recovers these characteristics. Animations of Figure 47 show these standing waves as features extending from Hawaii to the Aleutians and moving rapidly from west to east; this feature is one among many of the complicated internal-tide wave fields that the altimetry is observing, once every 10 days.

This global solution for internal tides obtains estimates for all major constituents (indeed the analysis can be expanded to include any frequencies). Figures 50–52 show the tidal solutions for the S_2, K_2, and N_2 semidiurnal constituents, and Figures 53,54 show the tidal solutions for the K_1 and O_1 diurnal constituents. These consituents have significantly weaker signals in the altimetry record, such that only S_2 has a meaningful signal in the central Pacific. K_2 and N_2 signals are quite weak, though not quite extinguished. As noted by Dushaw et al. (2011), what appears to be diurnal signals from the point-wise, along-track analysis are not internal tides; these signals are inconsistent with the internal tide dispersion relation. Although the altimetry record may not be sufficient to resolve these lesser constitutents, it seems apparent that they are nevertheless part of the internal tide signal. Their net contribution is not insignificant, however. Predictions computed from this global solution rely primarily on the harmonic constants for just the M_2 and S_2 constituents, except in some regions at lower latitudes where the contributions of the diurnal constituents are significant. The Philippine Sea is a region where diurnal variability is substantial.

South Pacific/New Zealand. The islands and topography of the South Pacific cause complicated internal tide fields (Figure 55). Even so, the frequency-wavenumber tidal analysis appears to be up to the task, with a close match to the harmonic constants obtained along the two tracks indicated in the figure. The signals around French Polynesia are particularly strong, although the topography here is several broken island chains, ridges, and plateaus (Figure 11). As noted above, waters around New Zealand have several relatively shallow plateaus, which greatly reduces the internal tide wavelength. Even so, the frequency-wavenumber analysis obtained a reasonable solution for the wavefields there. A tailored regional solution around New Zealand would result in a more accurate solution. While no obvious wavetrain is apparently emanating from the linear Kermadec Ridge to the north of New Zealand, it will be shown below that the absence of these waves is more apparent than real.

North Atlantic. Like the South Pacific, the internal tide fields of the North Atlantic are complicated, resulting from the interference of wavetrains emanating from the several island groupings, such as the Azores and Cape Verde Islands, as well as radiations from the north coast of Brazil and the eastern seaboard of the United States. Also as in the South Pacific, the frequency-wavenumber analysis is in essential agreement with the point-wise, along-track estimates. The great disagreement around 40°N on descending track 24 occurs where this track crosses the North Atlantic Current. To reiterate a general theme of this report, if these wavetrains had any incoherence, the interference patterns would be completely unstable, hence unobservable by the altimeter.

Separating Propagating Wavetrains

In the regional examples, the wave patterns are often confused, with no clear wavetrains evident. It is difficult to discern wavetrains when the wave field consists of multiple interfering waves, all traveling in different directions. The solution discussed in this report is constructed from a linear superposition of a near-continuum of wavetrains, however, so it is a simple matter to compute partial solutions consisting of waves traveling in particular directions. In other words, the solution can be parsed or separated into components traveling in particular directions. This separation of the solution allows wavetrains emanating from particular locations to be more readily seen. Similarly, the propagation of the directional wavetrains can be followed for much greater distances as these waves travel basin-scale distances. The great spatial coherence of these parsed wavetrains, both across and along the wave crests, is consistent with the evident temporal coherence of internal tides.

The wavefield for the North Central Pacific separates into clear northward and southward wave patterns (Figure 57). Waves propagating northward emanate from points along the Hawaiian Ridge forming a near planar wave (see the section Interpretation of Beams). When depicted as internal amplitude, as Figure 57 is, the waves appear to propagate across the North Pacific basin with little disruption to coherence and little decay in amplitude. The northward wavetrain, while almost planar, begins to experience cylindrical spreading at great distance from the Hawaiian Ridge. The southward propagating wave pattern emanates primarily from a "hot spot" within the Aleutian Island chain. This wavetrain is more obviously cylindrical, consistent with waves emanating from a particular point. The wavetrain emanating southward from the Hawaiian Ridge is almost planar, as for the waves emanating northward from Hawaii.

The energy density for the North Pacific solution can also be computed; Figure 58 shows the energy density from northward wavenumbers. There are clearly regions of large amplitude corresponding to regions of constructive interference (and also small amplitude in regions of destructive interference). Accounting for cylindrical spreading, there appears to be little dissipation of internal tide energy density as the waves propagate across the basin. This result also indicates that there has been little loss of internal tide coherence as these waves propagate over great distances (Dushaw et al. 2011). A loss of coherence would necessarily correspond to a loss of signal in the analysis of the altimetry data (a narrow-band time and space filter), which would result in a marked decrease in estimated amplitude.

One region of interest in this analysis has been the Kermadec Ridge north of New Zealand. This linear feature appears similar to the Hawaiian Ridge, except it is oriented meridionally. The global solution in SSH indicates no obvious or clear wavetrain from the Kermadec Ridge (Figure 59), although internal tides have been reported there (Chiswell and Moore 1999). The lack of clear radiation from the Kermadec Ridge is just a result of interference from vigorous internal tide radiation from French Polynesia confusing the picture. Constructing the solution using only eastward wavenumbers and converting SSH to internal amplitude gives a quite clear wavetrain emanating from the Kermadec Ridge (Figure 60). One of the aims of studying this region was to test the notion that the process of Parametric Subharmonic Instability was noticeably reducing internal tide energy at 28.9°. The Kermadec Ridge spans this latitude, so perhaps an interesting signal could be discerned. The variations in internal tide generation along this Ridge are too great to provide a meaningful test for this resonance phenomena. It is apparent that the southern portion of this ridge generates internal tides much more efficiently than the northern portion.

Another interesting region where clear wavetrains can be extracted out of apparent confusion is the North Atlantic (Figure 61). The wave field is a confusion of variations resulting from waves emanating from several island groupings and continents. Constructing the solution for southward wavenumbers and showing this solution in internal amplitude rather than SSH, reveals a beautiful wave pattern emanating from the Azores (Figure 62). This wavetrain appears to extend almost to the coast of Brazil. It crosses several 11°×11° regions in which the internal tides are independently estimated, yet the wavetrain is unbroken. Any incoherence in these wavetrains would render the wavefields of the North Atlantic entirely unstable with a complete loss of signal in the altimetry record.

This tidal solution is complete in that it includes all major tidal constituents (most poorly estimated for lack of signal), hence it may be used to predict the mode-1 internal tide variability at arbitrary places and times. In the next section, the global solution is used to predict the internal tide variability observed by tomography, with remarkable agreement obtained between predictions and observations. While the global solution worked fairly well, regional solutions were computed to try to obtain a better quality solution. The regional solutions generally showed marginal improvement in predictability. I expect, or hope for, even better comparisons as the processing of the altimetry tidal estimates becomes more refined.

PREDICTIONS OF TOMOGRAPHY MEASUREMENTS

Ocean acoustic tomography provides accurate, unambiguous, in situ measurements of the mode-1 internal tide (Dushaw et al. 1995b, Dushaw and Worcester 1998, Dushaw 2006, Dushaw et al. 2011). The nature of the acoustic sampling averages in the vertical, hence, much like altimetry, the measurement is a natural filter for the lowest internal wave mode. Signals of all higher modes are greatly suppressed. If reciprocal propagation is available, the sum and difference of reciprocal travel times can be computed, which unambiguously separates the temperature and current signals. Both exhibit coherent tidal variations, the former from internal tides, the latter from barotropic tides. In all existing measurements, the two signals are of comparable amplitude in acoustic travel time. In cases where only one-way acoustic propagation is available, the observed tidal variations are from the combined, and indistinguishable, baroclinic and barotropic signals. The barotropic tidal signals can be removed using numerical tidal models, however. These numerical models are accurate enough that the barotropic component of the tidal variations can be almost entirely removed (Dushaw et al. 1997, Stammer et al. 2014). In all cases, the observations of internal tides by tomography described here and elsewhere are not filtered, other than a simple high-pass filter to remove mesoscale and other low-frequency variability.

The comparison between acoustic measurements and tides began as a test of the ability of tomography to measure tidal currents (hence a test of the ability to measure current generally (Dushaw et al. 1994b)). These measurements proved to be accurate enough that the roles in the comparison were quickly reversed, with the tomography measurements providing tests of the accuracy of tidal models in determining tidal currents. Similarly, in the present report, tomography measurements of the internal tide provide a test of the global solution for mode-1 internal tides derived from altimetry. In fact, of all available measurement approaches, tomography provides the most accurate in situ measurements of mode-1 internal tides in the open ocean. The global solution and its regional derivatives were used to obtain predictions for the in situ internal tide variations as observed by several experiments employing acoustic tomography. These experiments have been conducted over the past few decades. Because the harmonic constants obtained in the global solution for internal tides will be used to predict these observations, the global solution is challenged to provide tidal predictions for time intervals spanning decades. Some of these comparisons represent an evolution of comparisons previously described by Dushaw et al. (2011).

Acoustic Mid-Ocean Dynamics Experiment (AMODE)

The 1991–2 AMODE experiment (Figure 63) took its name from the original Mid-Ocean Dynamics Experiment (MODE) experiment (Hendry 1977, The MODE Group 1978). The experiment aimed to employ acoustic tomography to measure the ocean mesoscale in a region of quiescent variability. Because the intent was to research the use of tomography data in conjunction with data assimilation techniques (Cornuelle and Worcester 1996), a quiescent region was selected to ensure the dynamics were as linear as possible. Internal tide variability was also incidentally measured (Dushaw 2006, Dushaw et al. 2011), with coherent tidal variability observed on all 15 acoustic paths of the AMODE array (Figure 63). The available record lengths varied by acoustic path, but these were generally 200–300 days. Diurnal internal tide waves were found to be resonantly trapped between the Carribean island arc and the turning latitude for these waves at about 30°N (Dushaw and Worcester 1998). The AMODE region has fairly weak mode-1 internal tides, with the tidal field comprised of several wavetrains traveling in different directions. Both the amplitude and phase of the observed internal tides can be predicted from the altimetry analysis, even though the tomography measurements were obtained a decade before the data used for the tidal analysis (Dushaw et al. 2011).

The procedures for the global solution described in this report were applied to the AMODE region (Figure 63), obtaining good predictions for the observed variability. The global solution also indicates good predictability, but the regional solution indicated in Figure 63 was somewhat better. The refined tidal analysis appears to give predictions of better quality than those first reported by Dushaw et al. (2011). Consistent with the lack of incoherent elements, there is little difference in amplitude between the in situ measurements and the prediction from altimetry. To reiterate, this coherence is all the more remarkable because the tidal field is one comprised of the interference of several wavetrains. The phases of the interference pattern are stable, indicating extraordinary coherence, spatial and temporal, of the internal tide. The ability to predict the internal tide variability averaged along all the AMODE acoustic paths also indicates that the frequency-wavenumber tidal analysis can accurately interpolate the tidal field between the altimeter tracks. Such predictability requires high spatial coherence in the tidal field.

Measurements Around the Hawaiian Ridge

The Hawaiian Ridge has been a region with intense measurement programs to determine the energetics of the tidal radiation and its role in driving deep ocean mixing (Luther et al. 1999, Pinkel et al. 2000, Rudnick et al. 2003, Zhao et al. 2010). Figure 65 indicates several of these measurements around the Hawaiian Ridge, including the 1987 Reciprocal Tomography Experiment (RTE87), which first detected coherent low-mode radiation into the central North Pacific. The farfield component of the Hawaiian Ocean Mixing Experiment (HOME) included two diamond shaped tomography arrays to resolve and measure the several waves radiating northward from the Hawaiian Ridge. The measurements from the Internal Waves Across the Pacific (IWAP) experiment in 2006, six moorings extending north from French Frigate Shoals, will be discussed in the next section. For our purposes, all these measurements comprise a set of measurements of mode-1 internal tides around Hawaii spanning the twenty years 1987 to 2006.

The mapped harmonic constants obtained from the frequency-wavenumber analysis appears to be of good quality (Figure 66), with values closely in agreement with the along-track estimates; no claim of perfection is made, of course. The estimate provides excellent predictions of mode-1 internal tides determined on the six acoustic paths of the northern (Figure 67) and southern (Figure 68) HOME tomography measurements. The tidal signals observed on the southern array were relatively weak. As in the AMODE comparisons, there is little difference between the observed and predicted tidal amplitudes, indicating the frequency-wavenumber analysis has captured nearly all of the tidal variability, that is, there is little incoherence to the internal tide field. This coherence is consistent with the tomography time series, which indicates coherent tidal variability over the 200-day record lengths.

The signals observed by the triangular RTE87 tomography array in 1987 are also predicted reasonably well (Figure 69). In the panels of the figure, the estimates for mode-1 amplitude are denoted in black, the tidal analysis of that record gives the tidally-coherent signal denoted in blue, and the independent prediction from altimetry is given in red. The record lengths extend for 120 days over summer, from May to September. The predictions in this case are not quite as good as those obtained by the earlier calculation reported by Dushaw et al. (2011); it seems evident the solutions are subject to some deviation. Path 1→2 is a meridional path which is aligned across the troughs and crests of the main radiation from the Hawaiian Ridge, hence this signal is relatively small. Figure 69 indicates excellent agreement between predictions and observations on this path, but a sign change has been applied to the predictions to obtain that agreement. Because this path averages over 6–7 cycles of the tidal wave, such a sign error may arise if the tidal analysis is slightly in error, giving an imperfect average over these cycles. The significant discrepancies between measured and predicted amplitude on this path may indeed be an indication of incoherence. Note, however, that the average SSH signal on these paths shown in the figure is scaled by millimeters, rather than the centimeters of previous figures; these are tiny signals in which noise, rather than incoherence, may dominate. The predictions here represent a 15-year hindcast of the tidal state.

One obvious step is to employ the tomography data directly in constraining the tidal solutions. There are no technical objections or impediments to using the data this way. Such an approach would employ the tomography data as a quite strong segment-averaged constraint on the solutions. It seems likely that the solution could easily accomodate this data type, given the apparent looseness of the constraints from altimetry data. It would be difficult to ascertain whether the solution was still consistent with the altimetry data, however.

Another tomographic observation of the internal tide was the SLICE'89 experiment (Worcester et al. 1994, Bracher and Flatté 1997) conducted midway between Hawaii and California in 1989 (Figure 70). This path was deployed in a region outside of the main radiation from the Hawaiian Ridge, and its orientation is not optimal for detecting radiation from that direction. The acoustic measurements lasted only 9 days, and they were one-way, employing only a single source and single vertical-line receiving array separated by 1000 km. The goal of this experiment was to determine the effects of small-scale internal waves on the details of the acoustic time fronts (acoustic intensity over depth as a function of travel time). The data from this experiment were not readily available for this report, but Figure 70 indicates the expected baroclinic and barotropic tide signals. The barotropic signal was obtained using the TPXO v.8 solution of Egbert and Eroveeva (e.g., Stammer et al. 2014). The dominant signal observed on the SLICE89 path was likely either from the Gulf of Alaska or the Mendocino Escarpment; the exact origin is unclear from the global estimate (top left panel, Figure 70).

PREDICTIONS OF THE INTERNAL WAVES ACROSS THE PACIFIC (IWAP) MEASUREMENTS

The Internal Waves Across the Pacific (IWAP) experiment consisted of moored and shipboard measurements extending along a line northward from the Hawaiian Ridge during spring 2006 (Alford et al. 2007, Zhao et al. 2009) (Figure 65). For our present purposes, the six IWAP moorings consisted of measurements by moored profilers, which by moving between 85 and 1400 m depths at 1.5-hr intervals provide good vertical resolution for the internal tides by hydrographic sampling. The record lengths obtained were only about 45 days, so temporal coherence could not be precisely determined by these direct measurements. As noted by Zhao et al. (2009), these measurements at six points are challenged to characterize a tidal field that consists of the interference of multidirectional wavefields. Zhao et al. (2009) compared the estimated SSH determined from the moored observations to those determined from a tidal analysis of altimetric data (Zhao et al. 2009, their Figure 10). The moored observations were obtained along altimeter ascending track 125 (Figure 65), so the comparison was to time series predicted from a point-wise, along track tidal analysis. Zhao et al. concluded that by the furthest mooring, MP6, the internal tide had become incoherent with the predictions from altimetry.

The in situ measurements, even though obtained with a moored profiler, likely suffered from not inconsiderable noise. A clear determination of the mode-1 signal, or almost equivalently, an error-free estimate of SSH anomaly, is challenging, even with hydrographic data extending to 1400 m. In addition, the point-wise, along track harmonic constants derived from the altimetric record likely suffer considerable errors, as documented by Dushaw (2002). Tidal predictions derived from such estimates are not likely to be reliable.

Predictions derived from the frequency-wavenumber tidal analysis are in better agreement with the IWAP measurements, including MP6, the mooring furthest from the Hawaiian Ridge (Figure 71), indicating the internal tide is coherent even at the MP6 site. Similar comparisons can be obtained at the four HOME tomography mooring sites, where thermistor records were available to determine the internal tide signals (Figure 72). The comparisons indicated in Figure 72 are of better quality than those reported earlier by Dushaw et al. (2011, Figure 14), again indicating improvement in the tidal estimates from altimetry. It may be noted that HOME tomography mooring N2 (2001) was co-located with IWAP mooring MP3 (2006); those two observed signals are directly comparable. The signal derived from N2 had only a few thermistor records available, however, so resolution of the mode-1 signal was poor. (The majority of these moored thermistors failed in the course of their deployment or recovery on the northern moorings, leaving even fewer instruments available to deploy on the southern HOME tomography moorings later.)

Dushaw et al. (2011) argues that the (unknown) local gradients of temperature were affecting the tidal estimates from the moored thermistor records, particularly with only limited sampling in the vertical. Comparing Figure 71 (MP3) with Figure 72 (N2) appears to support that notion. With the HOME N2 mooring data, a tidal amplitude of 6 cm in SSH was obtained, almost twice that obtained with the better-resolved IWAP MP3 data. The amplitudes derived from the few thermistor records are likely in error. One may note that the phase is correct, however, consistent with what would occur from local hydrographic effects.

Consistent with the conclusions of Zhao et al. (2009) and Dushaw et al. (2011), no apparent influence of Parametric Subharmonic Instability (PSI) processes (MacKinnon and Winters 2005, MacKinnon 2013) on the amplitude or phase of the mode-1 internal tides at the critical latitude is apparent in the present analysis.

MEASURED AND PREDICTED INTERNAL TIDES IN THE PHILIPPINE SEA

Unlike the region north of Hawaii, the Philippine Sea is a region of vigorous mesoscale variability (Figure 73). The U.S. Office of Naval Research funded a program in this region in 2009–2011, which included the deployment of a short-term tomography segment in 2009 as a pilot study, followed by a pentagonal array in 2010–2011 (Worcester et al. 2013) (Figures 73, 74). Since the general perception was that the mesoscale variability disrupted the coherence of internal tides, the tomography measurements in the Philippine Sea offer an interesting test of this perception. While some of the tomography data obtained from these experiments are described here, analysis of the internal tide signals in these data is still preliminary.

The mapped low-mode tides of the Philippine Sea are a confused interference of large-amplitude, multiple wavetrains traveling in different directions (Figure 74). Two main regions of generation are the Marianas Island chain to the east and the ridge within the Luzon Strait to the west. In addition to the large semidiurnal tides, the diurnal internal tides are particularly large. The tomography array configuration was similar to that of AMODE in that the line-segment elements of it were aligned in 15 different directions, giving the array almost omnidirectional sensitivity (Dushaw, 2003). Further, the array spacing or size was almost ideal for internal tide resolution - it was designed to be almost optimal for resolving the mesoscale (one of its main research purposes), hence it is also optimal for resolving the low-mode internal tides. (Optimal in this case means the most is made of limited resources.)

The pilot tomography deployment consisted of a single short acoustic path deployed within the 2010–2011 pentagonal array. The record length of acoustic transmissions was 32 days. As Figure 75 illustrates, even given the vigorous mesoscale variability and the complicated and combined semidiurnal/diurnal nature of the internal tide variability, the mode-1 internal tide still appears to be predictable. The result is all the more remarkable in that the analysis of the altimeter data has apparently resolved the complicated interference patterns of the internal tide in the Philippine Sea. The discrepancy between the measured and predicted amplitudes in Figure 75 may well be caused by some elements of incoherence. Before such a conclusion can be made, however, one must recall the nature of the estimate - made in the face of severe mesoscale noise and with an internal tide signal of near-zero signal to noise ratio. It is little wonder the altimetry analysis results in amplitudes that are biased low. The predictions are based on altimetry data obtained between 2001–2006, so for this pilot experiment the prediction is for a time period (2009) about five years after the observations.

The year after the pilot test, a full pentagonal tomographic array was deployed. Figure 76 shows data obtained on six of the 15 paths. (There are actually six more paths from a seventh mooring within the tomography array consisting of a full water column vertical line array of hydrophones and thermistors.) Record lengths on each path were about one year. The time series within the panels were obtained on paths of different orientations, so they each represent a particular directional component of the internal tide radiation. Compared to the AMODE time series of Figure 64, one can see that the Philippine Sea signals are roughly twice as large. While the comparisons of Figure 76 are still preliminary, considerable predictability is evident. Again, we can assume that the tidal estimate from altimetry has not resulted in a perfect representation of the internal tide radiation. Further improvement may be possible, or alternate approaches may result in a better predictions; it seems clear that the tidal radiation exhibits considerable coherence, despite the complicated interference patterns it forms. As for the comparison to the pilot experiment data, the predictions were derived from altimeter data obtained about six years before the in situ measurements.

As noted previously, it may be an interesting future exercise to combine the altimetric and tomographic data in a single estimate.

CALCULATING ENERGY FLUX

One of the strategies of the HOME farfield experiment was to employ the in situ data to verify the accuracy of models for the internal tide. With such verification, the in situ data is leveraged to provide a much larger scale estimate for the internal tide through modeling. The model could then be used to provide an estimate for the net energy flux by the low-order modes away from the Hawaiian Ridge. The in situ data acquired during HOME provided the first part of this strategy, so that the results of the space-time analysis of the altimetry data can now be used to calculate the net energy flux escaping from the Hawaiian Ridge.

Based on the in situ data, it appears that in the farfield of the Hawaiian Ridge, the mode-1 internal tides have a surprisingly weak O(1 kW/m or less) energy flux on either side of the Ridge, suggesting that most of the available tidal energy is dissipated in the "nearfield", i.e., within 500 km, of the Ridge. As measured by tomography, the M_2, mode-1 energy flux across the main diagonal of the northern tomography array was only 1.45 $kW \cdot m^{-1}$. This energy flux estimate is roughly consistent with values of internal-tide energy previously determined by T/P altimetry data (Dushaw 2002). These values suggest that only 4–5 GW of M_2 tidal energy escapes the 2000-km-long Hawaiian Ridge as mode-1 internal tide radiation. Measures of the local tidal energy dissipation at Hawaii were 3±1.5 GW (Klymak et al. 2006), however, whereas barotropic tidal models insist that some 20 GW of M_2 tidal energy is dissipated at the Hawaiian Ridge (Egbert and Ray 2001, Zaron and Ebert 2006). With these values, an energy loss of about 10–15 GW has gone unaccounted for, although uncertainties are large. Carter et al. (2008) reviewed this energy budget in the context of a regional model, finding that the majority of energy lost from the barotropic tide (60%) was radiated out of their model domain by low-order modes.

A novel and rigorous approach to estimating the mode-1 energy flux from the altimetric measurements is proposed. The energy flux is fundamentally defined as ($\langle p'u' \rangle$,$\langle p'v' \rangle$). In the context of the interference patterns of the internal tide around Hawaii, some care must be given to defining what is meant by the brackets < . >. This averaging implies an average over time to remove the oscillations of energy flux with time, an average over depth to remove the oscillations of energy flux with depth, and, by analogy, an average over area to remove the oscillations of energy flux with area. This latter average is most often omitted, giving the common figures of high-energy jets apparently emanating from such locations as the Kaena Ridge. But these jets are an artifact of the interference of multiple waves (Rainville et al. 2009), hence such models of energy flux are not quite rigorous. Without the area average, expressions such as $\langle p'u' \rangle$, with p and u expanded as grand summations over frequency, mode, and wavenumber, retain cross terms of wavenumber, which have no clear physical meaning. With such averaging, the < . > reduces to a simple summation of the individual components, as required.

As an alternative to the averaging implied by the brackets, the variability can be separated in time, depth and area manually. A tidal analysis can separate the signals of the constituent frequencies, a modal decomposition can separate the signals of individual modes, and a wavenumber decomposition can separate the signals of individual wavenumbers. With this separation, no averaging < . > is required, since the individual components of the tidal variability can be directly added. The tidal analysis and modal decomposition are familiar techniques. The wavenumber decomposition is a direct product of the the space-time tidal analysis. Thus, the three decompositions of the tidal variability are accomplished: the tidal analysis is included in the space-time analysis, the SSH is dominated by mode 1 and consistent with the mode-1 dispersion relation, and the wavenumber decomposition is included in the space-time tidal analysis.

The wavenumber decomposition is a three-step process. The weighted-least-squares technique employed here is a biased estimator. This means that the fit strives to reduce the variance associated with any one wavenumber by giving values to as many wavenumbers as possible, while staying within the modeling constraints. The fit therefore minimizes the energy associated with the wavenumbers, which is precisely what is not wanted in this case. The strategy is therefore to (1) perform the space-time analysis to obtain an estimate for the wavenumber spectrum, (2) based on the spectrum, choose the subset of wavenumbers that best characterize the spectrum, i.e., wavenumbers of the peaks of the spectrum, and (3) redo the space-time analysis using only the small subset of wavenumbers derived from the initial spectrum. The result of this procedure is that the amplitude for each wavenumber is much less susceptible to the biased nature of weighted least squares. (In the frequency domain, this procedure is equivalent to calculating a frequency spectrum to find the tidal lines, followed by a harmonic analysis using the frequencies of those tidal lines.)

This project aims to eventually derive such spectra for the internal tides, so that the energy flux carried by the mode-1 internal tide can be computed directly. With this approach, the issue of the beams of tidal energy and their nature as the product of the interference of multiple waves is resolved.

DISCUSSION

This report is written about 20 years after the first publication describing the radiation of coherent internal tides far into the interior of an ocean basin (Dushaw et al. 1995). It is, to this author, rather peculiar that the result of this report should have taken this long to be sorted out. The result is, on the face of it, the most simple, straightforward interpretation of the altimeter measurements possible. Three basic factors may have been causes of delay. First, it appears to be an inherent belief of physical oceanographers that any variability of the ocean must necessarily be incoherent. Overcoming this preconception has been challenging. The example of mode-1 internal tides is the first, and perhaps only, example of baroclinic predictability. While there may be (rather weak in the case of mode-1) theoretical arguments for incoherence, this author is unaware of any solid observational evidence showing the incoherence of mode-1 internal tides. Second, it cannot be denied that physical oceanographers have had a less-than-enthusiastic response to ocean acoustic tomography. Oceanographers have exhibited great reluctance in accepting this techinque. It is the belief of this author that the question of internal tide coherence became wrapped up with the question of acceptance of acoustic tomography as a viable observing technique. As of this writing, I know of no publications, outside of my own, that explicitly acknowledge the nature of the internal tides as observed by tomography. Ultimately, ignoring observations that contradict prevailing, but unsubstantiated, perceptions has the consequence that the progress of science is obstructed or misdirected, as seems to have been the case here. Third, the determination of an accurate mode-1 internal tide estimate by in situ observations is challenging. Analyses of moored thermistor data are easily corrupted by higher-order mode contamination and the inability to resolve the lowest internal tide mode with accuracy. Determination of even ordinary barotropic tidal currents from current meter moorings is fraught with inaccuracy (Dushaw et al. 1997, Stammer et al. 2014). The extraction of a clear first mode internal tide signal from moored thermistor data is an even more challenging exercise. Nevertheless, the straightforward interpretation of altimetry and tomography observations have resulted in the demonstration of the remarkable predictability of mode-1 internal tides. The essential conclusion of this report, that mode-1 internal tides are largely predictable in most regions of the world's oceans, rests firmly on the tomography observations.

Zaron and Egbert (2014) examined the time-variable refraction of the internal tide near the Hawaiian Ridge, employing the Simple Ocean Data Assimilation (SODA) numerical ocean model for realizations of the mesoscale environment. Their estimate for the standard deviation of mode-1 phase speed derived from this model (their Figure 10, ca. 0.08 m/s; deemed a lower bound) is roughly consistent with that obtained from analysis of the Hawaiian Ocean Time series

(HOT) in situ hydrographic data (Figure 65, Dushaw 2002; deemed and upper bound). Their analysis indicated that a substantial portion of the coherent internal tide is scattered into the non-stationary tide, with perhaps 20% of the baroclinic tidal energy flux lost by adiabatic scattering (refraction) within 250 km of the Hawaiian Ridge. It would be an interesting task to reconcile this conclusion, with that of the present report, which appear to be in contradiction. Zaron and Egbert conclude: "In contrast to mooring-based observations, inferences from long-range reciprocal acoustic travel time (Dushaw et al. 1995) and along-track satellite altimetry (Dushaw et al. 2011; Ray and Zaron 2011) find that much of the baroclinic tidal variance is coherent and phase locked with its forcing. The maps presented in Figs. 8, 11, and 12 [of Zaron and Egbert] illustrate the spatial inhomogeneity of tidal variability and suggest that some caution is warranted in interpreting along-track or line-integral measurements." Thus suggesting that the two results can be reconciled by a more cautious interpretation; what that alternate interpretation could be is unstated. As has been demonstrated in this report, however, mooring-based observations are also coherent, at least to the extent that this data type can resolve a clear mode-1 signal. One possible issue with this comparison is suggested by the assumption by Zaron and Egbert that their estimate of energy loss is "a value regarded as a lower bound because of the smoothed nature of the SODA fields used in this study." The logic of this statement appears to be false, based on a similar situation in comparing the acoustic properties of numerical ocean models. Acoustic propagation is a phenomena not entirely dissimilar to the propagation of low-mode internal waves. Comparison of the acoustic properties of several ocean models finds them to be quite different, with the highly-smoothed World Ocean Atlas providing the best comparisons to observation (Dushaw et al. 2013). The models often have unphysical sound speed gradients that significantly affect the acoustic propagation. It appears that the true ocean behaves in a remarkably smooth way, at least insofar as acoustic propagation is concerned, with ocean models often failing to capture this property. In short, it may be that the Zaron and Egbert result stems from artifacts of the numerical ocean model employed. Ultimately, the resolution of these two results may be one of "degree", leaving the mode-1 internal tides with a modest degree of incoherence, neither perfectly coherent, nor substantially incoherent. Incoherence may also be a fleeting, or temporary, property, with occasional mesoscale events knocking the internal tide off its phase, but with phase coherence maintained most of the time; no obvious examples of such events have been observed, however.

One aspect to these global solutions to be determined is the degree to which they are able to predict internal tide variability near coasts or in regions with a shallow or sloping sea floor (e.g., von Haren 2007, Nash et al. 2012). In such regions the internal tides become complicated, of course, such that the concept of a particular internal wave mode becomes ill-defined. Points near coasts or internal tide generating topography are within the nearfield of the tidal radiation. In some ways, however, these kinds of regions are of greatest oceanographic interest, hence the predictability of the internal tide signals there may be of greatest relevance. Two basic factors appear to be relevant and perhaps unresolved. These are (1) whether the altimetry signal is affected by the proximity to coasts, hence precluding accurate tidal estimates there, or (2) whether there is, in fact, no inherent predictability to any of the baroclinic tidal motions near coasts. Resolving these questions will be challenging; the observational difficulties are formidable.

One can compare the estimated M_2, mode-1 internal tides (Figures 36,46) to the sea floor topography. This comparison finds that the internal tides determined from altimetry correspond to topographic features, which is reassuring. The estimates were obtained without employing the sea floor topography, of course. One notable exception is to the east of the southern tip of South

America, where considerable internal tide variability is obtained that does not correspond to a particular topographic feature. The estimates are likely in error here. While there is no obvious explanation for this apparent error, one can speculate that the barotropic tidal model used to remove the barotropic tides from the altimetric record may be in error in this region. Residual barotropic signals may be appearing in the global solution, but such residual signals would have to correspond to the dispersion relation for internal tides to be able to influence the solution.

In one exercise during this analysis, an attempt was made to employ the AVISO estimates for SSH anomaly to subtract the mesoscale noise from the altimetry records prior to the tidal analysis. The main aim with this strategy was to reduce the mesoscale noise, hence enhance the internal tide SNR. The results from this procedure were mixed. The reduction of the mesoscale noise in the AMODE region appeared to improve the predictions compared to data. The same reduction in the Philippine Sea region appeared to make the tidal solution worse. One suggestion that might explain this discrepancy is that the AVISO SSH anomaly estimates have aliased, or incorporated, the signals of diurnal internal tides to some degree. Because the diurnals are particularly large in the Philippine Sea region, subtracting the AVISO product from the altimetry record may have affected the diurnal signal, hence causing errors in those estimates.

The possible applications of a global solution for mode-1 internal tides have yet to be determined. One obvious application is to subtract the internal tide signals from other data, hence reduce the tidal noise in those data. Internal tide signals would be affecting measurements of sea surface height by altimeters, of course, but also such measurements as underway ADCP measures of upper-ocean currents or even Argo hydrography. As noted earlier, the time scales for the interference patterns of internal tides are faster than for the tides themselves, hence this tidal variability may be aliasing to unexpected frequency bands. The interference patterns are, of course, periodic. If enough confidence in a global tidal solution can be garnered (not necessarily the one described in this report), the mode-1 internal tides can be used as a test signal for any particular observations or analysis. For example, how well do the observations recorded by a particular mooring resolve baroclinic signals? It seems likely that a global self-consistent solution for internal tides as described here may result in more accurate studies of the energetics of this tidal radiation. From one perspective, as scientists we seek only an accurate description of nature, irrespective of applications; the nature of the mode-1 internal tides is astonishing.

APPENDIX: COMMENTS ON COMPUTATION

The frequency-wavenumber tidal analysis is merely a large least-squares problem. As such, it is solved by a sequence of simple matrix computations. The dimensions of the matrices involved are large, so the solution to this problem is computationally challenging. Two aspects of this problem that make this solution easier are that they are simple matrix computations, handled by ordinary Basic Linear Algebra Subroutines (BLAS), and that they can be computed in single precision. The data are quite noisy and only a loose fit to these data can be expected, so single precision is perfectly adequate. In addition, the entire calculation does not have to be done at once. Rather, recursive least squares was employed to fit the data piecemeal and reduce the problem dimensions (at the expense of the computational inefficiency of recursive least squares). It may be worth noting that when single precision calculations are employed, Intel's hyperthreading technology can be effective.

Recognizing the computational challenges of the problem, I early on embarked on the strategy of employing computing on a Graphics Processing Unit (GPU), which promised quite large computational power at modest expense. Graphics cards can be employed in a PC as a coprocessor with O(1000) processors. In particular, the ability of calling up GPU computational power transparently from within an ordinary matlab script was appealing (Dushaw 2008). Getting such code up and running proved daunting, but was ultimately quite successful. The software design became easier as Nvidia and other software developers (MAGMA, CULA) fully implemented BLAS and LAPACK subroutines for GPU computing. Early on, the computational speed up was an order of magnitude. In this regard, being able to employ single precision matrices was critical, since these GPUs primarily compute in single precision. The computational power does not scale as the number of processors on the GPU, however. Interprocess communications within the GPU slow things down, as does the simple task of copying data to the GPU memory and copying the results back. Typically the latter tasks are the slowest aspects of these calculations.

Matlab soon realized the potential for GPU computing, and they have implemented this capability in their parallel processing toolbox. While the routines I developed in C for these calculations were challenging, though not particularly complicated in the end, the equivalent calculation in matlab is extraordinarily simple. The simple code is illustrated below; this routine is the least squares "engine" used for computing the frequency-wavenumber tidal analysis described in this report.

Compared to a high-end intel i7-3820 3.6 GHz cpu, an Nvidia Titan GPU (ca. $1000 in 2012; 6 GB of RAM) offered a speed up of about a factor of about 7.5. The GPU was therefore about equivalent to a 28 GHz quadcore processor. Even with this speed up, the global solutions obtained for this report required about 30 hrs of continuous calculation. Of course, the main computational challenge lies in all the preliminary computations required to get the software developed, optimized, and debugged to finally make the ultimate computation.

Matlab Routine: A Least Squares Fit on a Graphics Processing Unit

N.B.: Notation is the same as in Dushaw et al. (1995) or Dushaw et al. (2011). It is hoped the meaning of the various variables can be guessed by the reader from the variable names.

```
%  function  [mhat Rmm] = engine14(V0u1,F1,omega1,KXIND,KX1, ...
%                                    timex,data,Rnn0,mhat,Rmm,Nstate);
%  Input arrays must be single precision.
%  mhatp, Rmmp are previous values updated by this routine.
%  Calculates:  G = [f*cos(kx-wt-(V0+u)) f*sin(kx-wt-(V0+u))]
%               GR = G*Rmmp
%               Rdd = GR*G' + Rnn
%               L'  = Rdd\GR         - Kalman gain
%               mhat = =mhatp + L*d;  - update model parameters
%               Rmm = Rmmp - L*(GR) ( = Rmmp - L*Rdd*L' )  - update model covariance
%
%  B. Dushaw  2/2014

function  [mhath Rmmh] = engine14(V0u1, F1, omega1, KXIND, KX1, ...
                                    timex, data, Rnn0, mhath, Rmmh, Nstate);

% Do the main matrix calculations using GPU arrays - a factor of 10 speed up for a Titan v. i7-3820.

mhat=gpuArray(mhath);   % h for host, as opposed to GPU device.
Rmm=gpuArray(Rmmh);

[ND NT]=size(data);      % ND points of altimeter measurements at NT times.
HNstate=0.5*Nstate;

NP=10;                   % Take NP data at a time for speed up.  Size of NP is limited by GPU memory.
mmm=mod(NT,NP);
index=1;
for i=1:NP:NT,     % NT is the length of timex
   if    (index+(NP-1)) > NT & mmm ~=0,
     NP=mmm;
   elseif (index+(NP-1)) > NT & mmm ==0,
     break
   end

   dh=data(:,index:(index+(NP-1)));
   dh=dh(:);
   d=gpuArray(dh);

   rnn=Rnn0(:,index:(index+(NP-1)));
   Rnn=gpuArray(rnn);
   Rnn=diag(Rnn(:));
```

```
    arg0=[];   f0=[];
    for kk=1:NP,
      time0=timex(index);

    % Gets arg0=KX - om*t - (V0+u)  and f0=f.
    % Keep all this initial setup stuff on the host, rather than the GPU, since it doesn't take long.
    % Minimize Host-Device transfers.  At each time step there is only one set of f's and V0U's.
      f1=F1(index,:);
      V0U1=V0u1(index,:);
      arg=zeros(size(KX1));
      f=arg;
      istart=1;
      for kgh=1:length(KXIND),
        iend=istart+KXIND(kgh)-1;
        II=istart:iend;
        QQQ=ones(length(II),1);
        arg(II)=KX1(II)-QQQ*omega1(kgh)*time0-QQQ*V0U1(kgh);
        f(II)=QQQ*f1(kgh);
        istart=iend+1;
      end

    % Reorganize so that data dimension is column, model dimension is row.
      arg0=[arg0; reshape(arg,ND,HNstate)];
      f0=[f0; reshape(f,ND,HNstate)];
      index=index+1;
    end  % End kk loop.

   % Calculate G = [f*cos(kxomt) f*sin(kxomt)], dimension # Data X # Model Parameters.
     argd=gpuArray(arg0);
     fd=gpuArray(f0);
     G=[fd.*cos(argd) fd.*sin(argd)];

   % The big matrix here is Rmm - 13000X13000.  For NP=10, Rdd is ca. 1000X1000.
     d=d - G*mhat;
     GR=G*Rmm;
     Rdd=GR*G' + Rnn;
     L=(Rdd\(GR))';

     mhat=mhat+L*d;
     Rmm=Rmm-L*GR;
end   % End i:NP:NT loop.

mhath=gather(mhat);      % Bring variables back to PC memory from GPU memory.
Rmmh=gather(Rmm);

end   % End function.
```

REFERENCES

Alford, M. H., J. A. MacKinnon, Z. Zhao, R. Pinkel, J. Klymak, and T. Peacock, 2007. Internal waves across the Pacific, *Geophys. Res. Lett.,* **34**, L24601. doi: 10.1029/2007GL031566

Antonov, J. I., D. Seidov, T. P. Boyer, R. A. Locarnini, A. V. Mishonov, H E. Garcia, O. K. Baranova, M. M. Zweng, and D. R. Johnson, 2010. World Ocean Atlas 2009, Volume 2: Salinity. S. Levitus, Ed., NOAA Atlas NESDIS 69, U.S. Government Printing Office, Washington, D.C., 184 pp.

Arbic, B. K., J. G. Richman, J. F. Shriver, P. G. Timko, E. J. Metzger, and A. J. Wallcraft, 2012. Global modeling of internal tides within an eddying ocean general circulation model, *Oceanography,* **25**, 20–29.

Bracher, C., and S. M. Flatté, 1997. A baroclinic tide in the Eastern North Pacific determined from 1000-km acoustic transmissions, *J. Phys. Oceanogr.,* **27**, 485–497.

Carter, G. S., M. A. Merrifield, J. M. Becker, K. Katsumata, M. C. Gregg, D. S. Luther, M. D. Levine, T. J. Boyd, and Y. L. Firing, 2008. Energetics of M_2 barotropic-to-baroclinic tidal conversion at the Hawaiian Islands, *J. Phys. Oceanogr.,* **38**, 2205–2223.

Chelton, D. B., R. A. deSzoeke, M. G. Schlax, K. El Naggar, and N. Siwertz, 1998. Geographical variability of the first baroclinic Rossby radius of deformation, *J. Phys. Oceanogr.,* **28**, 433–460.

Chiswell, S. M., and M. I. Moore, 1999. Internal tides near the Kermadec Ridge. *J. Phys. Oceanogr.,* **29**, 1019–1035.

Cornuelle, B. D., and Worcester P. F., 1996. Ocean Acoustic Tomography: Integral data and ocean models. In *Modern Approaches to Data Assimilation in Ocean Modeling*, P. Malanotte-Rizzoli, Ed. Elsevier oceanography series, Amsterdam, New York: Elsevier, 97–115.

Dibarboure, G., Lauret, O., Mertz, F., Rosmorduc, V., Maheu, C., 2009. *SSALTO/DUACS User Handbook: (M)SLA and (M)ADT Near-Real Time and Delayed Products.* AVISO Altimetry CLS-DOS-NT-06.034, Issue 1.10, SALP-MU-P-EA-21065-CLS, March 4, 2009, 41 pp.

Dushaw, B. D., 1998. Internal tides of the western North Atlantic, AGU-Ocean Sciences Meeting, San Diego, CA, *EOS, Transactions, AGU, suppl.,* **79,** p. OS187.

Dushaw, B. D., 2000. A review of internal tide observations by acoustic tomography and altimetry, *Proc. 5th Pacific Ocean Remote Sensing Conf. (PORSEC)*, Goa, India, 5–8 December 2000, vol. II, 651–652.

Dushaw, B. D., 2002. Mapping low-mode internal tides near Hawaii using TOPEX/POSEIDON altimeter data. *Geophys. Res. Lett.,* **29(9)**, doi: 10.1029/2001GL013944.

Dushaw, B. D., 2003. Mapping and wavenumber resolution of line-integral data for observations of low-mode internal tides. *J. Ocean. Atmos. Tech.,* **20**, 1043–1059.

Dushaw, B. D., 2006. Mode-1 internal tides in the western North Atlantic Ocean, *Deep Sea Res. I,* **53**, 449–473.

Dushaw, B., 2008. Matlab and CUDA, Internal report, Applied Physics Laboratory, University of Washington. Published on-line on the Nvidia CUDA forum. (direct link: http://faculty.washington.edu/dushaw/epubs/Matlab_CUDA_Tutorial_2_10.pdf), 25 pp., August 19, 2008, revised February 2, 2010.

Dushaw, B. D., 2013. "Ocean Acoustic Tomography" in *Encyclopedia of Remote Sensing*, E. G. Njoku, Ed., Springer-Verlag Berlin Heidelberg. doi: 10.1007/SpringerReference_331410

Dushaw, B. D., 2014. Tomography and the global predictability of mode-1 internal tides, AGU Ocean Sciences Meeting, Honolulu, HI, Abstract ID 13727.
http://www.sgmeet.com/osm2014/viewabstract.asp?abstractid=13727
http://www.eposters.net/pdfs/tomography-and-the-global-predictability-of-mode1-internal-tides.pdf

Dushaw, B. D., G. D. Egbert, P. F. Worcester, B. D. Cornuelle, B. M. Howe, and K. Metzger, 1997. A TOPEX/POSEIDON global tidal model (TPXO.2) and barotropic tidal currents determined from long-range acoustic transmissions. *Prog. Oceanogr.,* **40**, 337–367.

Dushaw, B. D., P. F. Worcester, B. D. Cornuelle, and B. M. Howe, 1994a. Barotropic and baroclinic tides of the western North Atlantic. AGU Fall Meeting, San Francisco, California, *EOS, Transactions, American Geophysical Union,* **75,** Supplement, 307.

Dushaw, B. D., P. F. Worcester, B. D. Cornuelle, and B. M. Howe, 1994b. Barotropic currents and vorticity in the central North Pacific Ocean during summer 1987 determined from long-range reciprocal acoustic transmissions, *J. Geophys. Res.,* **99**, 3263–3272.

Dushaw, B., P. Worcester, B. Cornuelle, and B. Howe, 1995a. The internal tide of the western North Atlantic observed using long-range reciprocal acoustic transmissions. ASA Spring Meeting, Washington, D.C. *J. Acoust. Soc. Am.,* **97,** 3263.

Dushaw, B. D., P. F. Worcester, B. D. Cornuelle, B. M. Howe, and D. S. Luther, 1995b. Baroclinic and barotropic tides in the central North Pacific Ocean determined from long-range reciprocal acoustic transmissions. *J. Phys. Oceanogr.,* **25**, 631–647.

Dushaw, B. D., and P. F. Worcester, 1998. Resonant diurnal internal tides in the North Atlantic, *Geophys. Res. Lett.,* **25**, 2189–2193.

Dushaw, B. D., P. F. Worcester, and M. A. Dzieciuch, 2011. On the predictability of mode-1 internal tides, *Deep-Sea Res. I***,** **58**, 677–698, doi: 10.1016/j.dsr.2011.04.002.

Dushaw, B. D., P. F. Worcester, M. A. Dzieciuch, and D. Menemenlis, 2013. On the time-mean state of ocean models and the properties of long-range acoustic propagation, *J. Geophys. Res.*, **118**. doi: 10.1002/jgrc.20325.

Dyson, F., W. Munk, and B. Zetler, 1976. Interpretation of multipath scintillations Eleuthera to Bermuda in terms of internal waves and tides. *J. Acoust. Soc. Am.,* **59,** 1121–1133.

von Haren, H., 2007. Unpredictability of internal M_2, *Ocean Sci.,* **3**, 337–344. url: www.ocean-sci.net/3/337/2007/

Headrick, R. H., J. L. Spiesberger, and P. J. Bushong, 1993. Tidal signals in basin-scale acoustic transmissions, *J. Acoust. Soc. Am.,* **93,** 790–802. doi: 10.1121/1.405441

Hendershott, M. C., 1981. Long waves and ocean tides, In: *The Evolution of Physical Oceanography*, Warren, B. A., Wunsch, C. (Eds.). Cambridge, Massachusetts: The MIT Press, pp. 292–341.

Hendry, R. M., 1977. Observations of the semidiurnal internal tide in the western North Atlantic ocean, *Philos. Trans. R. Soc.,* **A286**, 1–24.

Jensen, F. B., W. A. Kuperman, M. B. Porter, and H. Schmidt, 1994. *Computational Ocean Acoustics*. American Institute of Physics, Woodbury, NY.

Johnston, T. M. S., M. A. Merrifield, and P. E. Holloway, 2003. Internal tide scattering at the Line Islands Ridge, *J. Geophys. Res.,* **108**, 3365. doi: 10.1029/2003JC001844

Klymak, J. M., J. N. Moum, J. D. Nash, E. Kunze, J. B. Girton, G. S. Carter, C. M. Lee, T. B. Sanford, and M. C. Gregg, 2006. An estimate of tidal energy lost to turbulence at the Hawaiian Ridge, *J. Phys. Oceanogr.,* **36**, 1148–1164.

Locarnini, R. A., A. V. Mishonov, J. I Antonov, T. P. Boyer, H. E. Garcia, O. K. Baranova, M. M. Zweng, and D. R. Johnson, 2010. World Ocean Atlas 2009, Volume 1: Temperature. S. Levitus, Ed., NOAA Atlas NESDIS 68, U.S. Government Printing Office, Washington, D.C., 184 pp.

Luther, D.S. and the HOME PIs, 1999. The Hawaii Ocean Mixing Experiment (HOME): Is the abyssal stratification maintained by tidalgenic mixing?, *Proc., 11th 'Aha Huliko'a Hawaiian Winter Workshop*, Univ. of Hawaii, January 19–22, l999, pp. 57–62.

MacKinnon, J. A., and K. B. Winters, 2005. Subtropical catastrophe: Significant loss of low-mode tidal energy at 28.9 degrees, *Geophys. Res. Lett.,* **32**, L15605. doi: 10.1029/2005GL023376

MacKinnon, J. A., M. H. Alford, O. Sun, R. Pinkel, Z. Zhao, and J. Klymak, 2013. Parametric subharmonic instability of the internal tide at 29°N, *J. Phys. Oceanogr.,* **43**, 17–28. doi: 10.1175/JPO-D-11-0108.1

The MODE Group, 1978. The Mid-Ocean Dynamics Experiment, *Deep-Sea Res.,* **25**, 859–910.

Munk, W., B. Zetler, J. Clark, S. Gill, D. Porter, J. Speisberger, and R. Spindel, 1981. Tidal effects on long-range sound transmissions, *J. Geophys. Res.,* **86**, 6399–6410.

Nash, J. D., S. M. Kelly, E. L. Shroyer, J. N. Moum, and T. F. Duda, 2012. The unpredictable nature of internal tides on continental shelves, *J. Phys. Oceanogr.,* **42**, 1981–2000. doi: 10.1175/JPO-D-12-028.1

Pinkel, R., W. Munk, P. Worcester, B. D. Cornuelle, D. Rudnick, J. Sherman, J. H. Filloux, B. D. Dushaw, B. M. Howe, T. B. Sanford, C. M. Lee, E. Kunze, M. C. Gregg, J. B. Miller, J. M. Moum, D. R. Caldwell, M. D. Levine, T. Boyd, G. D. Egbert, M. A. Merrifield, D. S. Luther, E. Firing, R. Brainard, P. J. Flament, and A. D. Chave, 2000. Ocean mixing studied near Hawaiian Ridge, *Eos, Trans. Am. Geophys. U.,* **81**, pp. 545,553.

Rainville, L., and R. Pinkel, 2006. Propagation of low-mode internal waves through the ocean, *J. Phys. Oceanogr.,* **36**, 1220–1236. doi: 10.1175/JPO2889.1

Rainville, L., T. M. Shaun Johnston, G. S. Carter, M. A. Merrifield, R. Pinkel, P. F. Worcester, and B. D. Dushaw, 2010. Interference pattern and propagation of the M_2 internal tide south of the Hawaiian Ridge, *J. Phys. Oceanogr.,* **40**, 311–325. doi: 10.1175/2009JPO4256.1

Ray, R. D., and Mitchum, G. T., 1996. Surface manifestation of internal tides generated near Hawaii, *Geophys. Res. Lett.* **23**, 2101–2104.

Ray, R. D., and Mitchum, G. T., 1997. Surface manifestation of internal tides in the deep ocean: Observations from altimetry and island gauges, *Prog. Oceanogr.,* **40**, 337–367.

Ray, R. D., and D. E. Cartwright, 2001. Estimates of internal tide energy fluxes from TOPEX/Poseidon altimetry: Central North Pacific, *Geophys. Res. Lett.,* **28**, 1259–1262.

Ray, R. D., and E. D. Zaron, 2011. Non-stationary internal tides observed with satellite altimetry, *Geophys. Res. Lett.,* **38**, L17609. doi: 10.1029/2011GL048617

Rudnick, D. L., T. J. Boyd, R. E. Brainard, et al., 2003. From tides to mixing along the Hawaiian Ridge, *Science,* **301**, 355–357.

Schureman, P., 1958. *Manual of harmonic analysis and prediction of tides.* Special Publication 98, U.S. Coast and Geodesic Survey, U.S. Government Printing Office, Washington, D.C.

Stammer, D., R. D. Ray, O. B. Andersen, B. K. Arbic, W. Bosch, L. Carrère, Y. Cheng, D. S. Chinn, B. D. Dushaw , G. D. Egbert, S. Y. Erofeeva, H. S. Fok, J. A. M. Green, S. Griffiths, M. A. King, V. Lapin, F. G. Lemoine , S. B. Luthcke, F. Lyard, J. Morison, M. Müller, L. Padman, J. G. Richman, J. F. Shriver, C. K. Shum, E. Taguchi, Y. Yi, 2014, Accuracy assessment of global ocean tide models, *Reviews of Geophys.***,** **52**, 243–282. doi: 10.1002/2014RG000450.

Smith, W. H. F., and D. T. Sandwell, 1997. Global seafloor topography from satellite altimetry and 313 ship depth soundings, *Science,* **277**, 1957−1962.

Tian, J., L. Zhou, and X. Zhang, 2006. Latitudinal distribution of mixing rate caused by M_2 internal tide, *J. Phys. Oceanogr.,* **36**, 35–42. doi: 10.1175/JPO2824.1.

Weinberg, N. L., J. Clark, and R. P. Flanagan, 1974. Internal tidal influence on deep-ocean acoustic-ray propagation, *J. Acoust. Soc. Am.,* **56,** 447–458.

Worcester, P. F., B. D. Cornuelle, J. A. Hildebrand, W. S. Hodgkiss, T. F. Duda, J. Boyd, B. M. Howe, J. A. Mercer, and R. C. Spindel, 1994. A comparison of measured and predicted broadband acoustic arrival patterns in travel time-depth coordinates at 1000-km range, *J. Acoust. Soc. Am.,* **95,** 3118–3128.

Worcester, P. F., M. A. Dzieciuch, J. A. Mercer, R. K. Andrew, B. D. Dushaw, A. B. Baggeroer, K. D. Heaney, G. L. D'Spain, J. A. Colosi, R. A. Stephen, J. N. Kemp, B. M. Howe, L. J. Van Uffelen, and K. E. Wage, 2013. The North Pacific Acoustic Laboratory deep-water acoustic propagation experiments in the Philippine Sea, *J. Acoust. Soc. Am.,* **134,** 3359–3375. doi: 10.1121/1.4818887

Wunsch, C., 2010. Toward a midlatitude ocean frequency-wavenumber spectral density and trend determination, *J. Phys. Oceanogr.,* **40**, 2264−2281. doi: 10.1175/2010JPO4376.1

Wunsch, C., and A. E. Gill, 1976. Observation of equatorially trapped waves in Pacific sea level variations, *Deep-Sea Res.,* **23**, 371−390.

Wunsch, C., and D. Stammer, 1995. The global frequency-wavenumber spectrum of oceanic variability estimated from TOPEX/POSEIDON altimetric measurements, *J. Geophys. Res.,* **100**, 24895−24910. doi: 10.1029/95JC01783

Zaron, E. D., and G. D. Egbert, 2014. Time-variable refraction of the internal tide at the Hawaiian Ridge, *J. Phys. Oceanogr.,* **44**, 538−557. doi: 10.1175/JPO-D-12-0238.1

Zhao, Z., and M. H. Alford, 2009. New altimetric estimates of mode-1 M_2 internal tides in the central North Pacific Ocean, *J. Phys. Oceanogr.,* **39**, 1669−1684. doi: 10.1175/2009JPO3922.1.

Zhao, Z., M. H. Alford, J. A. MacKinnon, and R. Pinkel, 2010. Long-range propagation of the semidiurnal internal tide from the Hawaiian Ridge, *J. Phys. Oceanogr.,* **40**, 713−736.

Zhao, Z., M. H. Alford, and J. B. Girton, 2012. Mapping low-mode internal tides from multisatelite altimetry, *Oceanography,* **25**, 42–51.

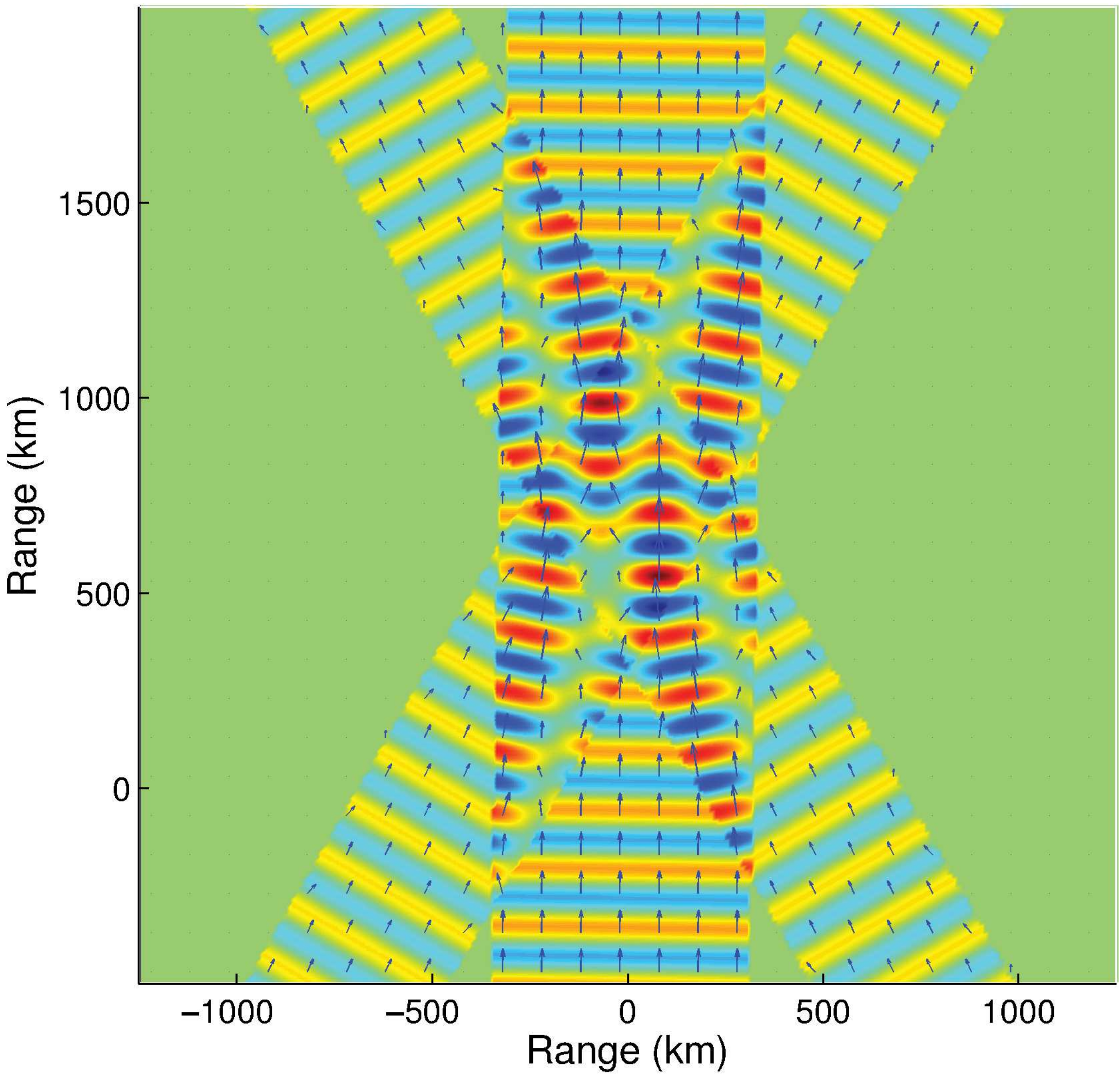

Figure 1. A simple illustration of the problem of deriving point-wise energy flux vectors from a field comprised of interfering waves. Where these waves form a complicated interference pattern at their intersection, a complicated field of energy flux vectors is obtained. In this case, there are only three energy flux vectors, one for each monochromatic wave.

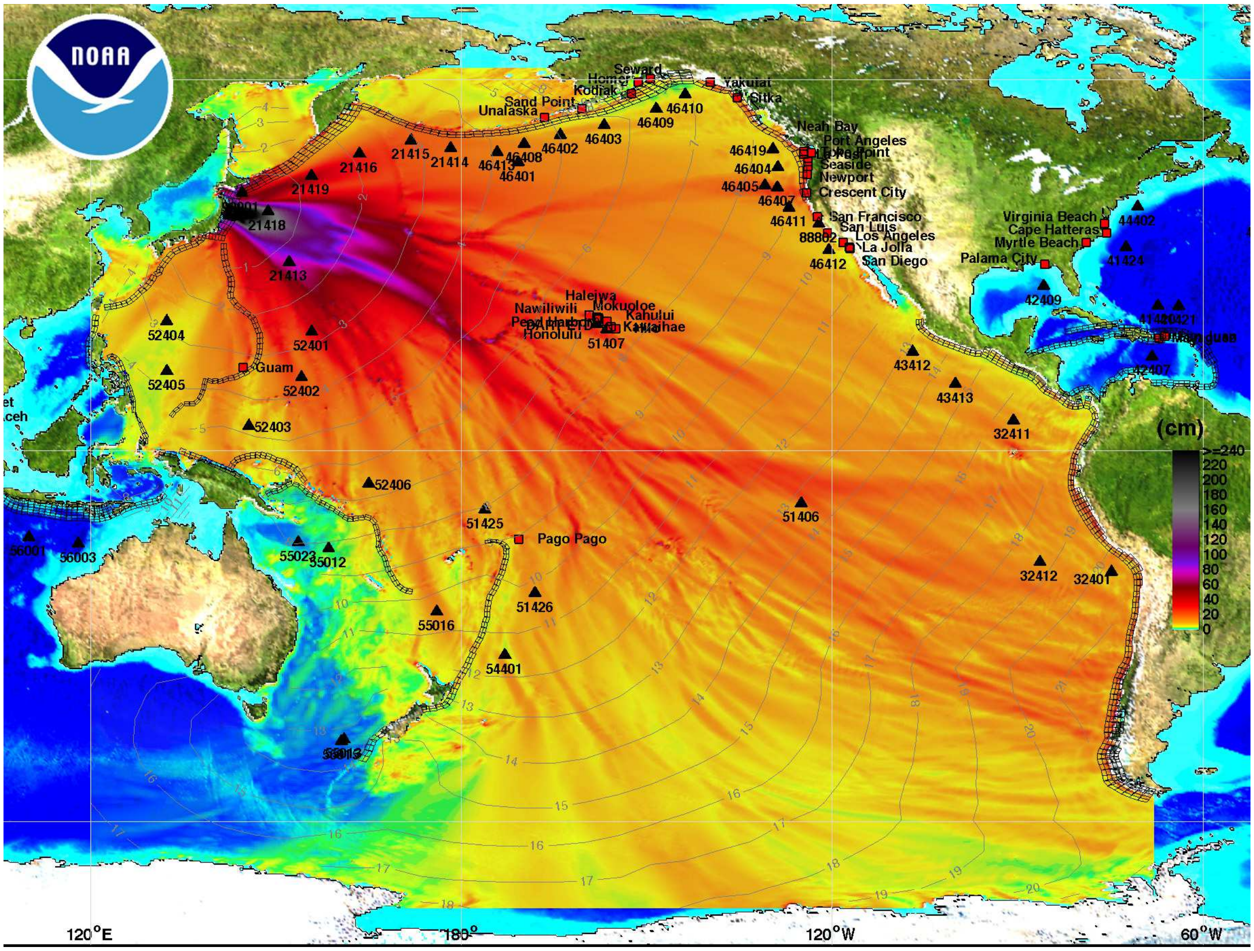

Figure 2. Wave patterns of tsunamis show similar filamental regions of high amplitude as the internal tide. Like the internal tide, these filaments of large amplitude are an artifact of the interference of mulitiple wave patterns.

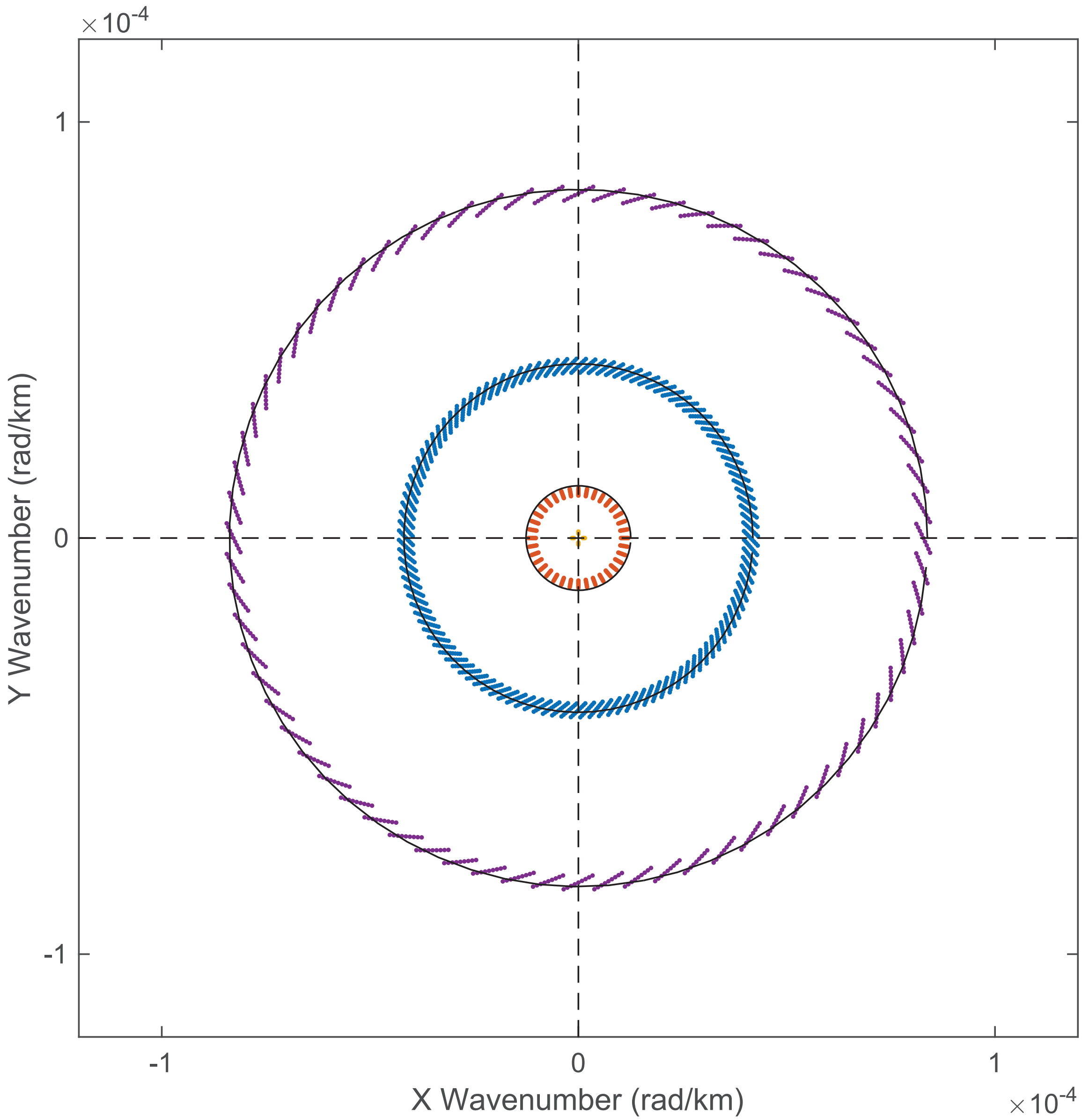

Figure 3. Wavenumbers used for frequency-wavenumber tidal analysis in this report. Magenta: Mode-2 semidiurnal; Blue: Mode-1 semidiurnal; Orange: Mode-1 diurnal; Center: Barotropic. These wavenumbers were determined by trial and error to obtain optimal fits to the along track data, and to give predictions that best matched in situ observations. One aim was to maximize the available wavenumber directions, hence the "twist" to the semidirunal wavenumbers. Another aim was to define a set of wavenumbers that would be universally applicable over the world's oceans, subject to the theoretical wavelengths of any region according to its latitude and stratification. The selection of wavenumbers is constrained by the 6 GB memory available on the Graphics Processing Unit. Wavenumbers with density greater than shown here generally require more memory than is available.

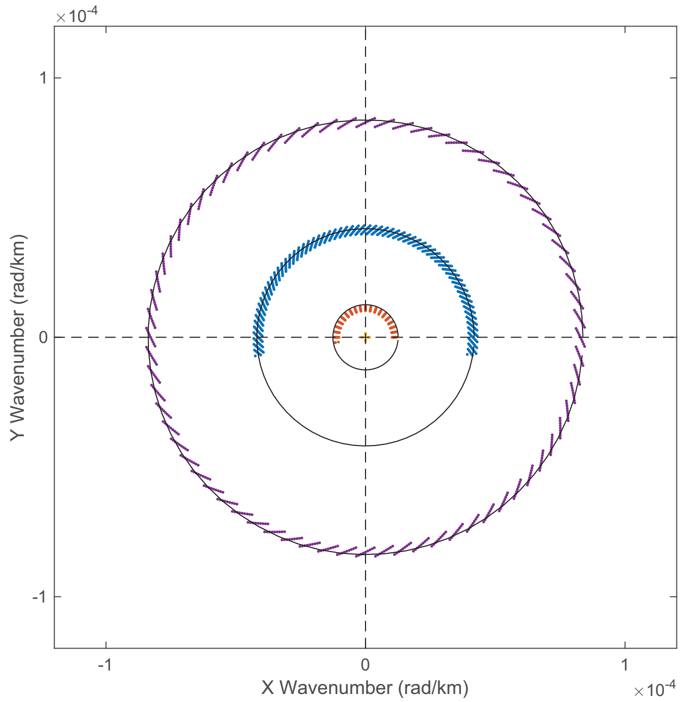

Figure 4. Wavenumbers used for determining the "northward" wavenumber content of the semidiurnal radiating internal tide. These are a subset of the wavenumbers used for the omnidirectional set shown in Figure 2. Mode-1 semidiurnal wavenumbers are indicated in blue as in Figure 2.

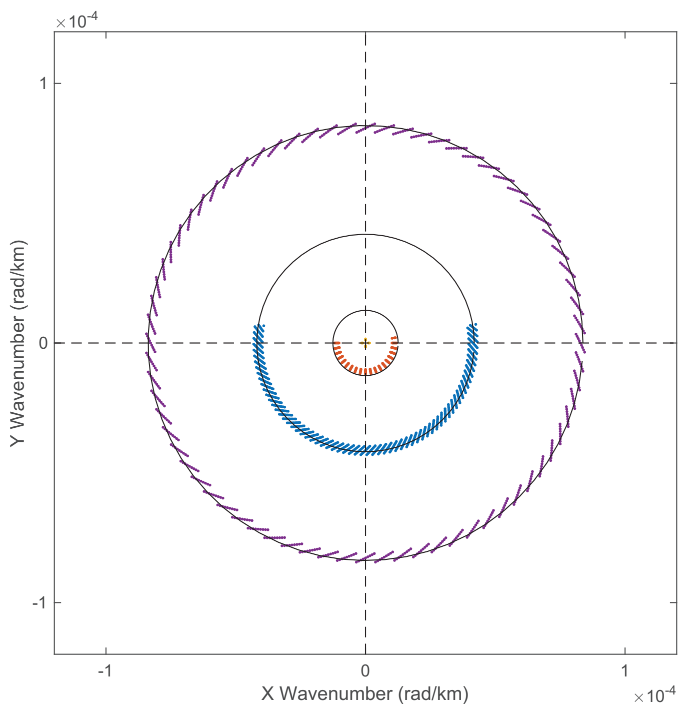

Figure 5. Wavenumbers used for determining the "southward" wavenumber content of the semidiurnal radiating internal tide. These are a subset of the wavenumbers used for the omnidirectional set shown in Figure 2. Mode-1 semidiurnal wavenumbers are indicated in blue as in Figure 2.

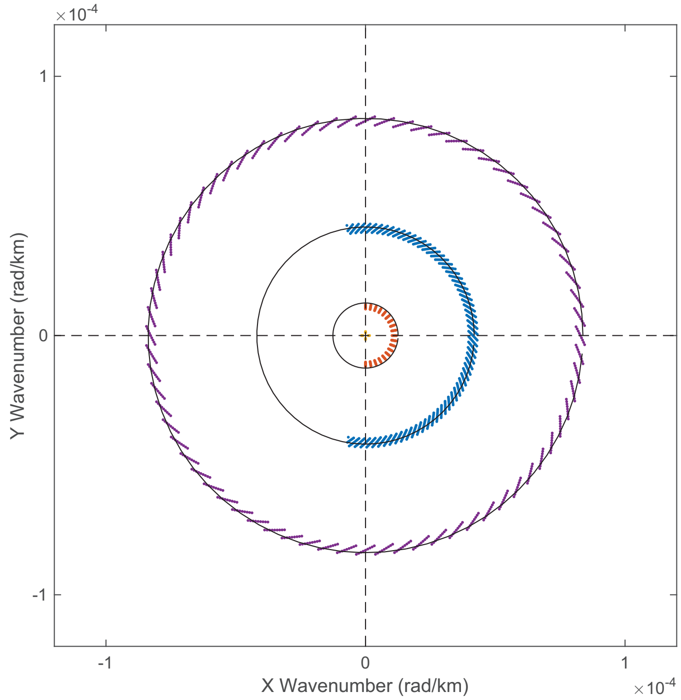

Figure 6. Wavenumbers used for determining the "eastward" wavenumber content of the semidiurnal radiating internal tide. These are a subset of the wavenumbers used for the omnidirectional set shown in Figure 2. Mode-1 semidiurnal wavenumbers are indicated in blue as in Figure 2.

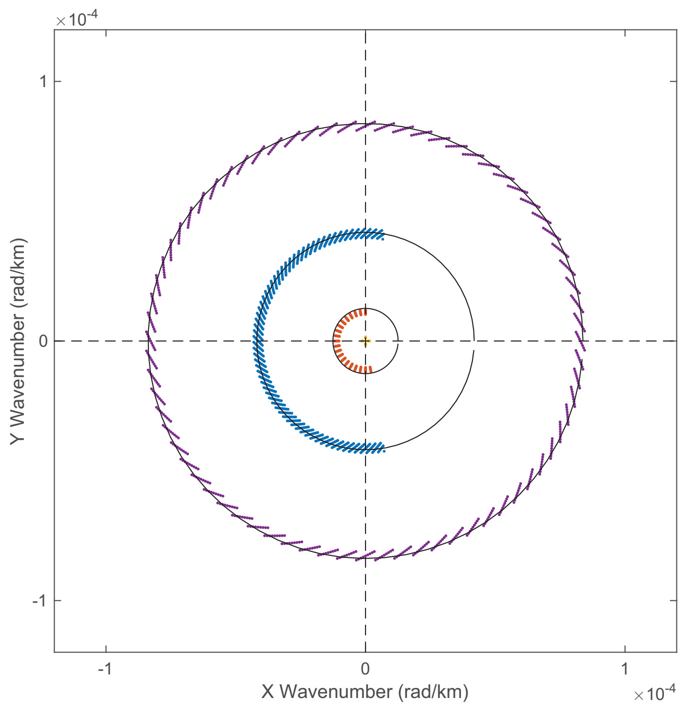

Figure 7. Wavenumbers used for determining the "westward" wavenumber content of the semidiurnal radiating internal tide. These are a subset of the wavenumbers used for the omnidirectional set shown in Figure 2. Mode-1 semidiurnal wavenumbers are indicated in blue as in Figure 2.

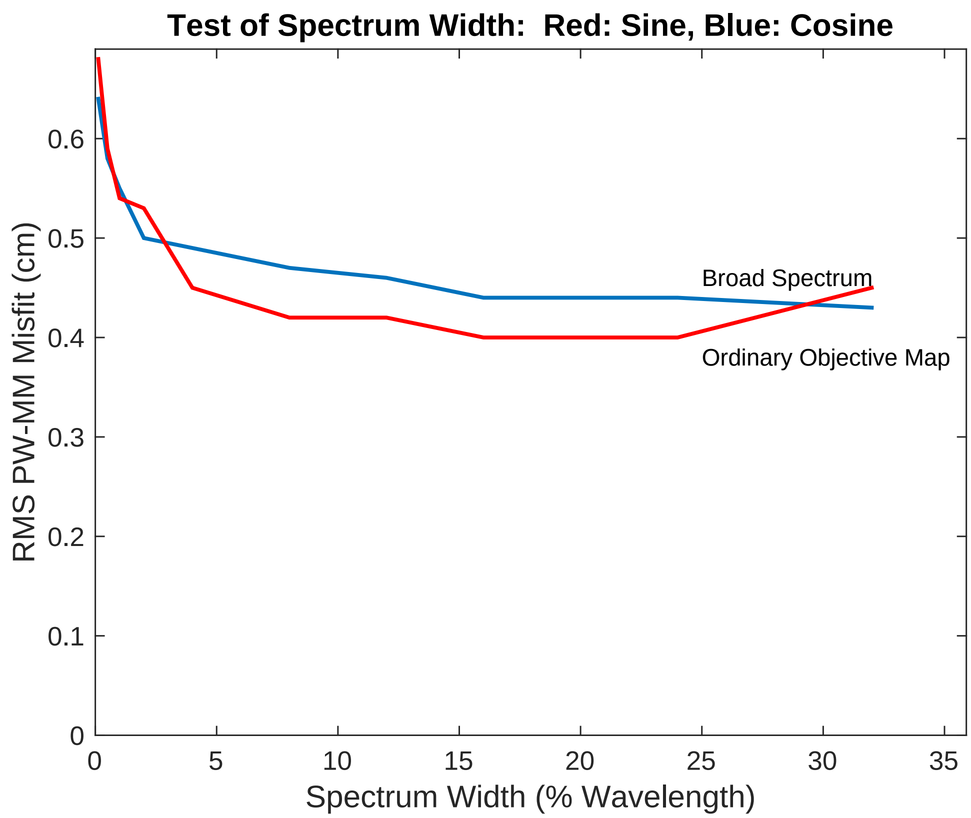

Figure 8. An experiment to determine sensitivity of the fit to spectrum bandwidth. RMS misfit between along-track, point-wise harmonic constants and frequency-wavenumber tidal analysis were computed. The M_2 internal tide north of Hawaii was used for this computation. Red corresponds to the sine component (A sin(G)), blue corresponds to the cosine component (A cos(G)). The fit improves with increasing bandwidth until 5% of semidiurnal wavelength, after which the fit improves very little. The optimal fit is therefore obtained for a narrowband spectrum with bandwidth corresponding to 5% of the mode-1 wavelength. The "point-wise" estimates are not really the gold standard, however, since they have significant error contributions, from, e.g., mesoscale aliasing; perfect agreement is not expected. We do not want to fit variance inconsistent with the dispersion relation. When the assumed bandwidth is large, the fit begins to resemble an ordinary objective map.

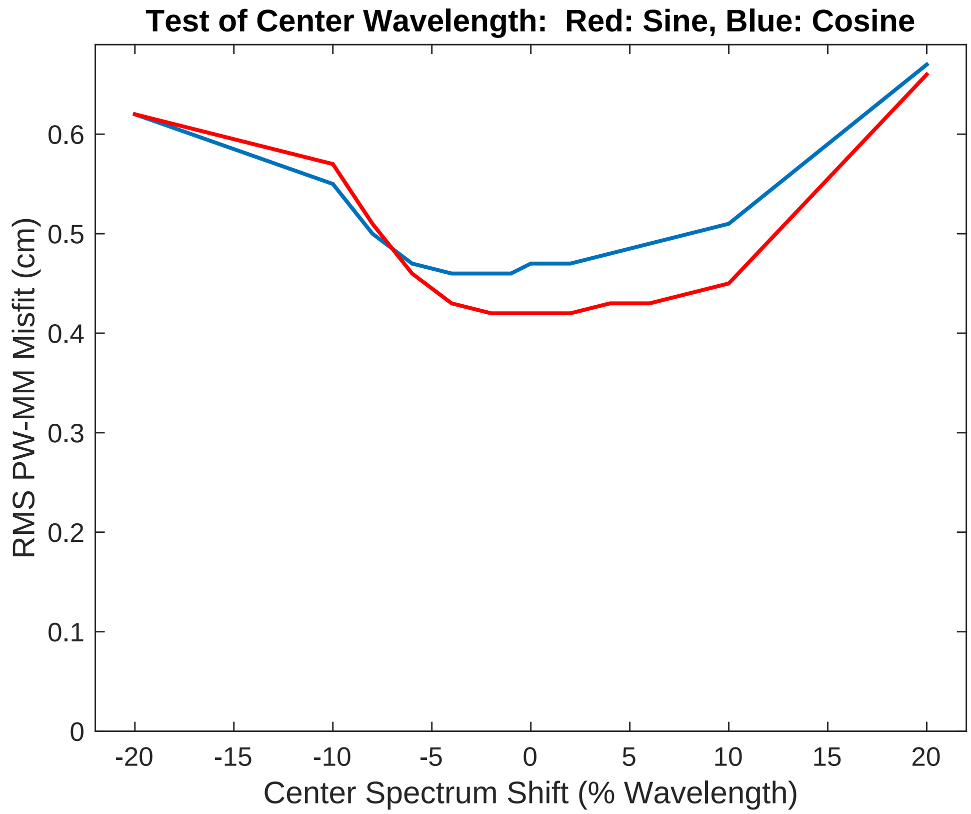

Figure 9. An experiment to determine how closely the observations correspond to the theoretical wavelength for the semidiurnal internal tide. As in Figure 7, the RMS misfit between along-track, point-wise harmonic constants and frequency-wavenumber tidal analysis were computed. The M_2 internal tide north of Hawaii was used for this computation. The optimal fit is obtained when the center wavenumber is within about 5% of the theoretically-expected wavenumber (which corresponds to 0% center spectrum shift) are used.

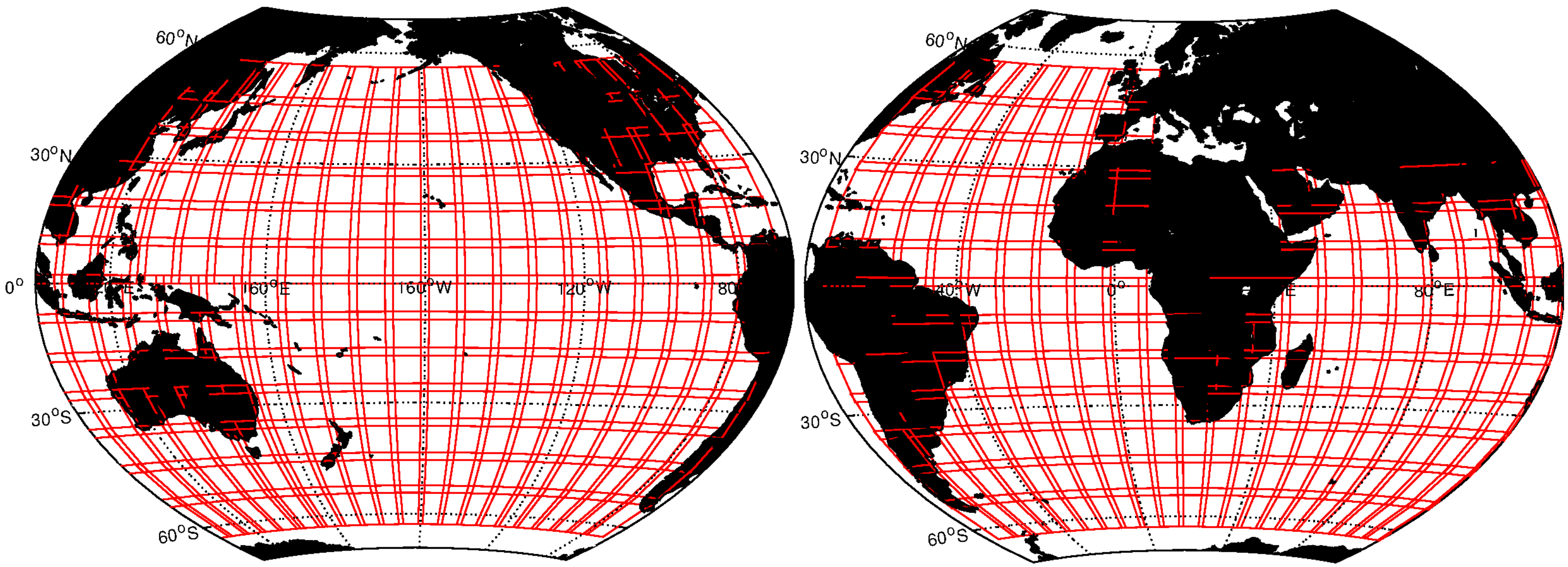

Figure 10. To compute the global maps of internal tides, the ocean basins were divided into 11°×11° squares that overlap by 1°. Each side of the globe spans 195°. Hammer-Aitoff Projections.

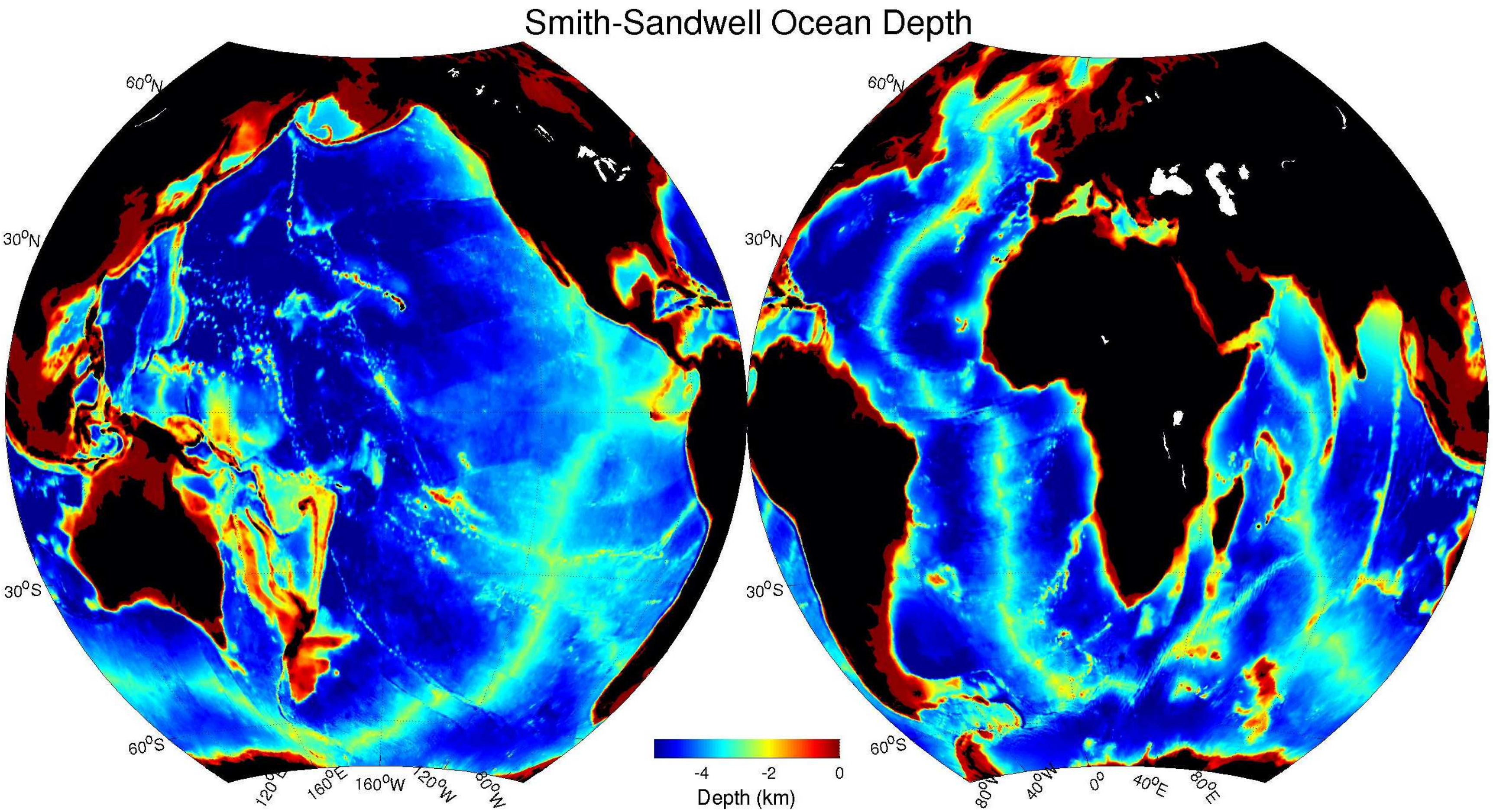

Figure 11. The ocean seafloor topography as modeled by Smith and Sandwell, version 8.2. The model is 0.25 degree resolution, but only a coarse 1.0 degree resolution is required here. Each side of the globe spans 195°. Hammer-Aitoff Projections.

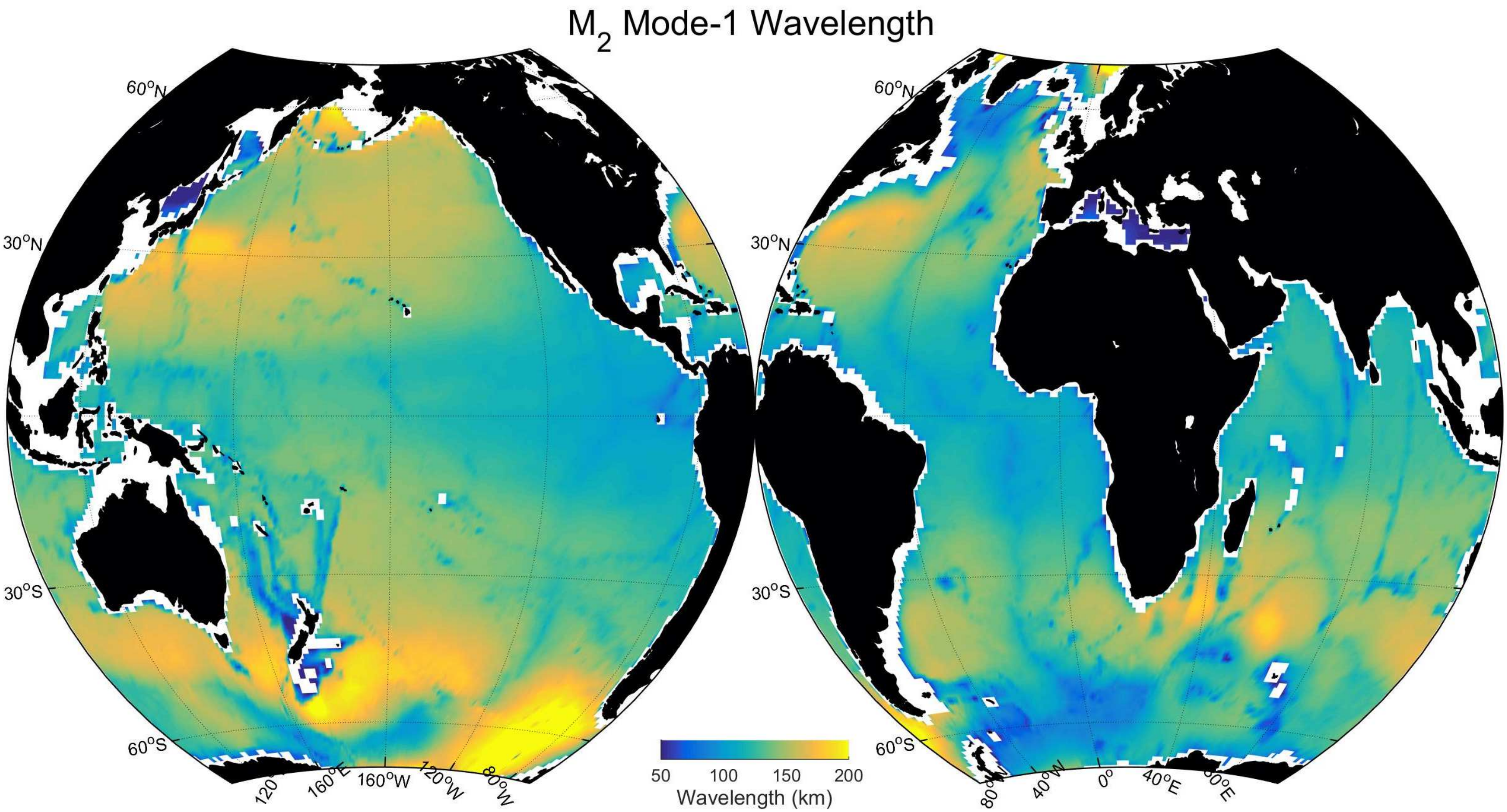

Figure 12. M_2, mode-1 wavelength derived from the 2009 World Ocean Atlas.

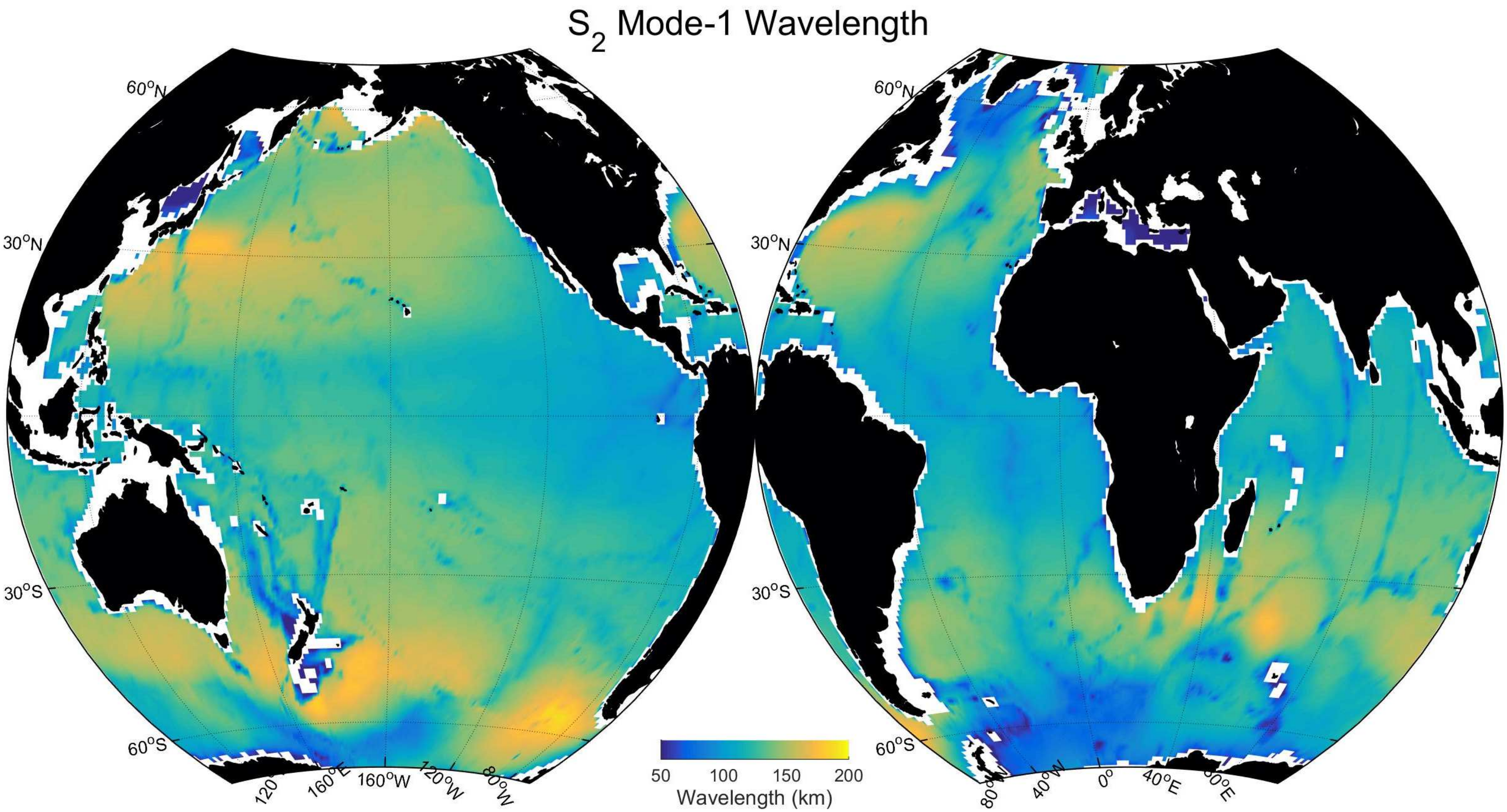

Figure 13. S_2, mode-1 wavelength derived from the 2009 World Ocean Atlas.

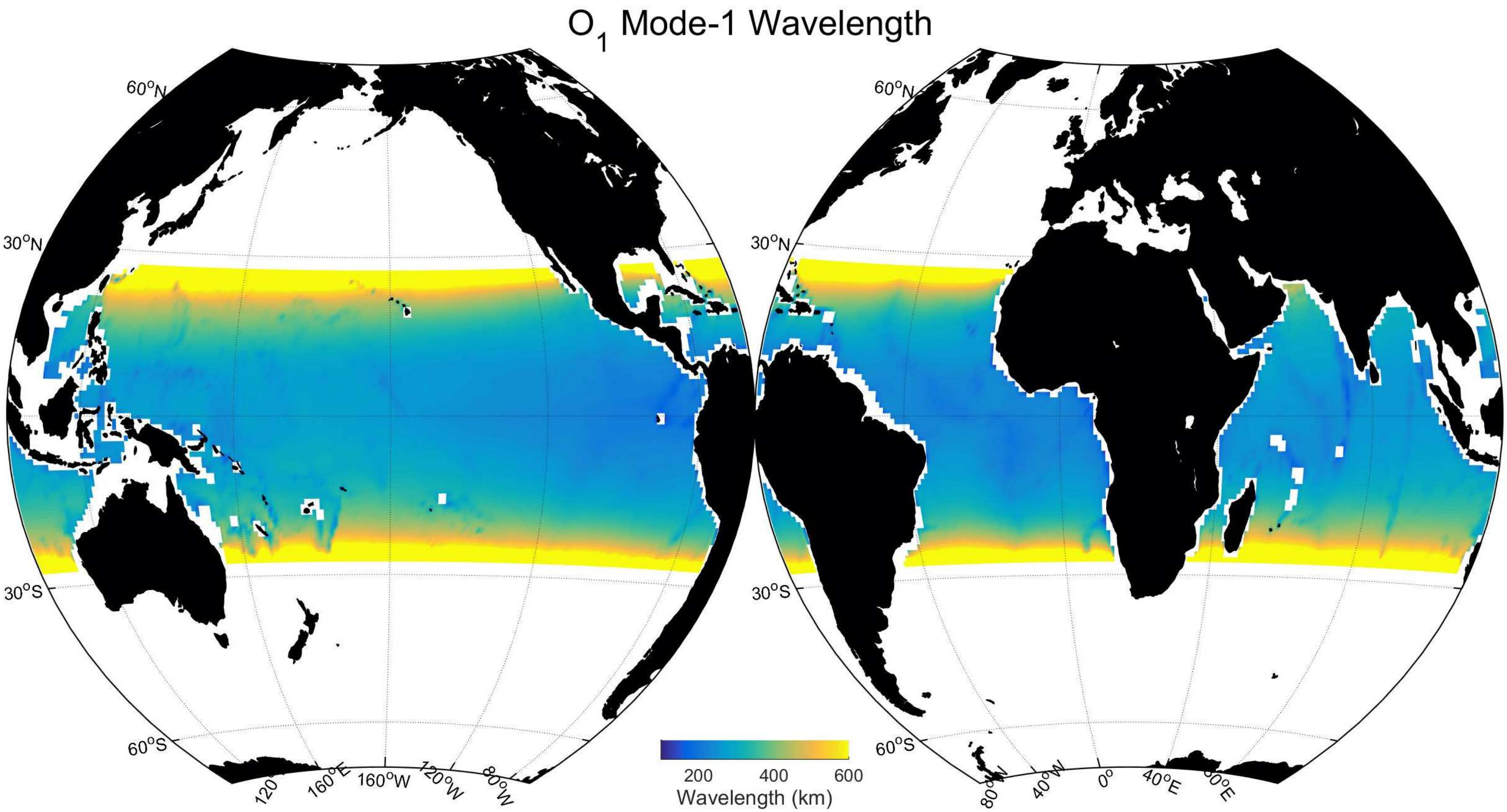

Figure 14. O_1, mode-1 wavelength derived from the 2009 World Ocean Atlas.

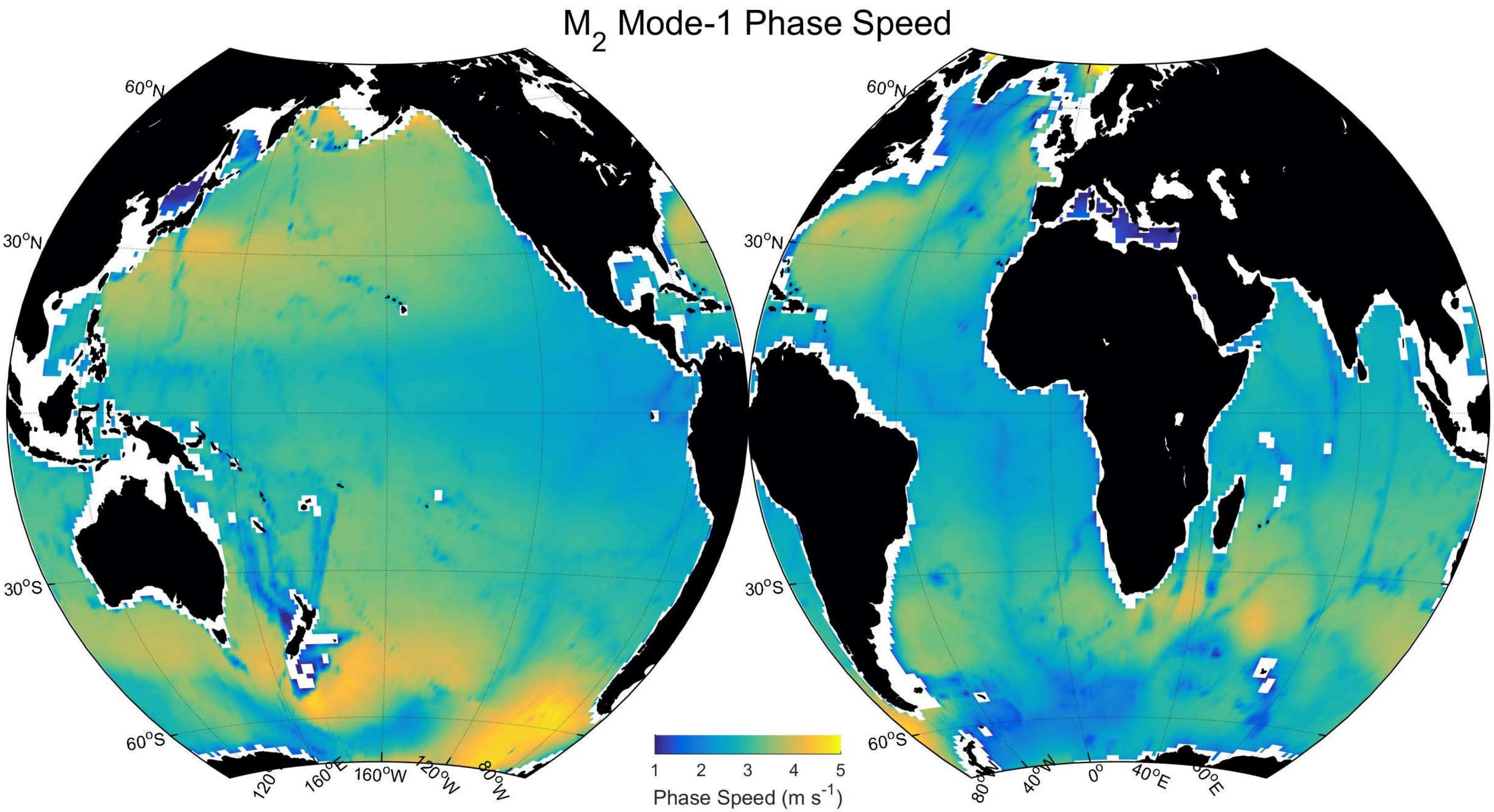

Figure 15. M_2, mode-1 phase speed derived from the 2009 World Ocean Atlas.

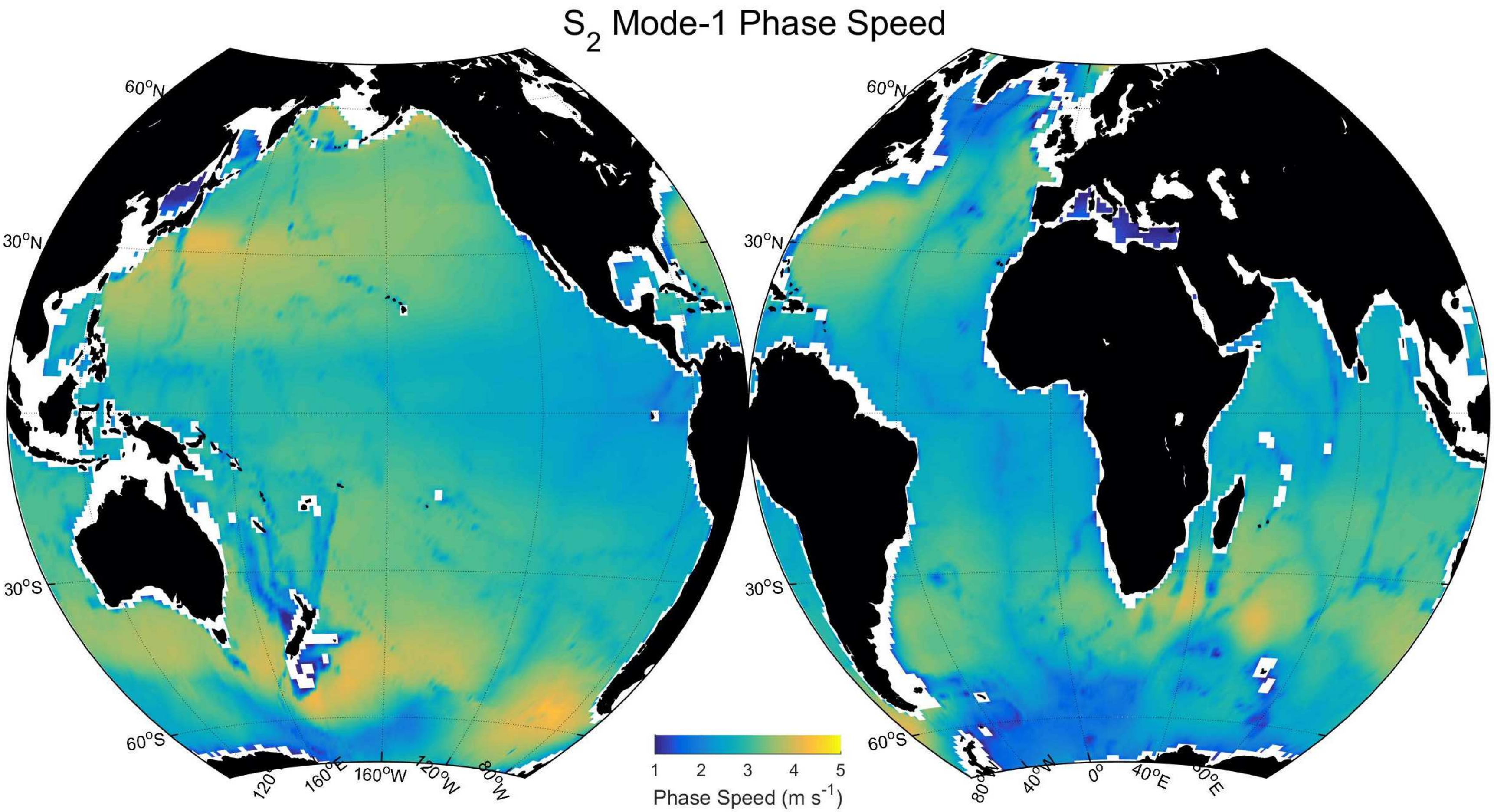

Figure 16. S$_2$, mode-1 phase speed derived from the 2009 World Ocean Atlas.

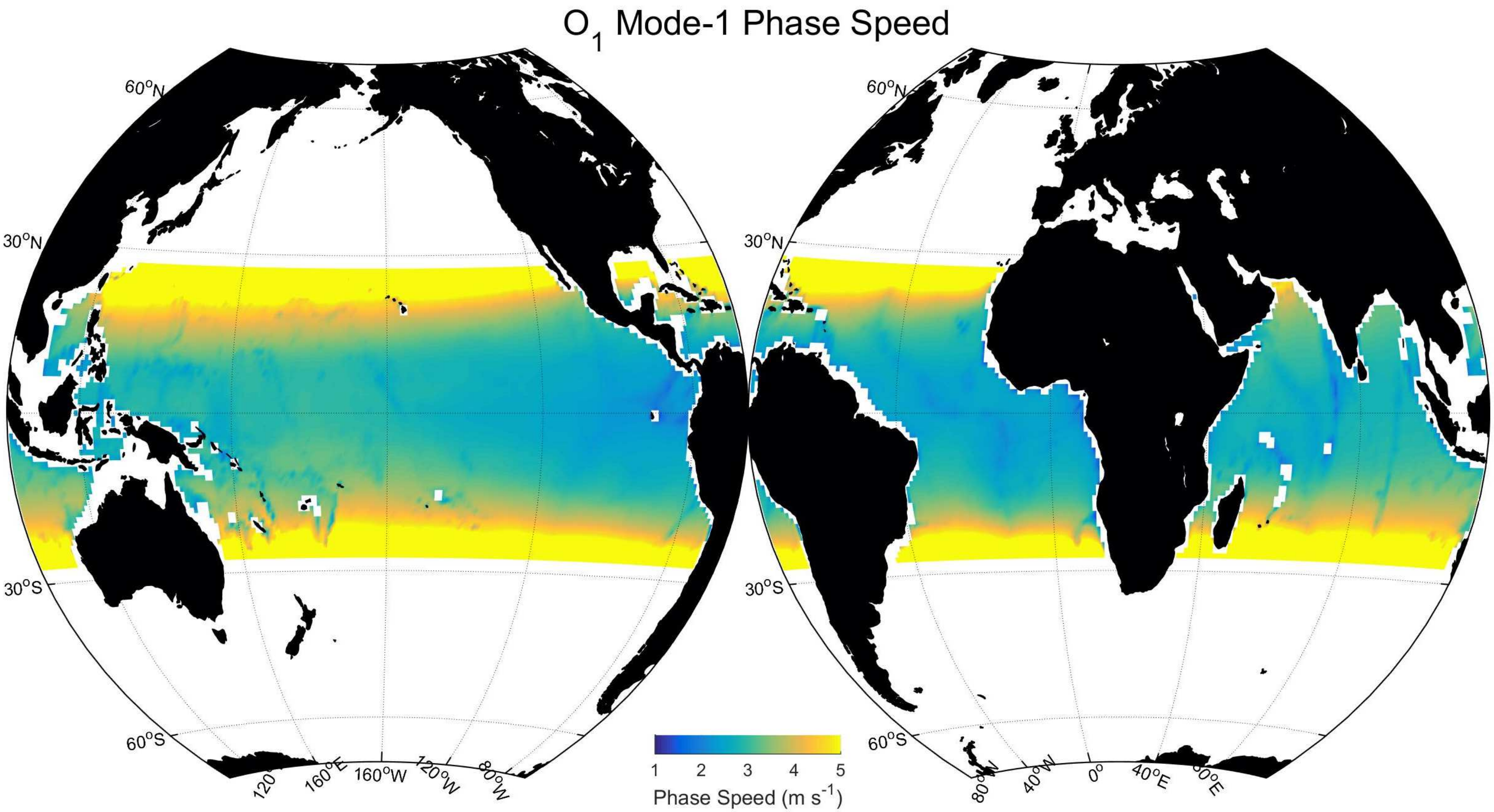

Figure 17. O_1, mode-1 phase speed derived from the 2009 World Ocean Atlas.

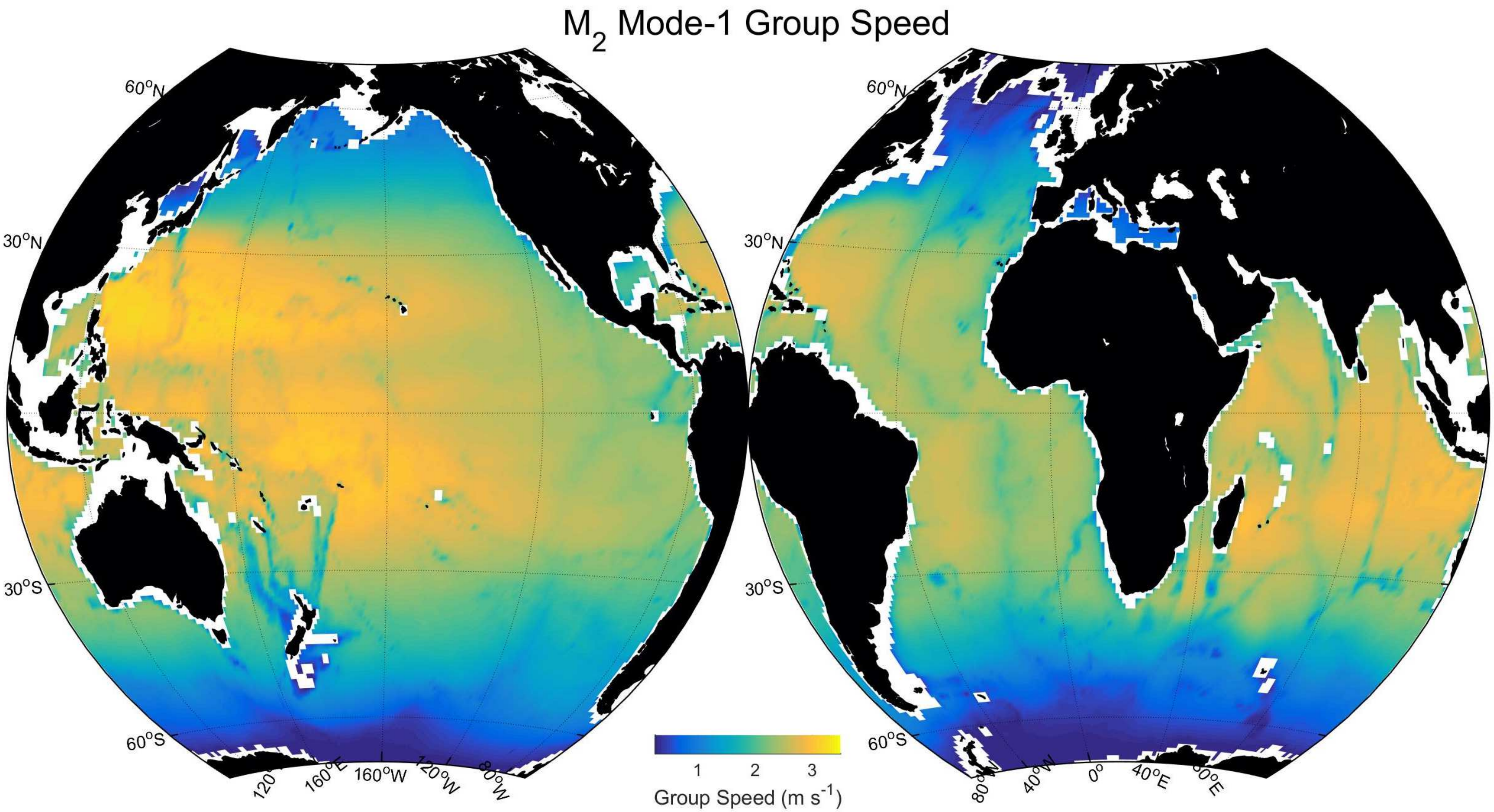

Figure 18. M_2, mode-1 group speed derived from the 2009 World Ocean Atlas.

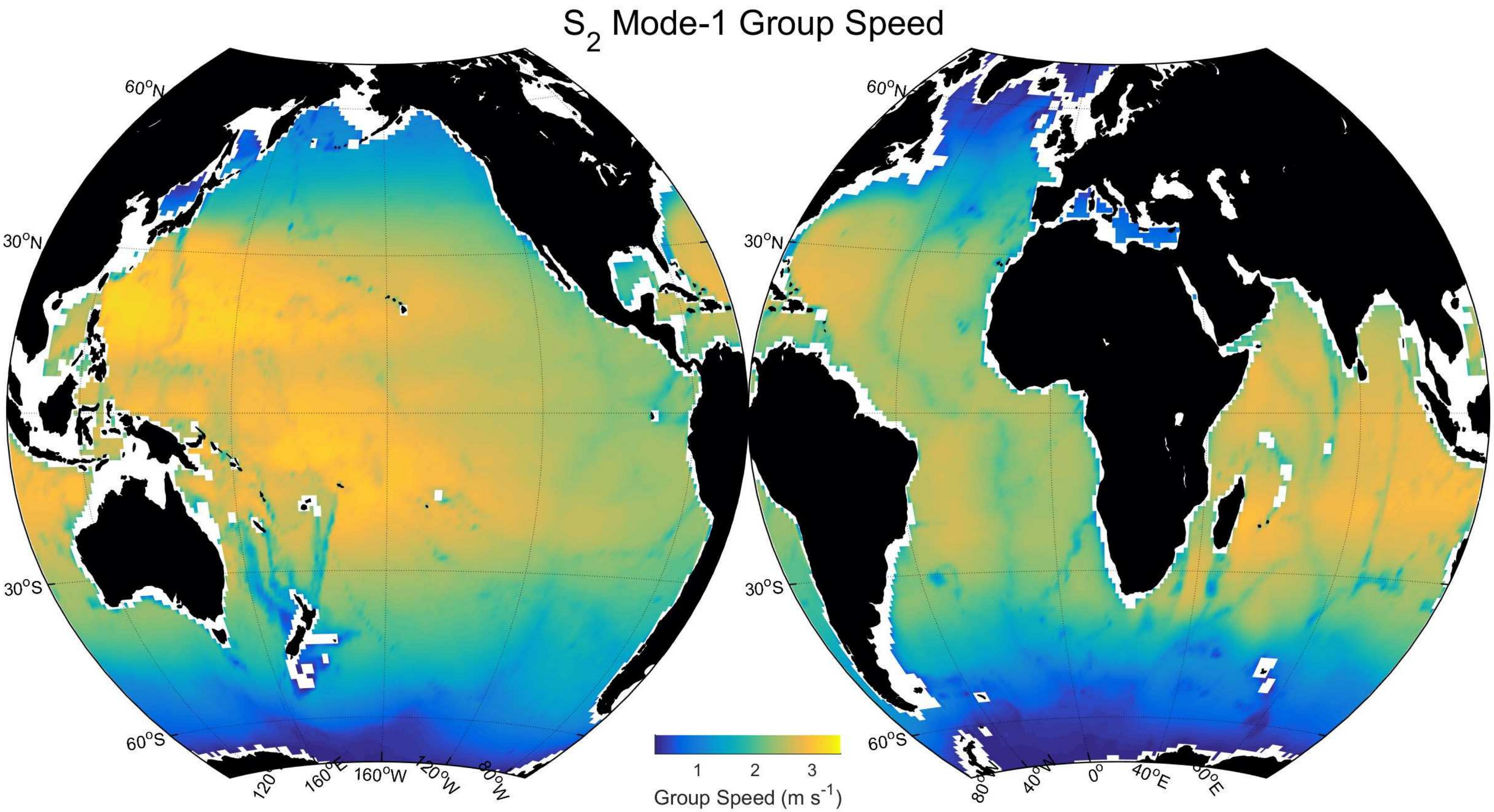

Figure 19. S_2, mode-1 group speed derived from the 2009 World Ocean Atlas.

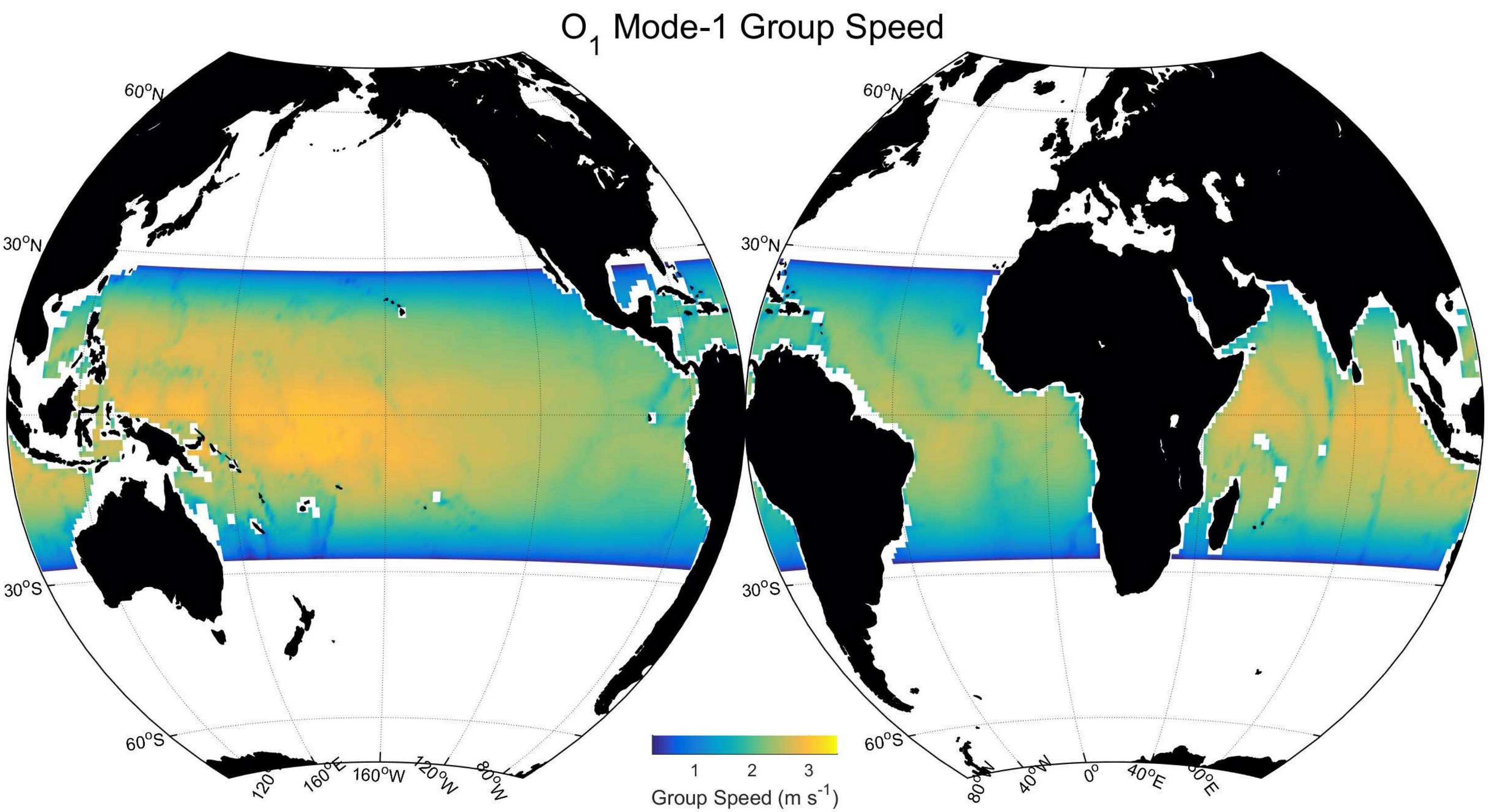

Figure 20. O_1, mode-1 group speed derived from the 2009 World Ocean Atlas.

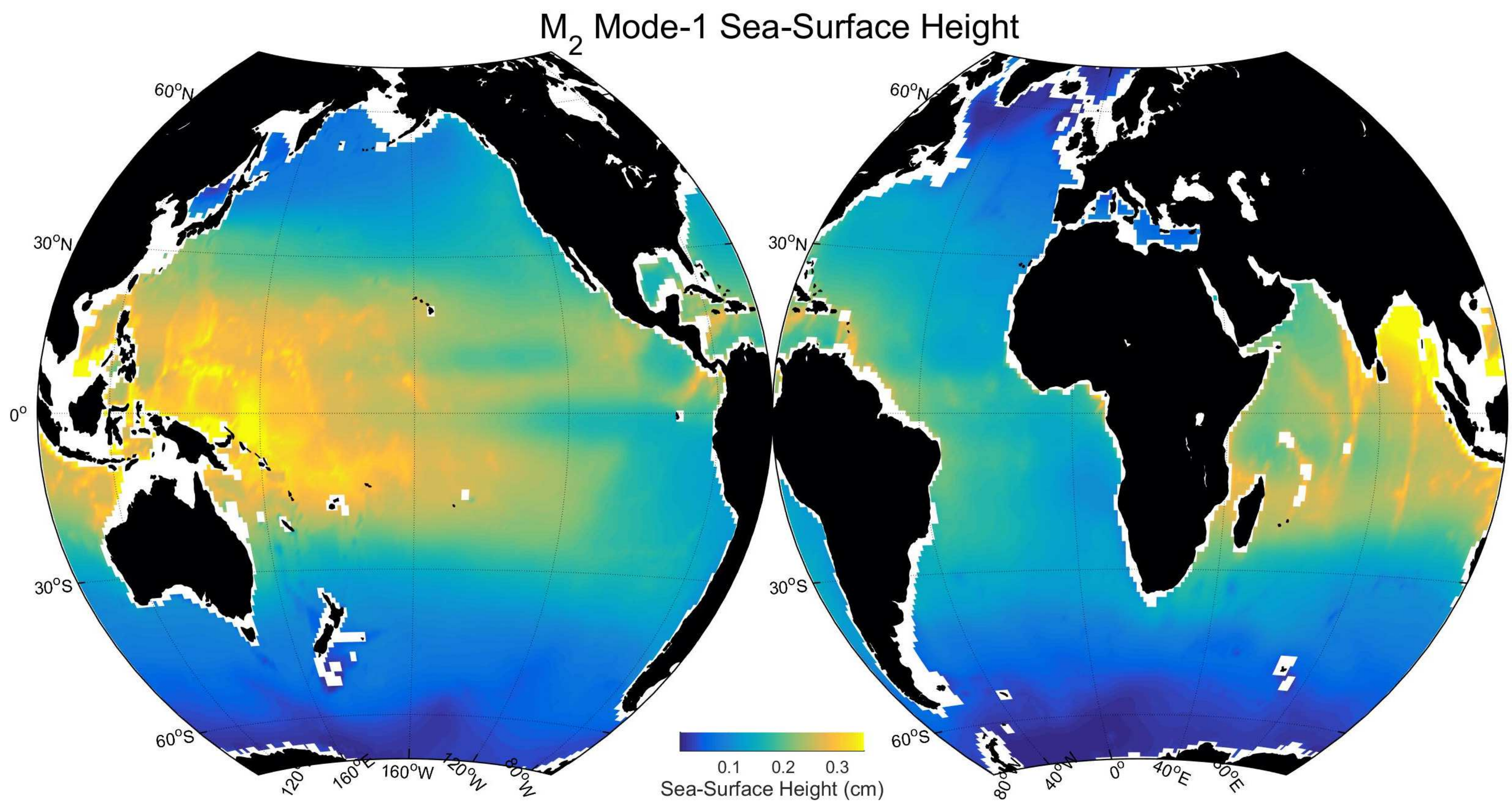

Figure 21. The sea-surface height expression of an M_2, mode-1 internal tide with unit amplitude derived from the 2009 World Ocean Atlas.

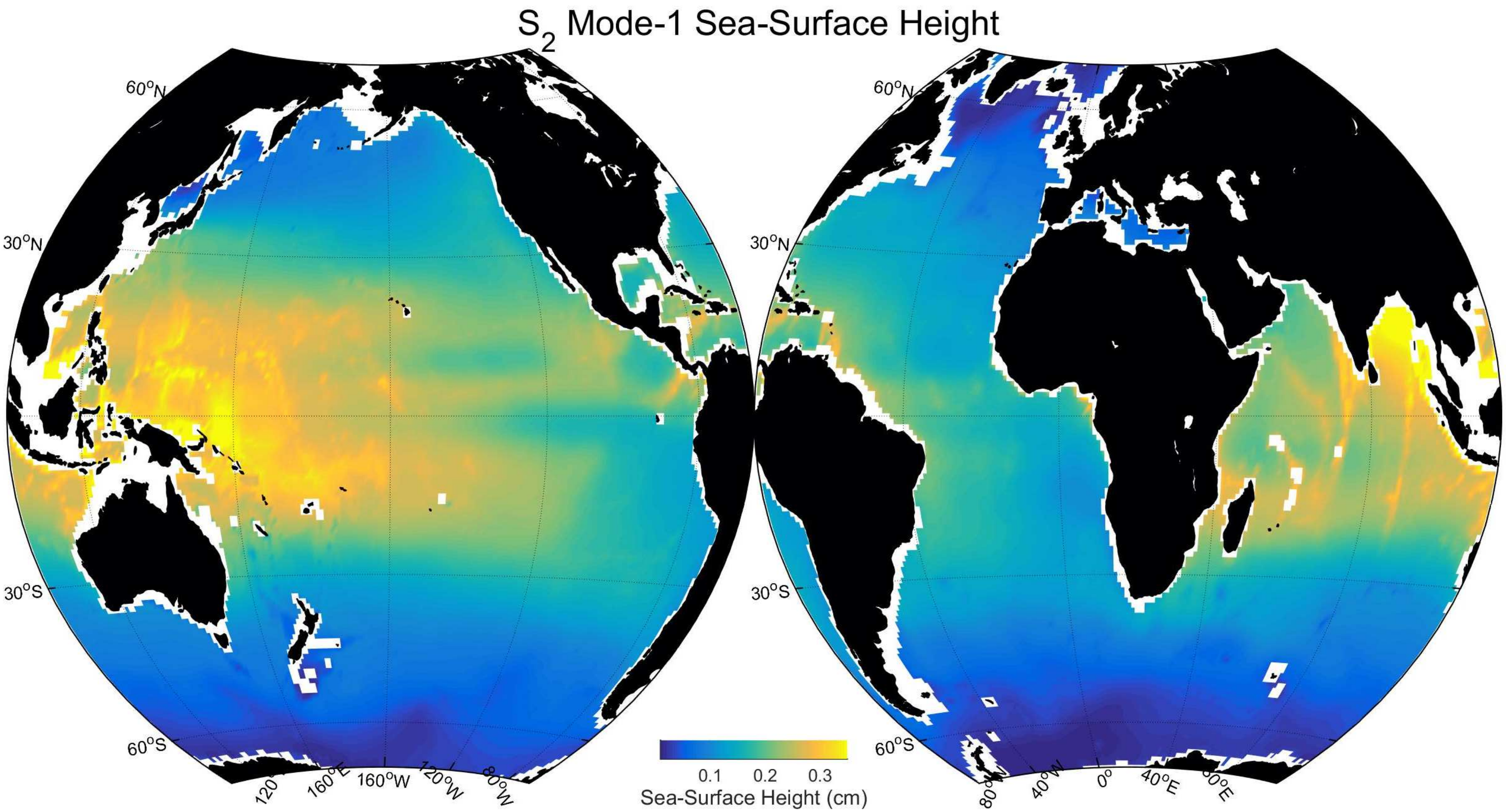

Figure 22. The sea-surface height expression of an S_2, mode-1 internal tide with unit amplitude derived from the 2009 World Ocean Atlas.

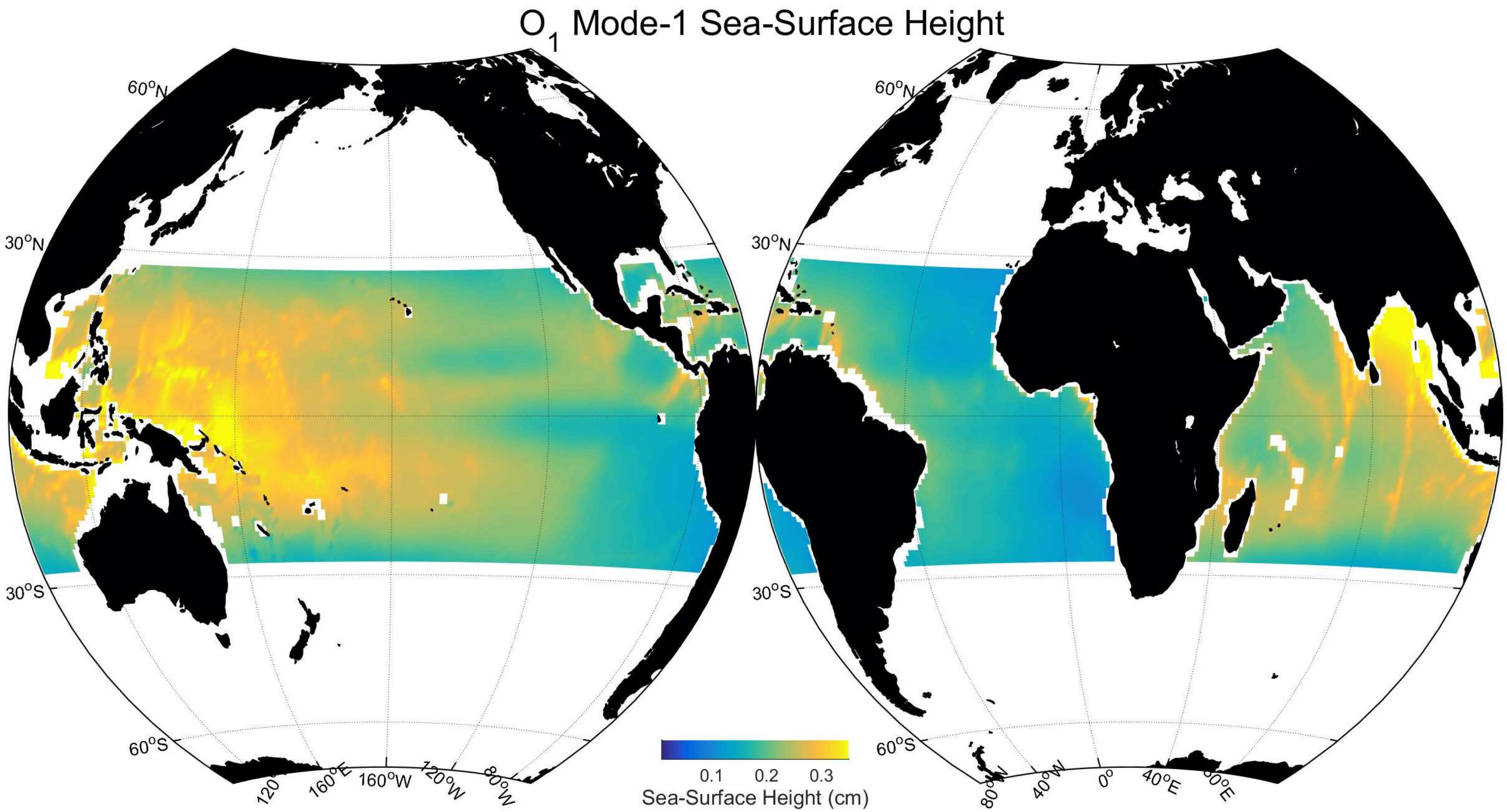

Figure 23. The sea-surface height expression of an O_1, mode-1 internal tide with unit amplitude derived from the 2009 World Ocean Atlas.

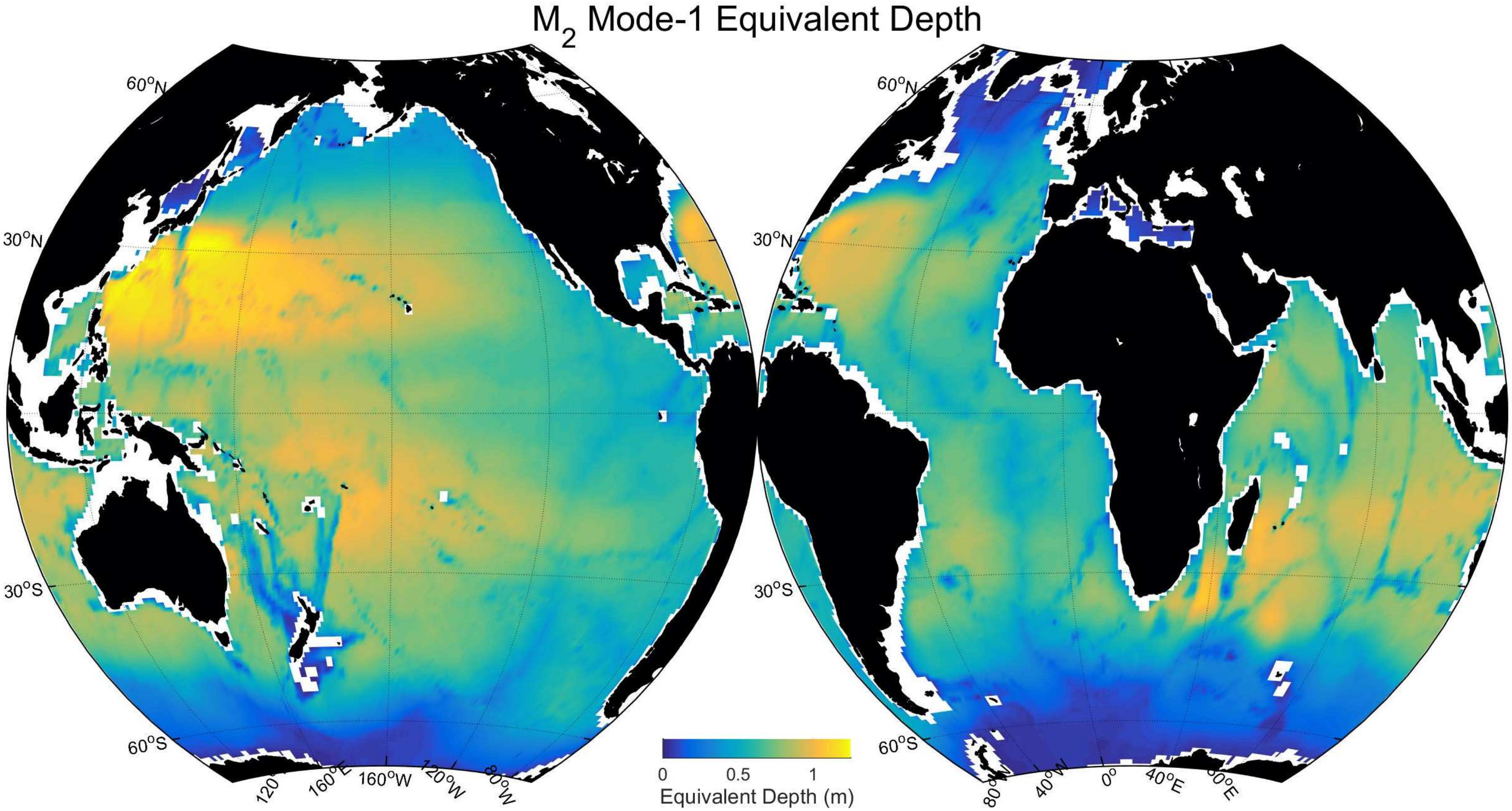

Figure 24. The equivalent depth for the M_2, mode-1 internal tide derived from the 2009 World Ocean Atlas.

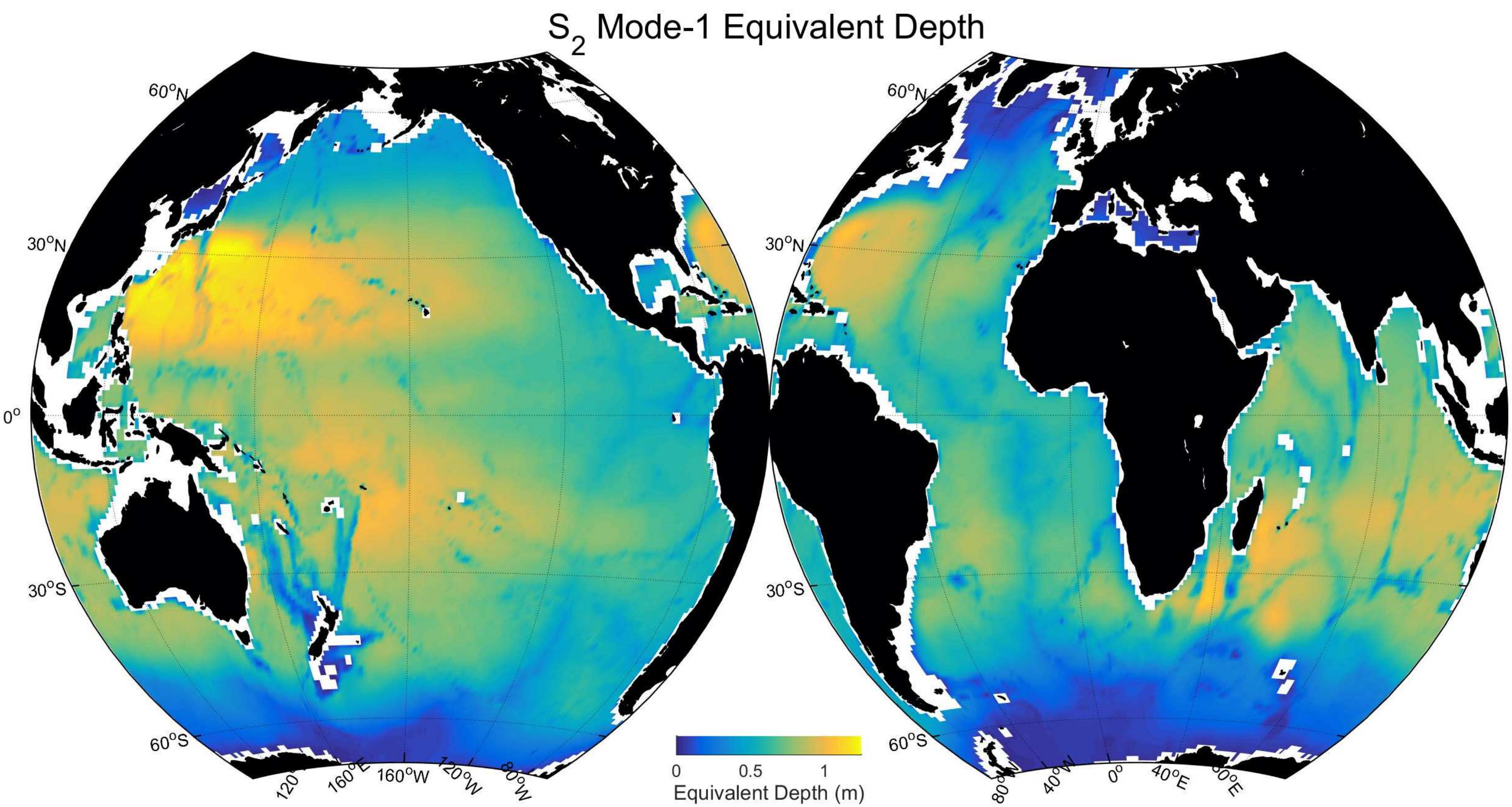

Figure 25. The equivalent depth for the S_2, mode-1 internal tide derived from the 2009 World Ocean Atlas.

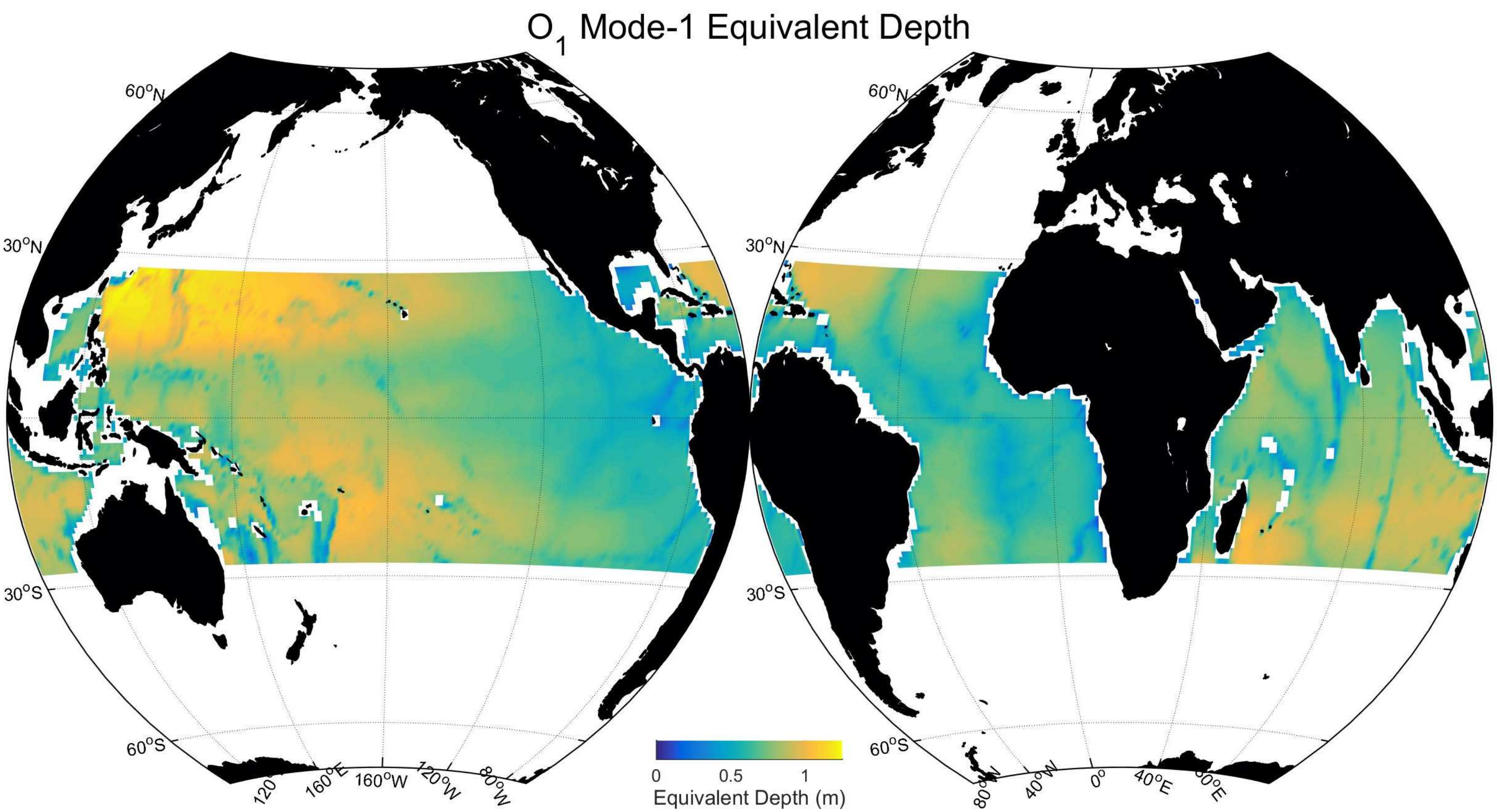

Figure 26. The equivalent depth for the O_1, mode-1 internal tide derived from the 2009 World Ocean Atlas.

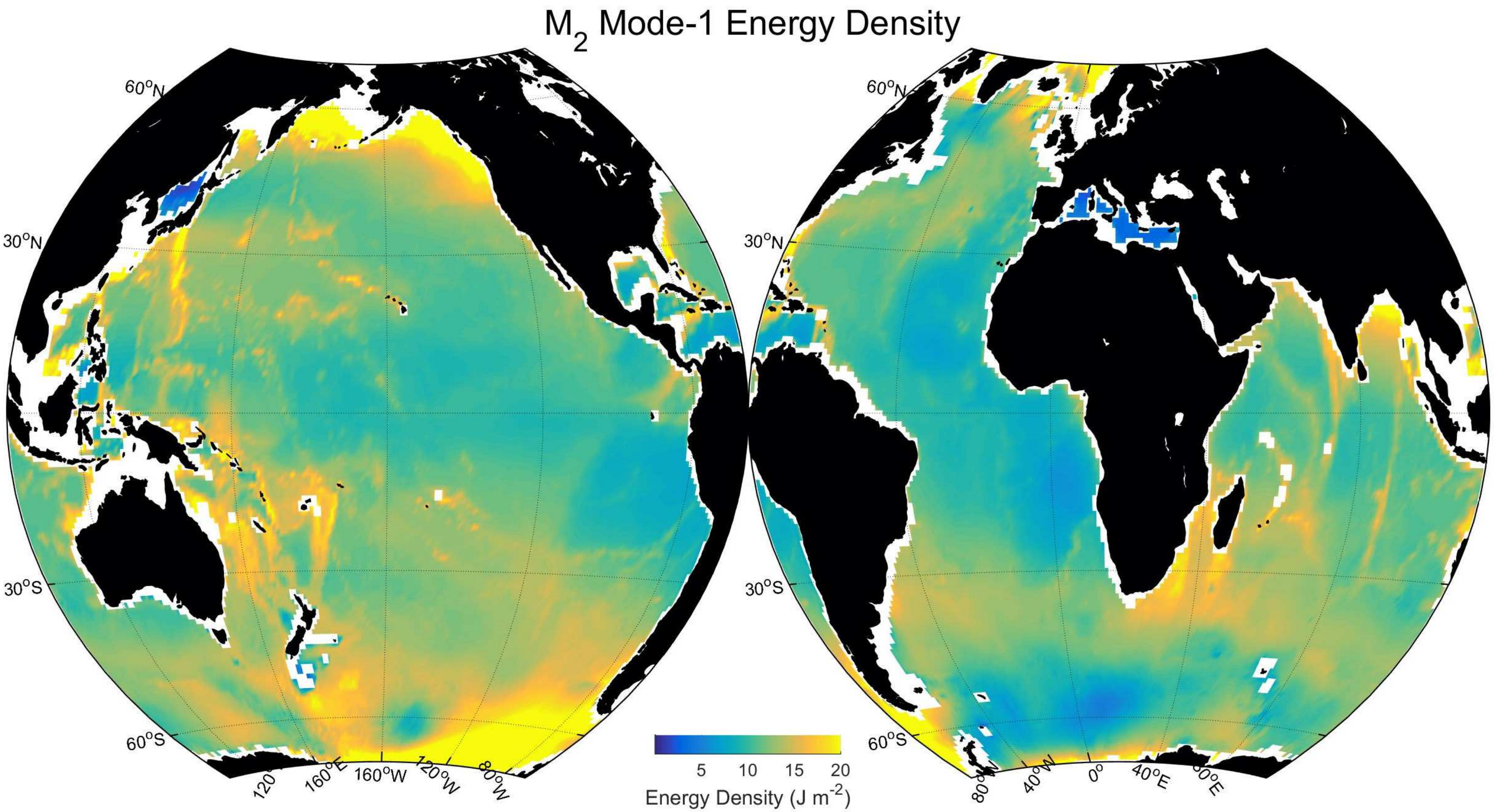

Figure 27. The energy density for an M_2, mode-1 internal tide with unit amplitude derived from the 2009 World Ocean Atlas.

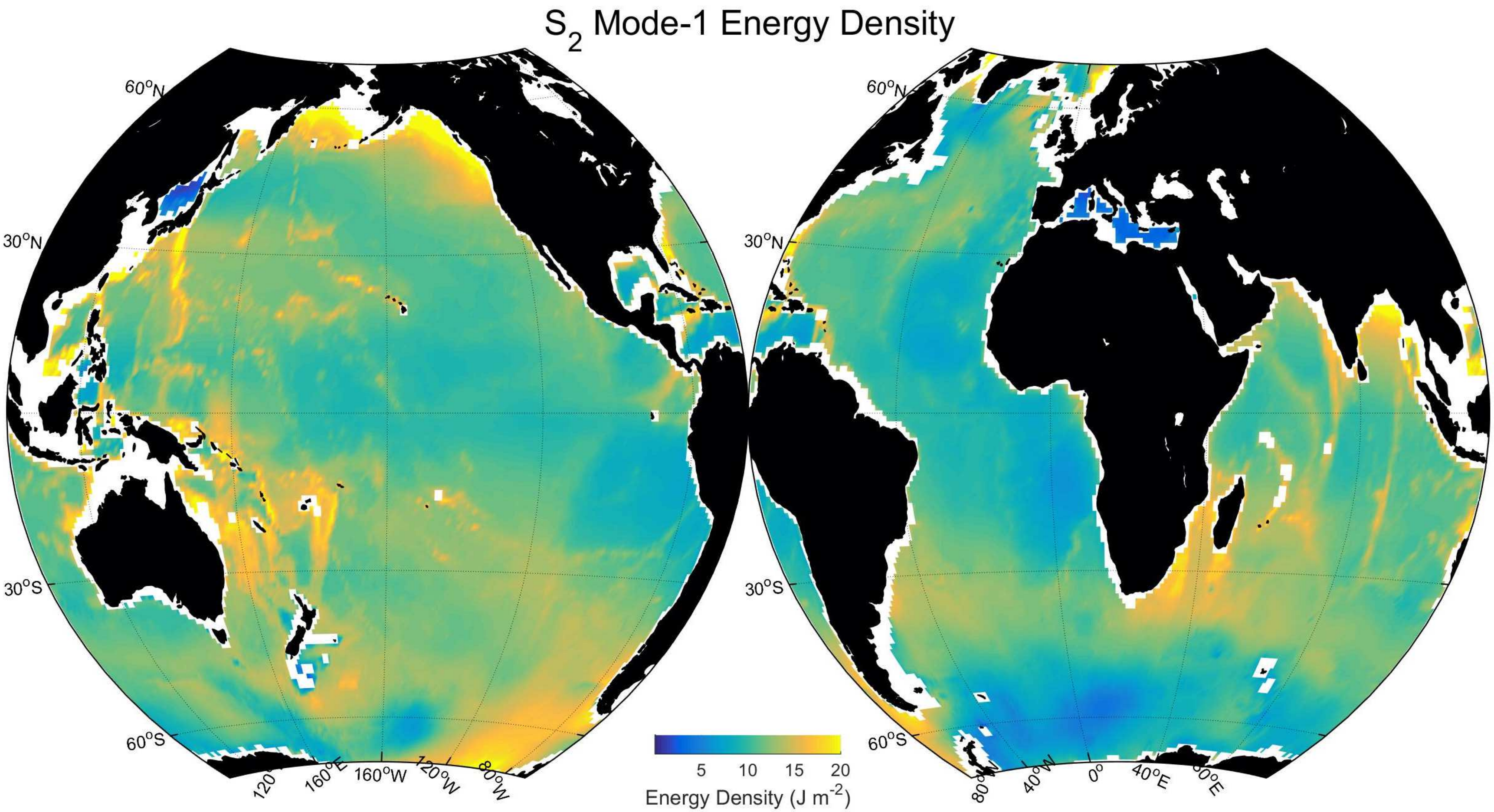

Figure 28. The energy density for an S_2, mode-1 internal tide with unit amplitude derived from the 2009 World Ocean Atlas.

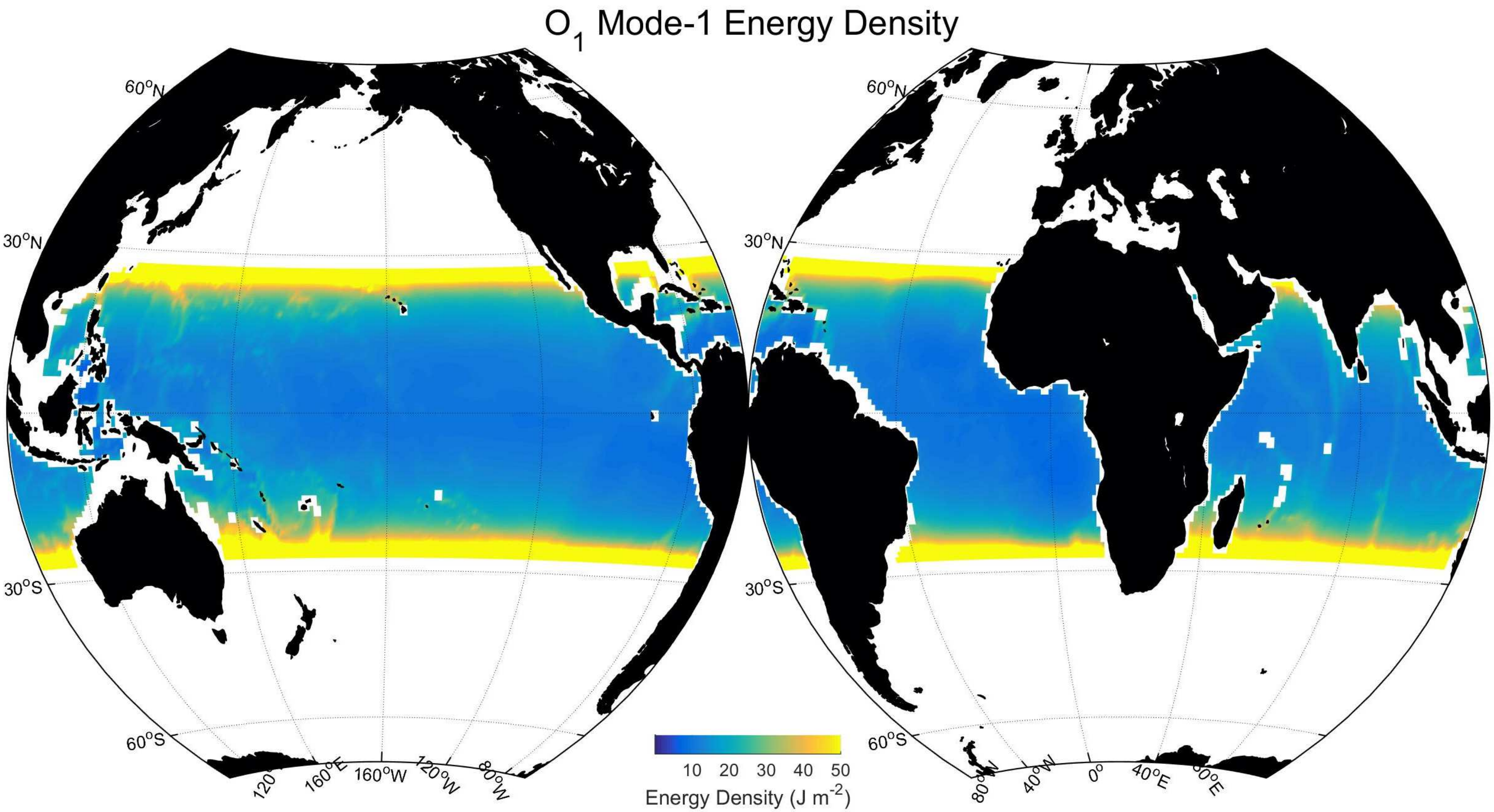

Figure 29. The energy density for an O_1, mode-1 internal tide with unit amplitude derived from the 2009 World Ocean Atlas.

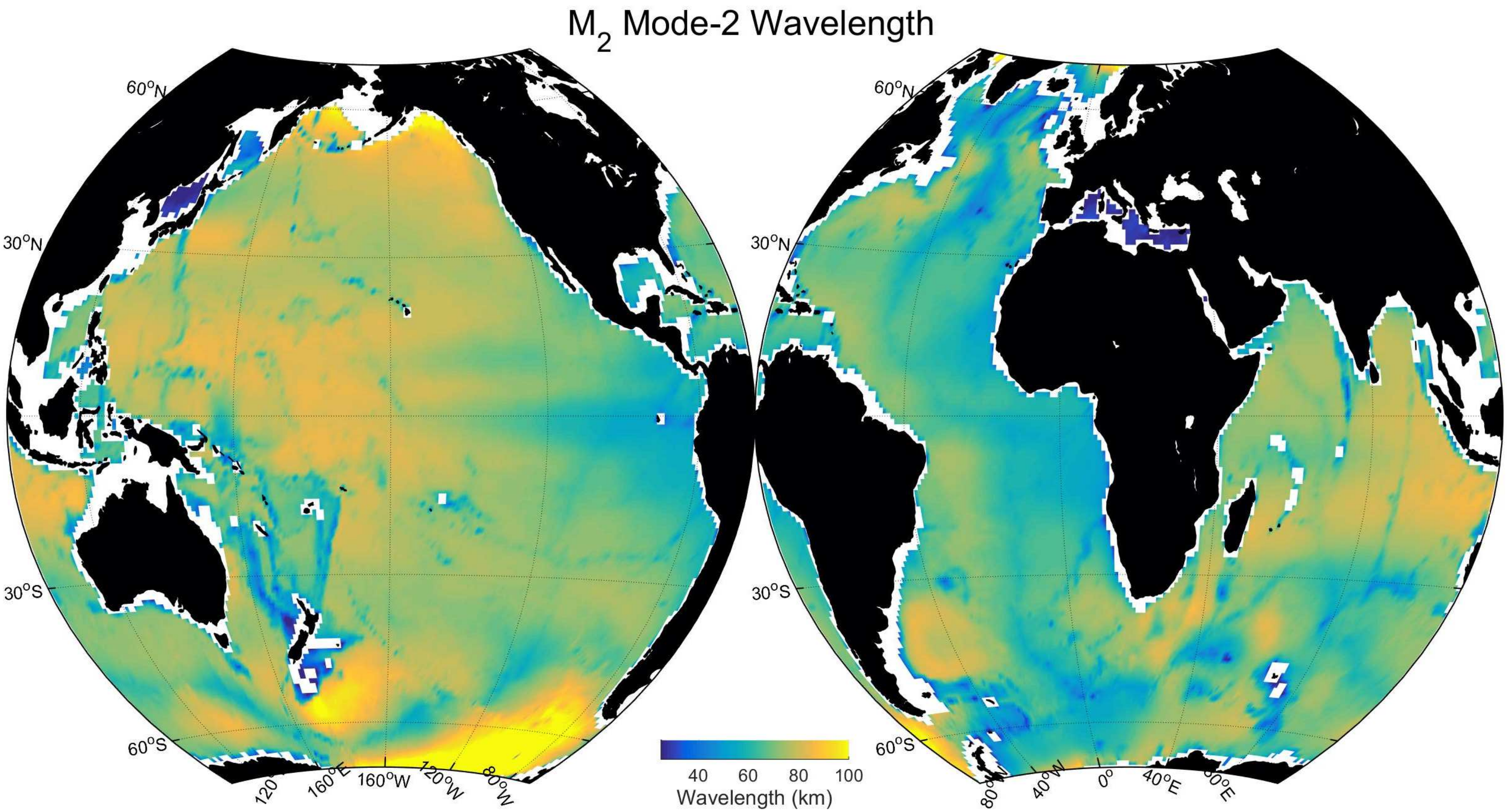

Figure 30. M_2, mode-2 wavelength derived from the 2009 World Ocean Atlas.

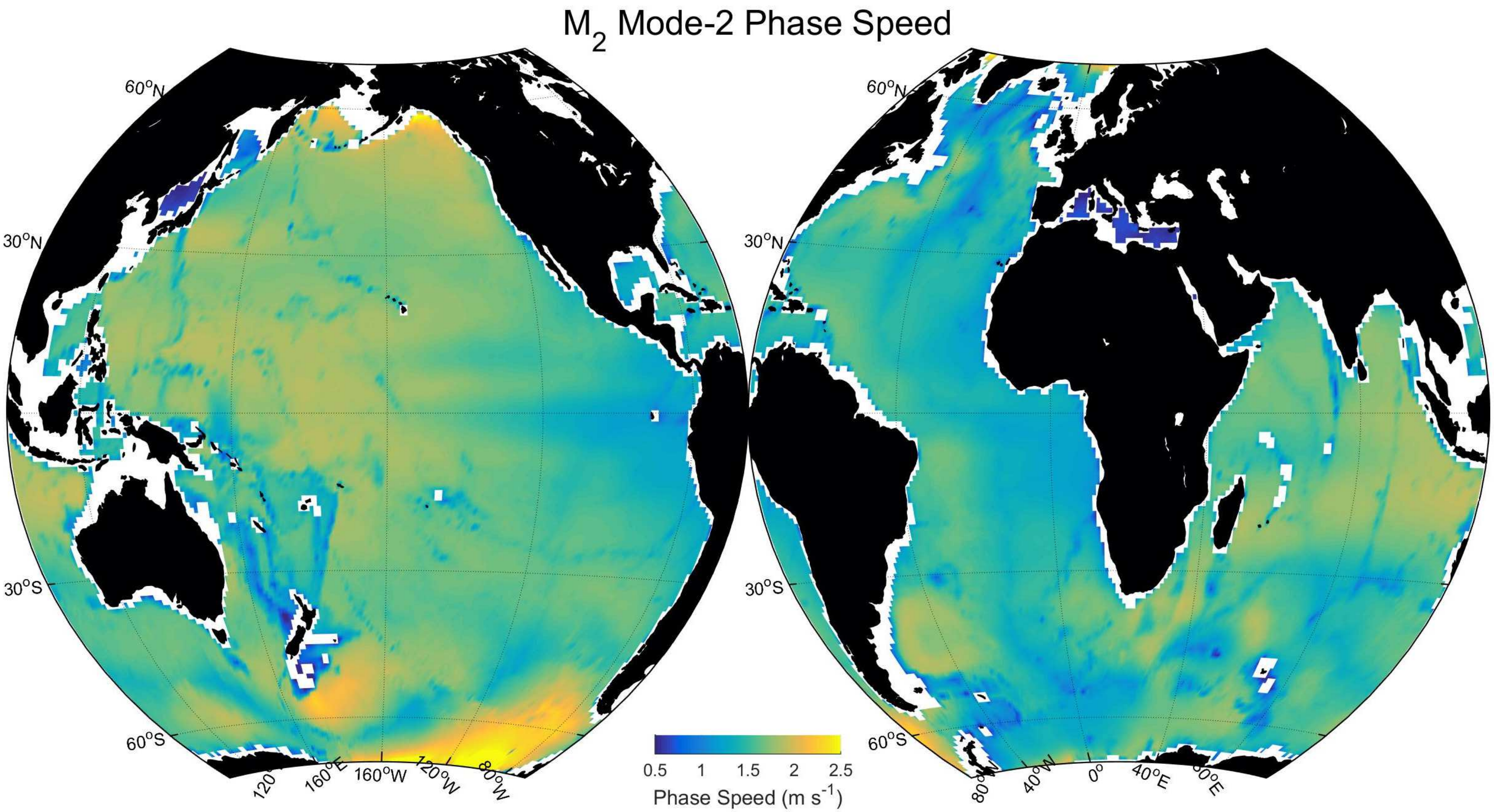

Figure 31. M_2, mode-2 phase speed derived from the 2009 World Ocean Atlas.

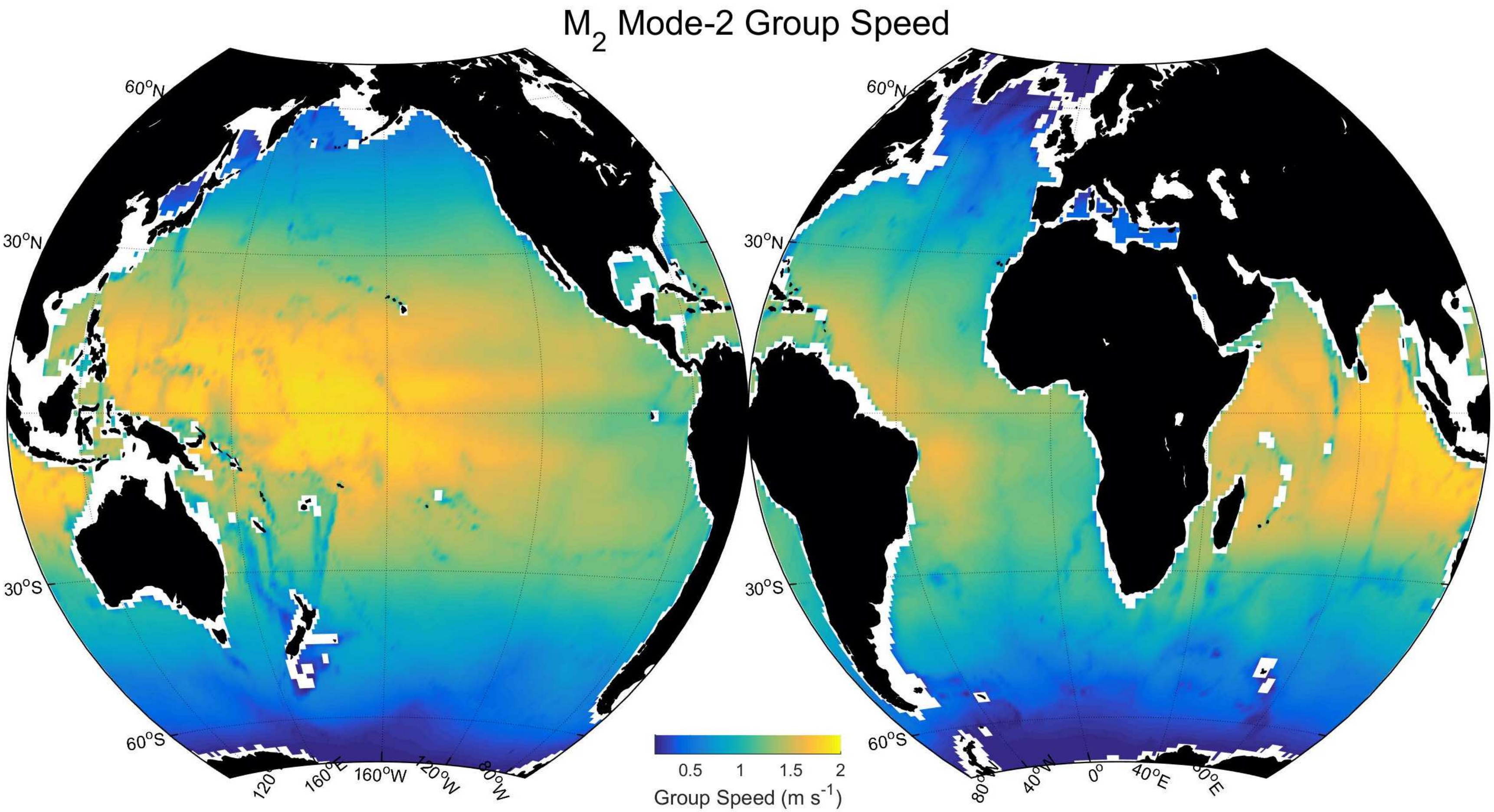

Figure 32. M_2, mode-2 group speed derived from the 2009 World Ocean Atlas.

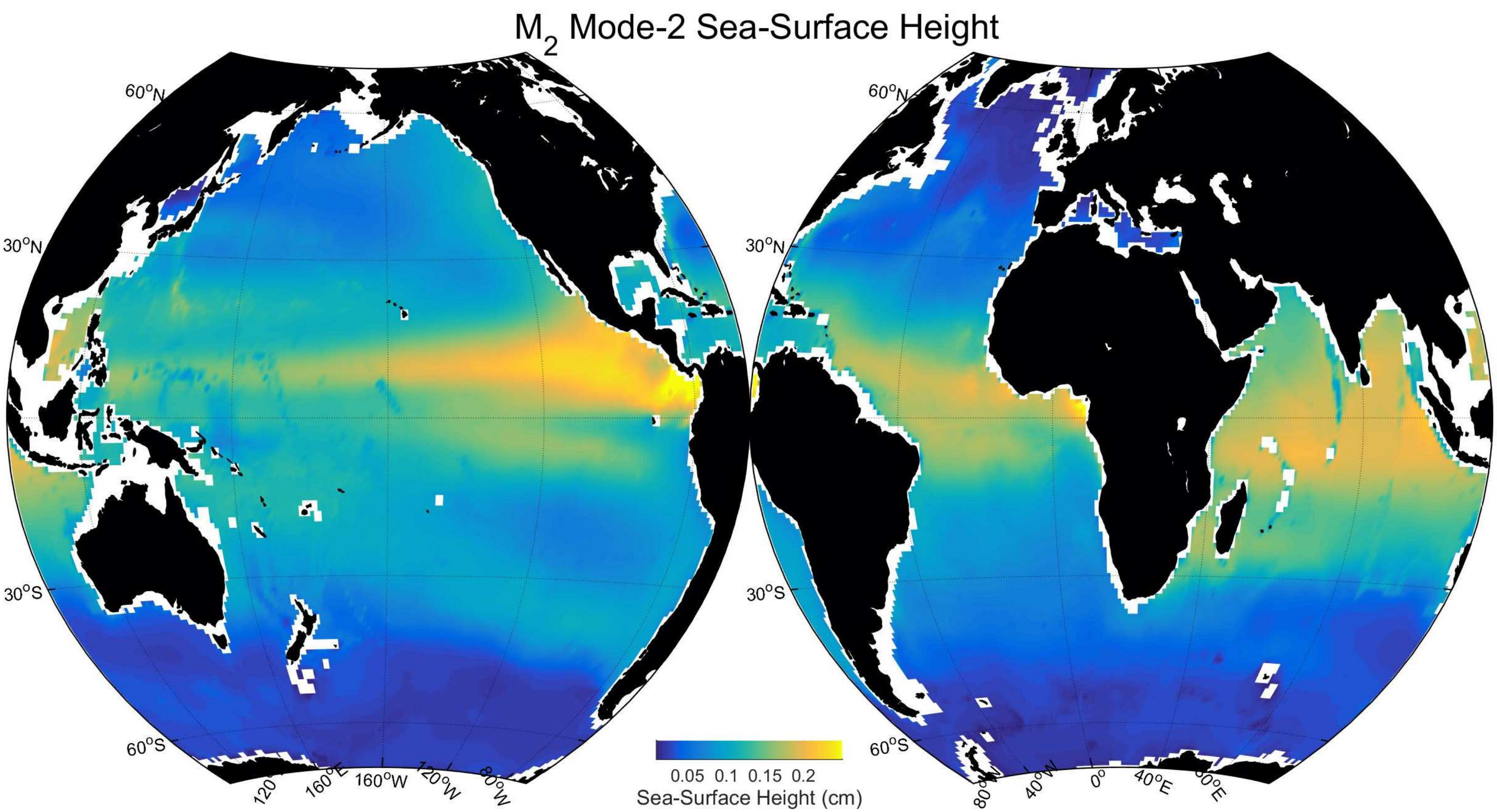

Figure 33. The sea-surface height expression of an M_2, mode-2 internal tide with unit amplitude derived from the 2009 World Ocean Atlas.

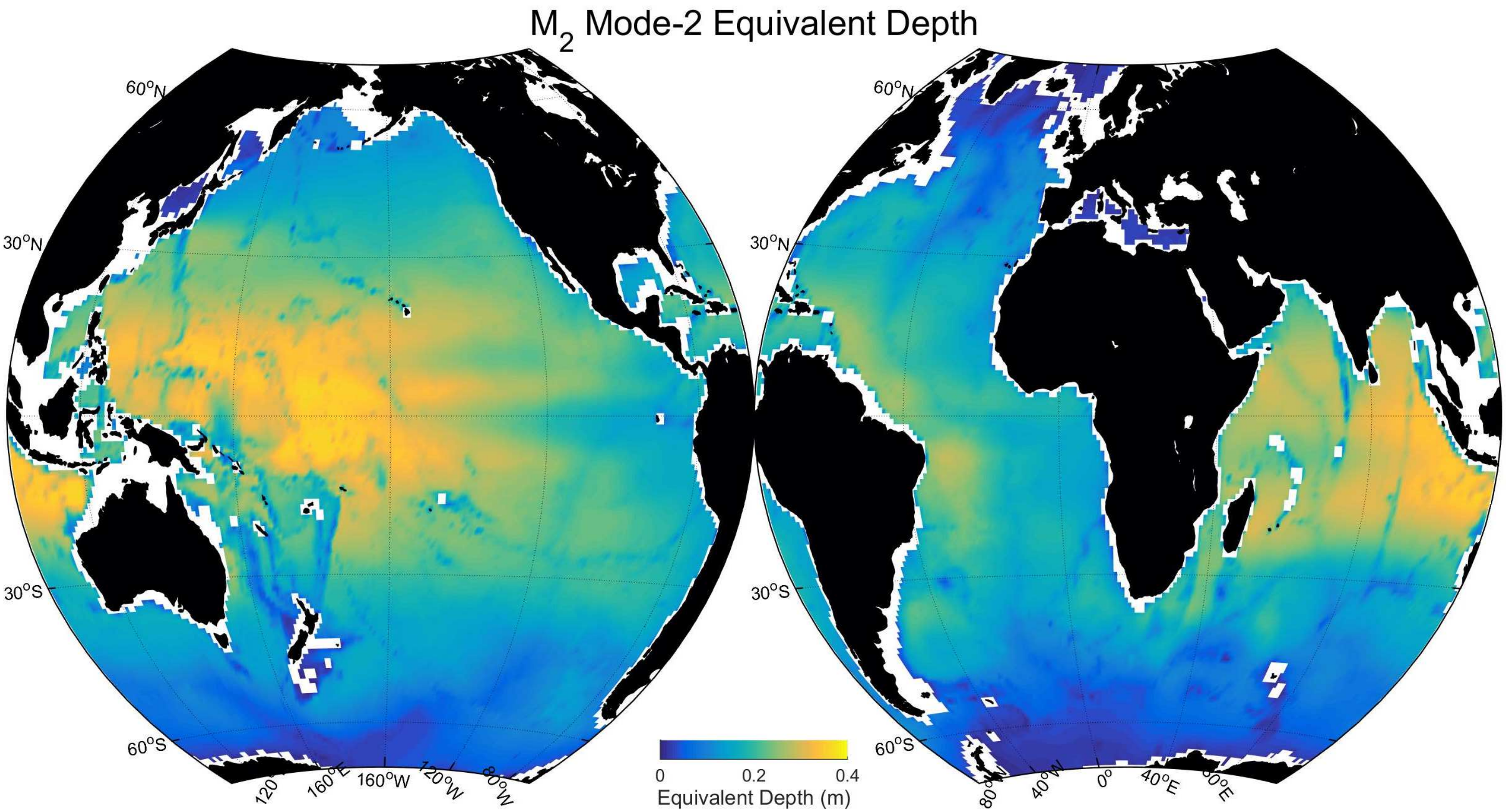

Figure 34. The equivalent depth for the M_2, mode-2 internal tide derived from the 2009 World Ocean Atlas.

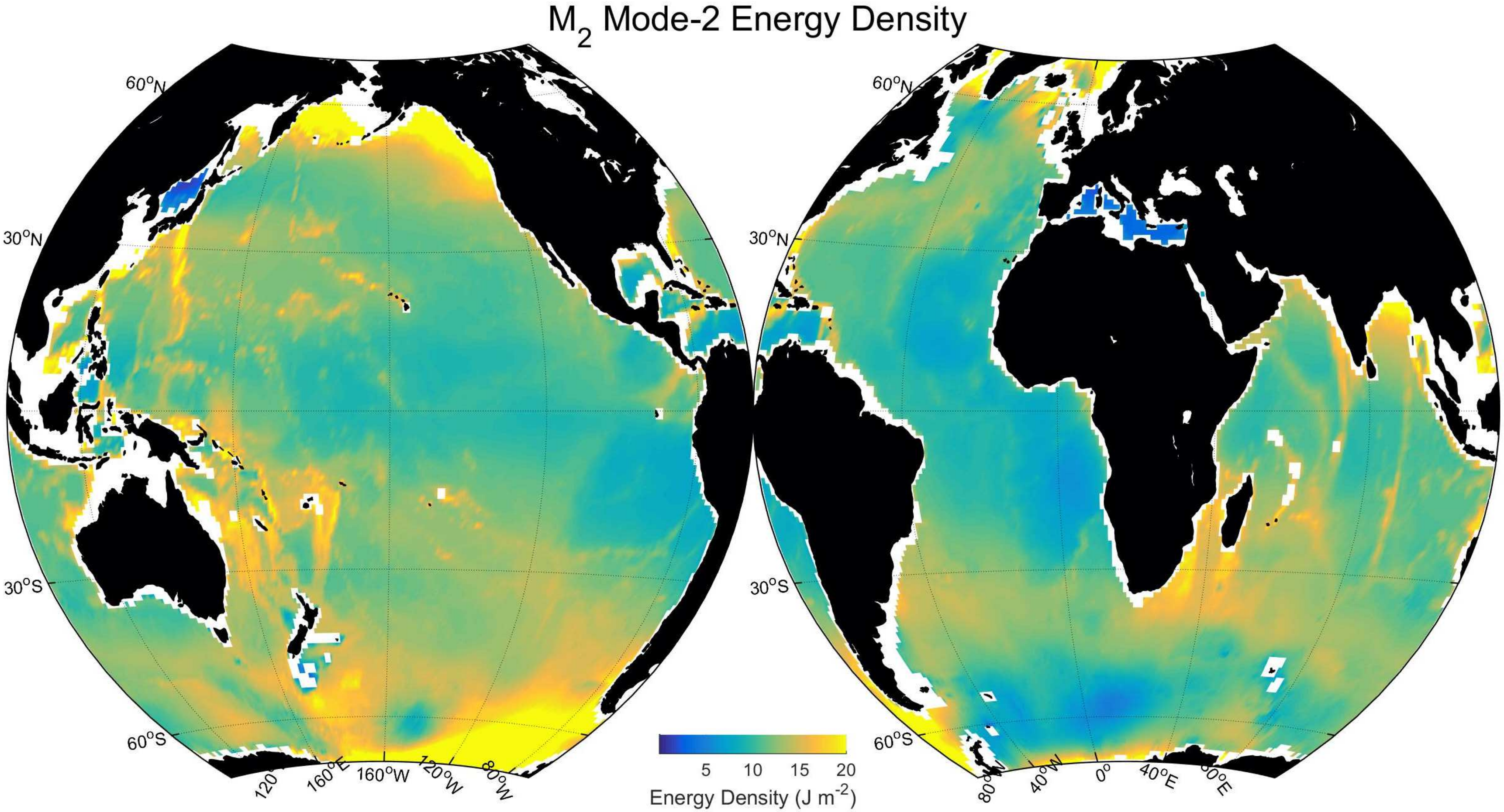

Figure 35. The energy density for an M_2, mode-2 internal tide with unit amplitude derived from the 2009 World Ocean Atlas.

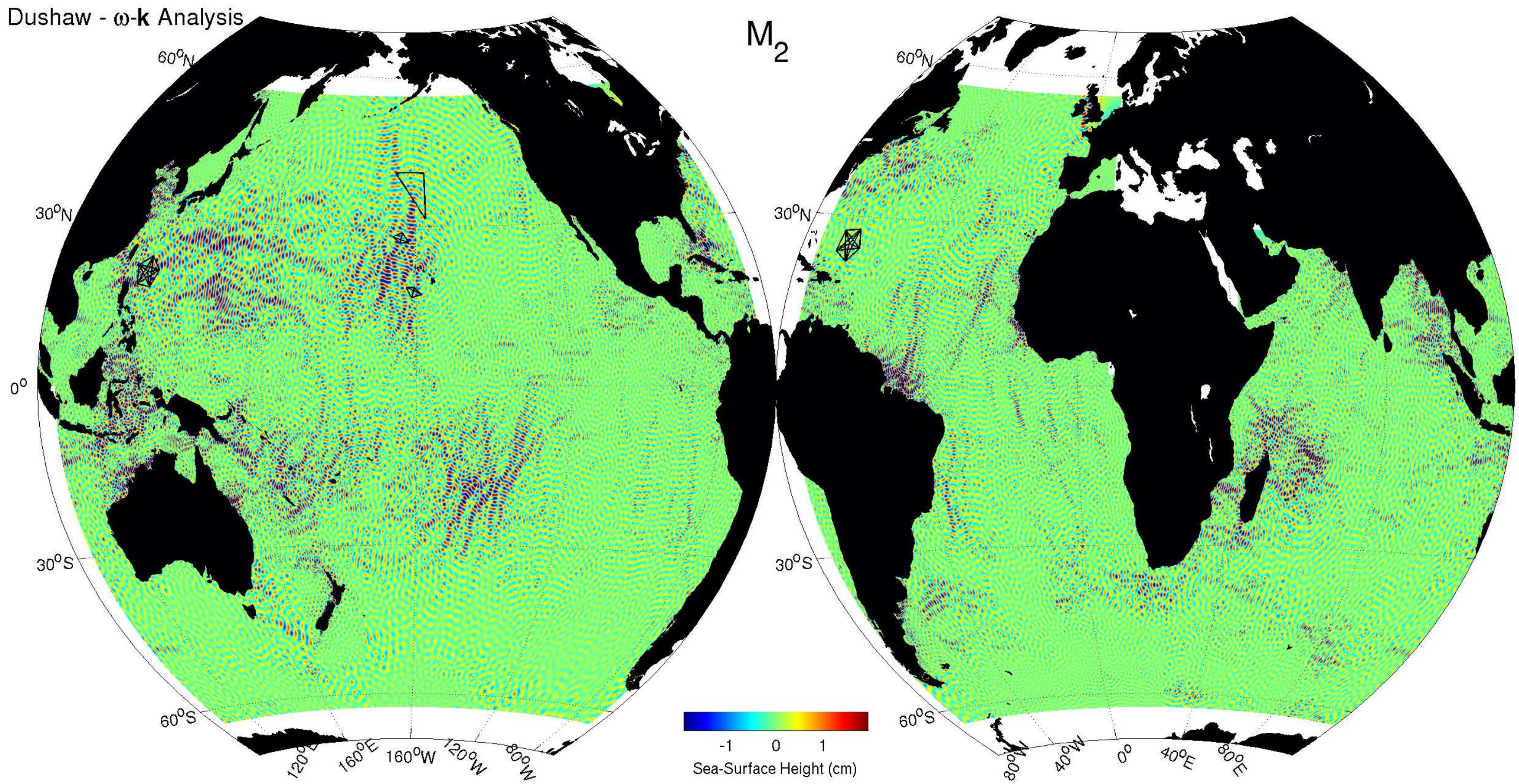

Figure 36. Sea-surface height of mode-1, M_2 internal tide. From west to east tomography arrays are indicated: Philippine Sea, HOME (Hawaii), RTE87 (central North Pacific), AMODE (Sargasso Sea). Each side of the globe spans 190°. Hammer-Aitoff Projections.

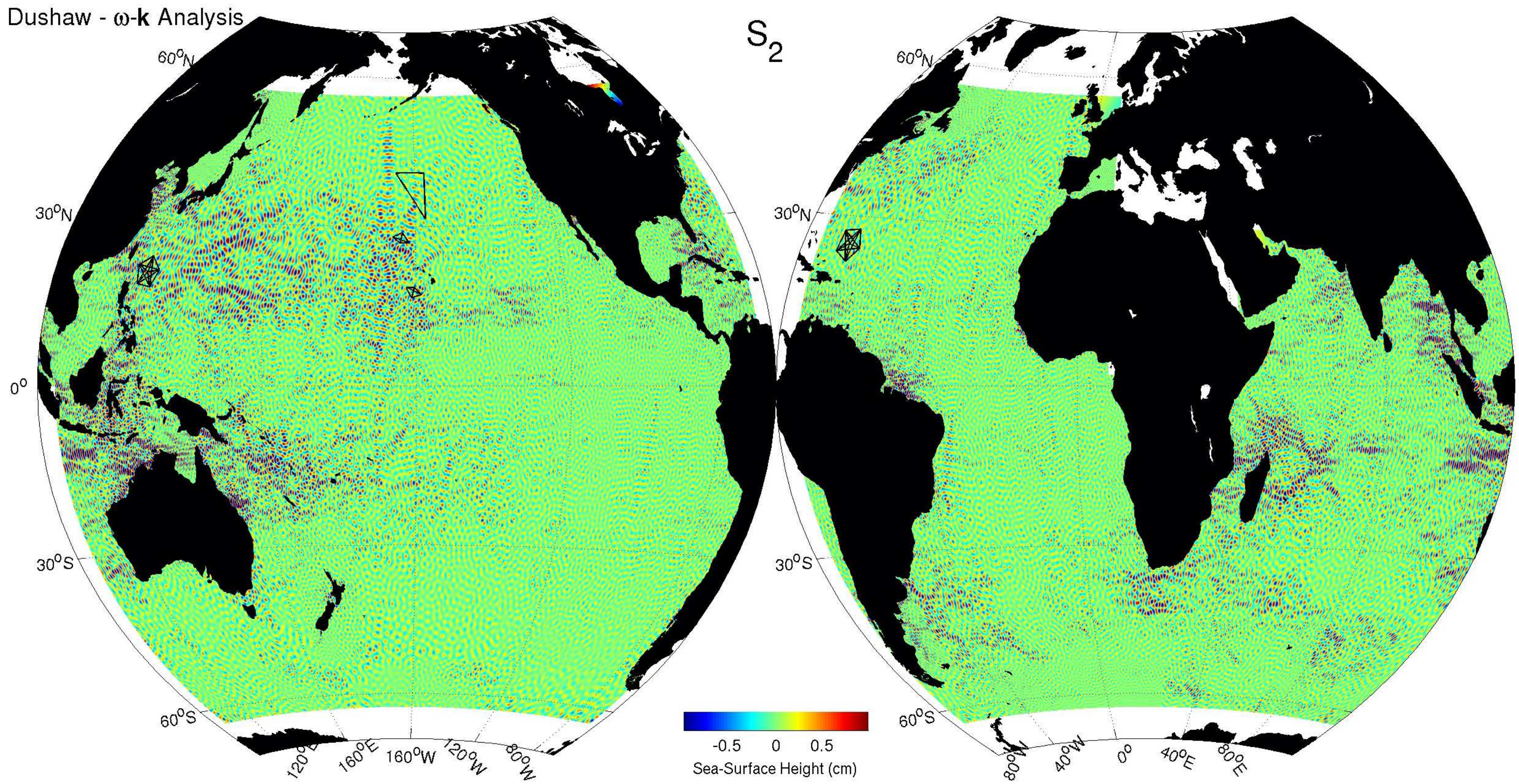

Figure 37. Sea-surface height of mode-1, S_2 internal tide.

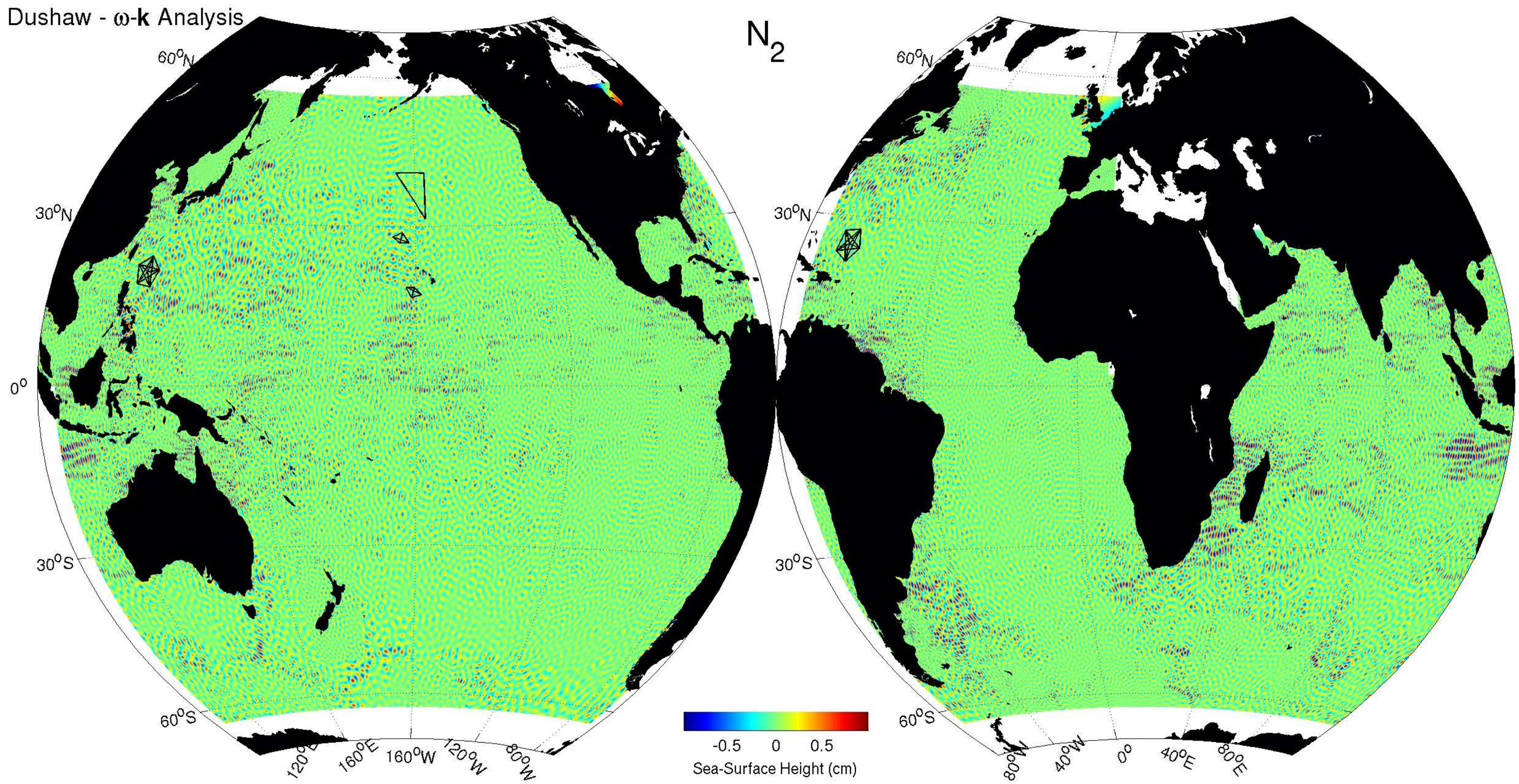

Figure 38. Sea-surface height of mode-1, N_2 internal tide.

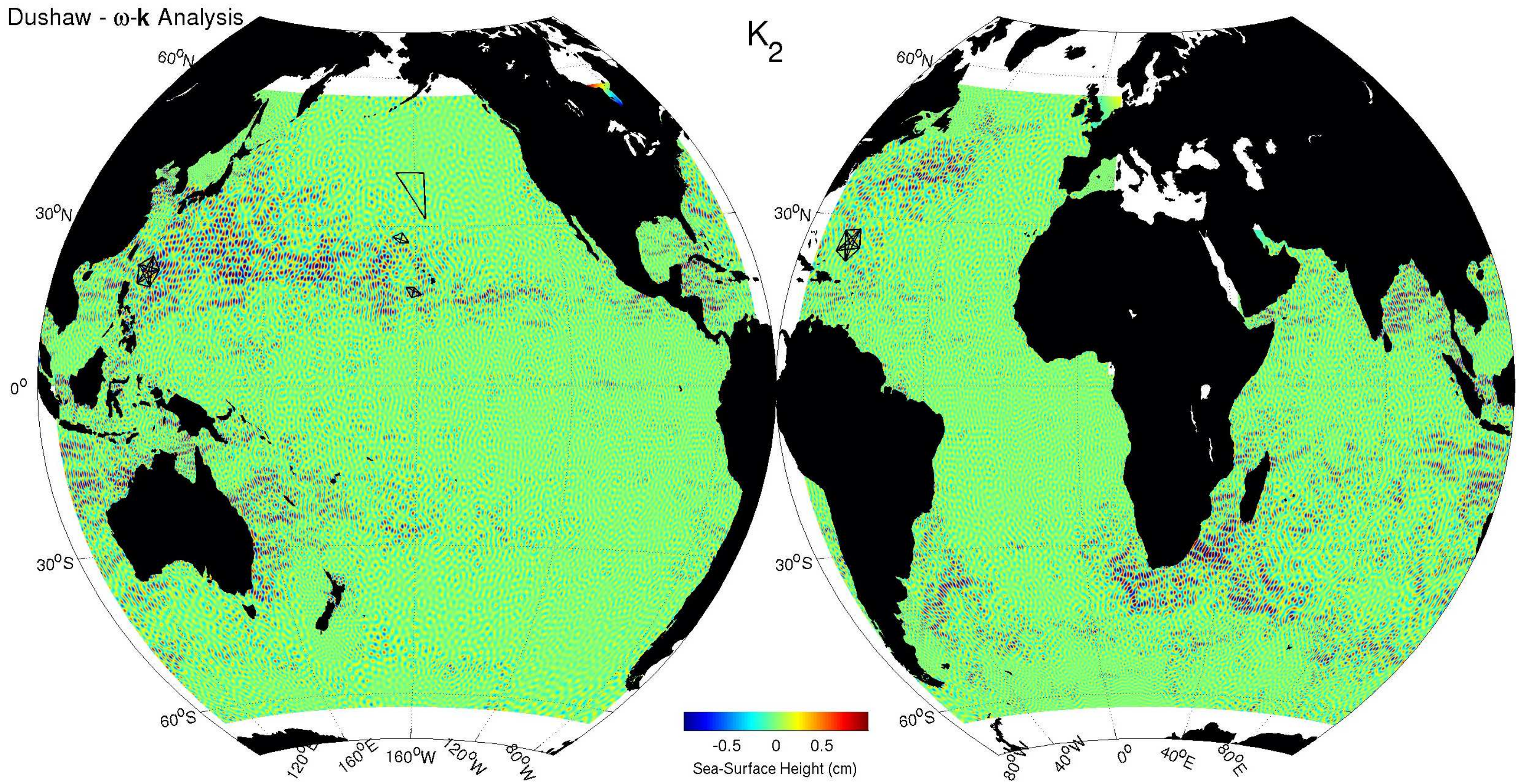

Figure 39. Sea-surface height of mode-1, K_2 internal tide.

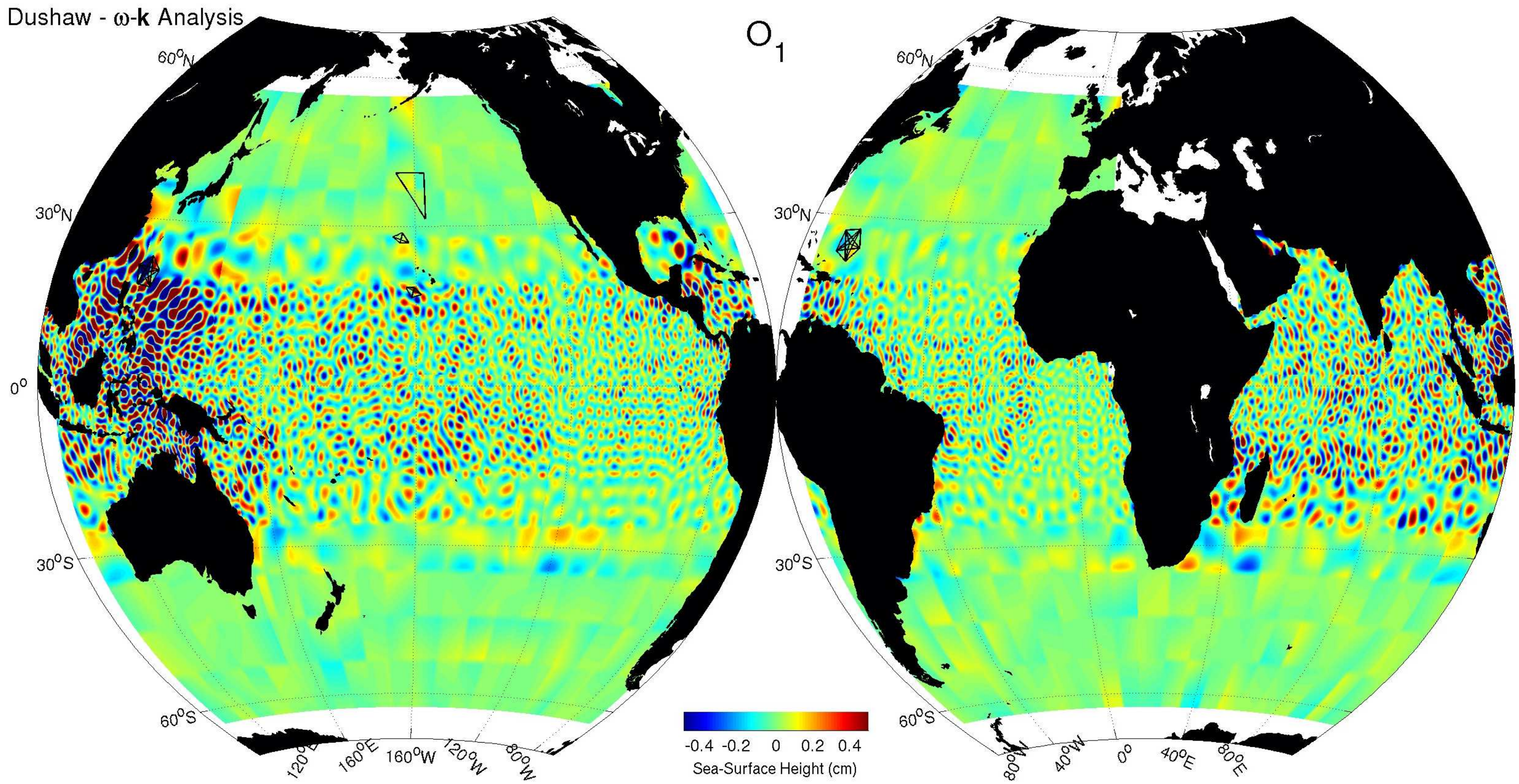

Figure 40. Sea-surface height of mode-1, O_1 internal tide.

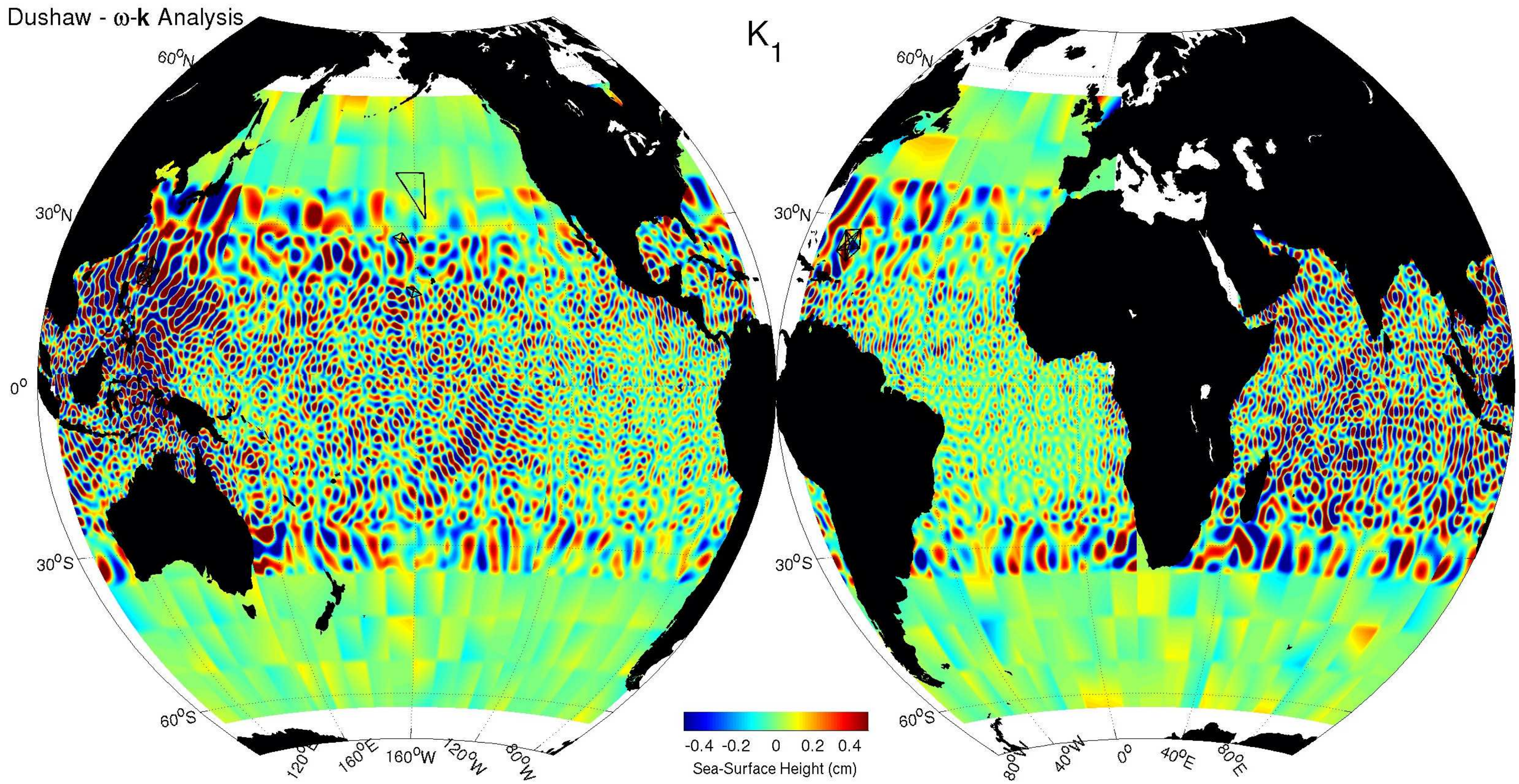

Figure 41. Sea-surface height of mode-1, K_1 internal tide.

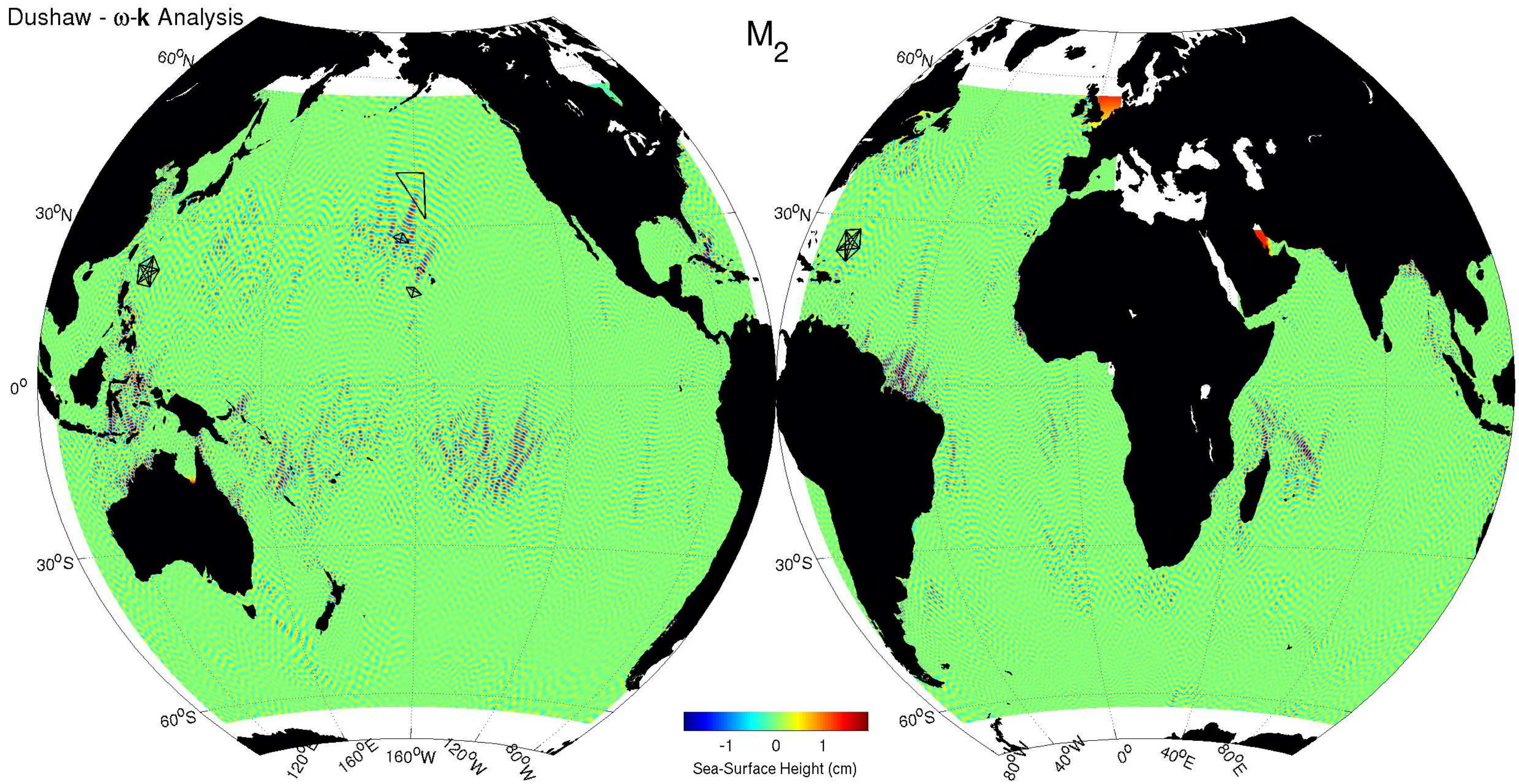

Figure 42. Sea-surface height of mode-1, M_2 internal tide, northward wavenumbers.

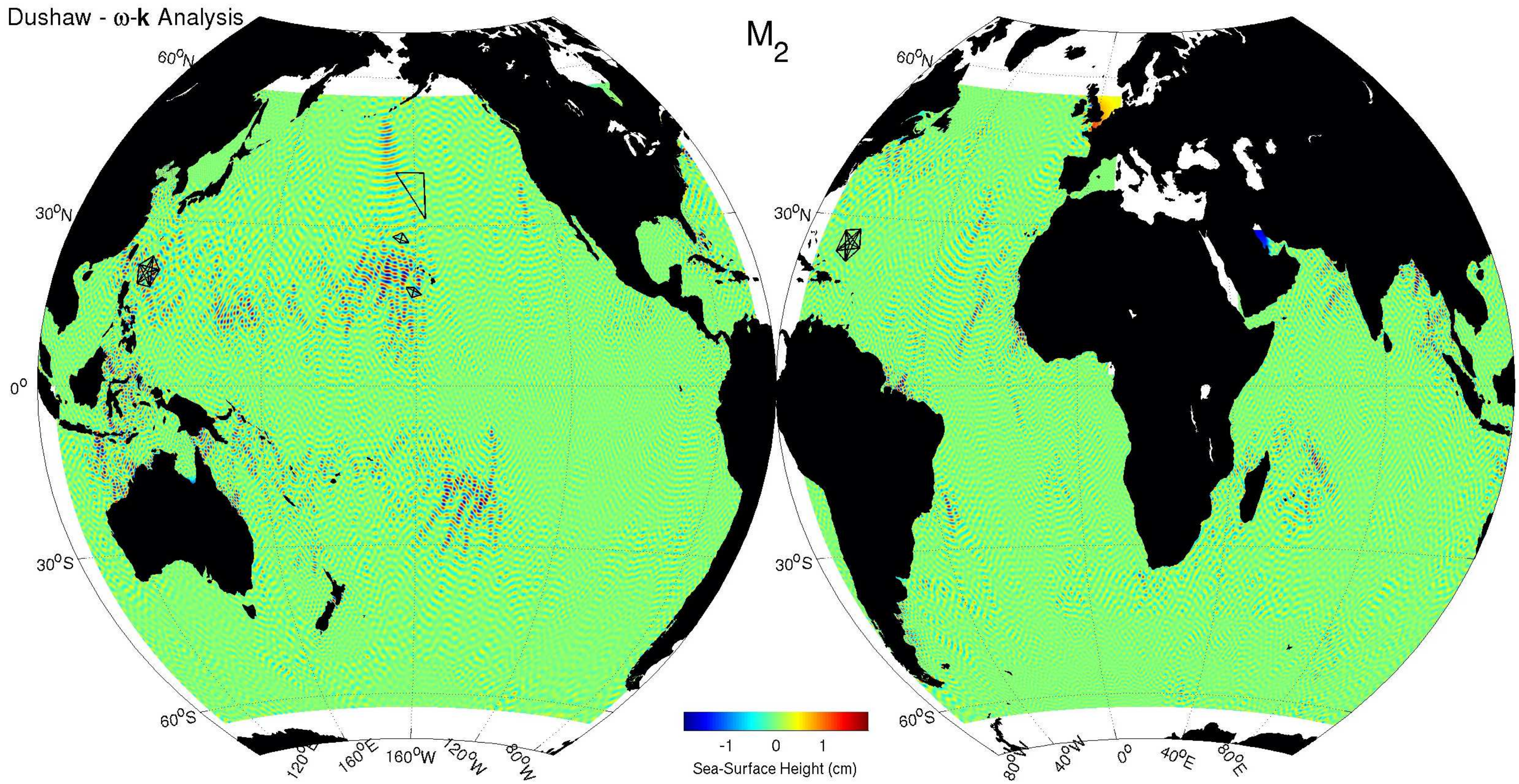

Figure 43. Sea-surface height of mode-1, M_2 internal tide, southward wavenumbers.

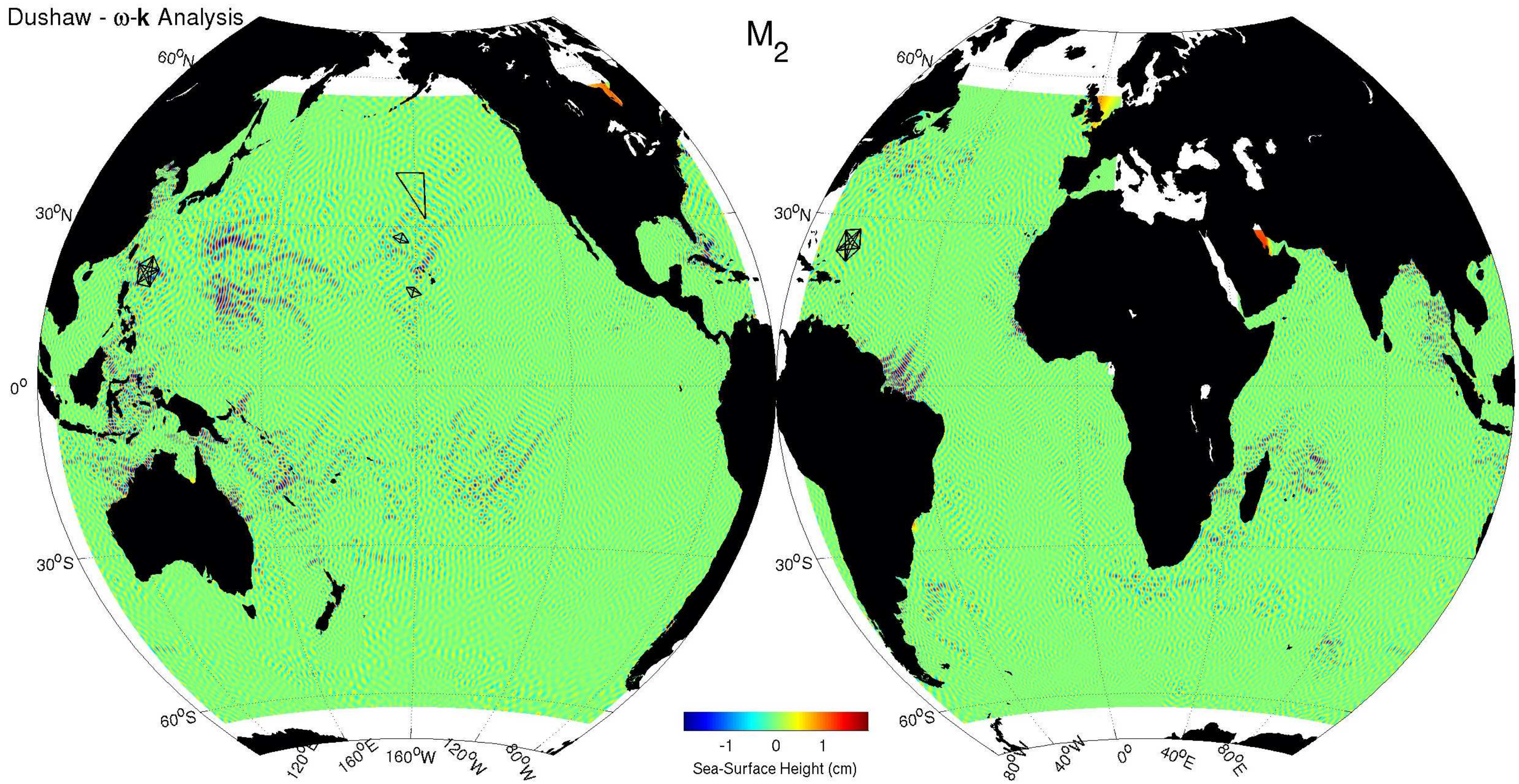

Figure 44. Sea-surface height of mode-1, M_2 internal tide, eastward wavenumbers.

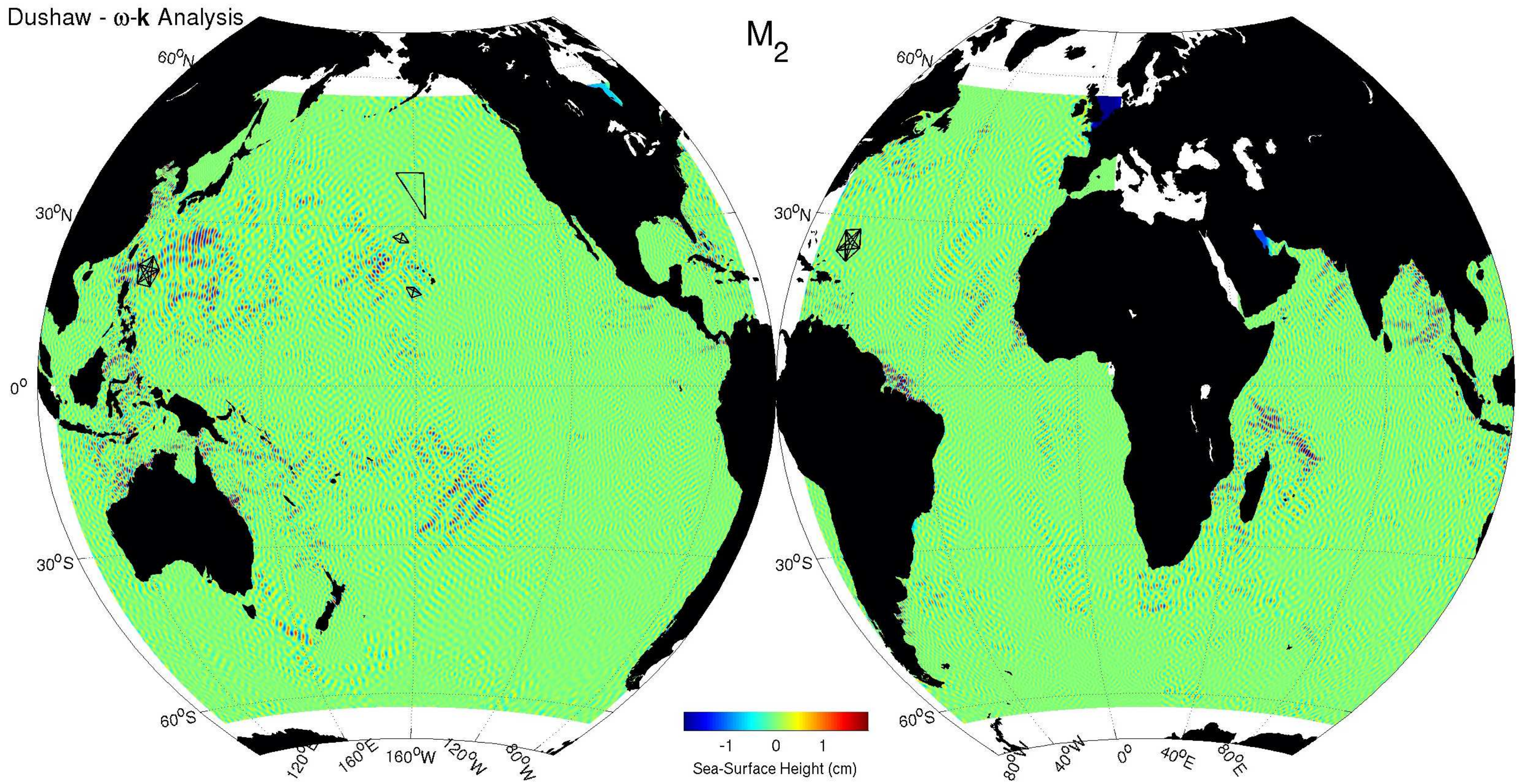

Figure 45. Sea-surface height of mode-1, M_2 internal tide, westward wavenumbers.

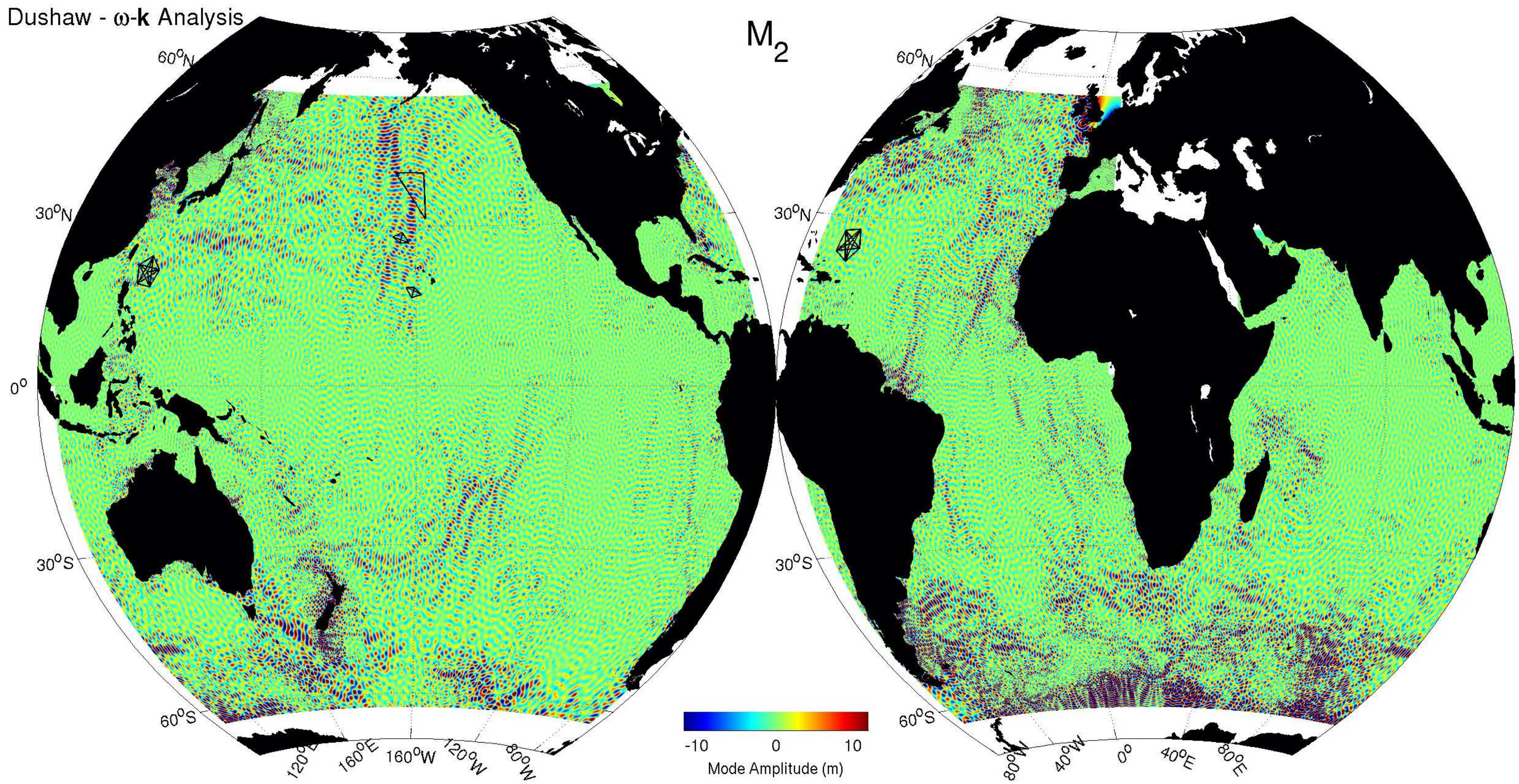

Figure 46. Internal amplitude of mode-1, M_2 internal tide.

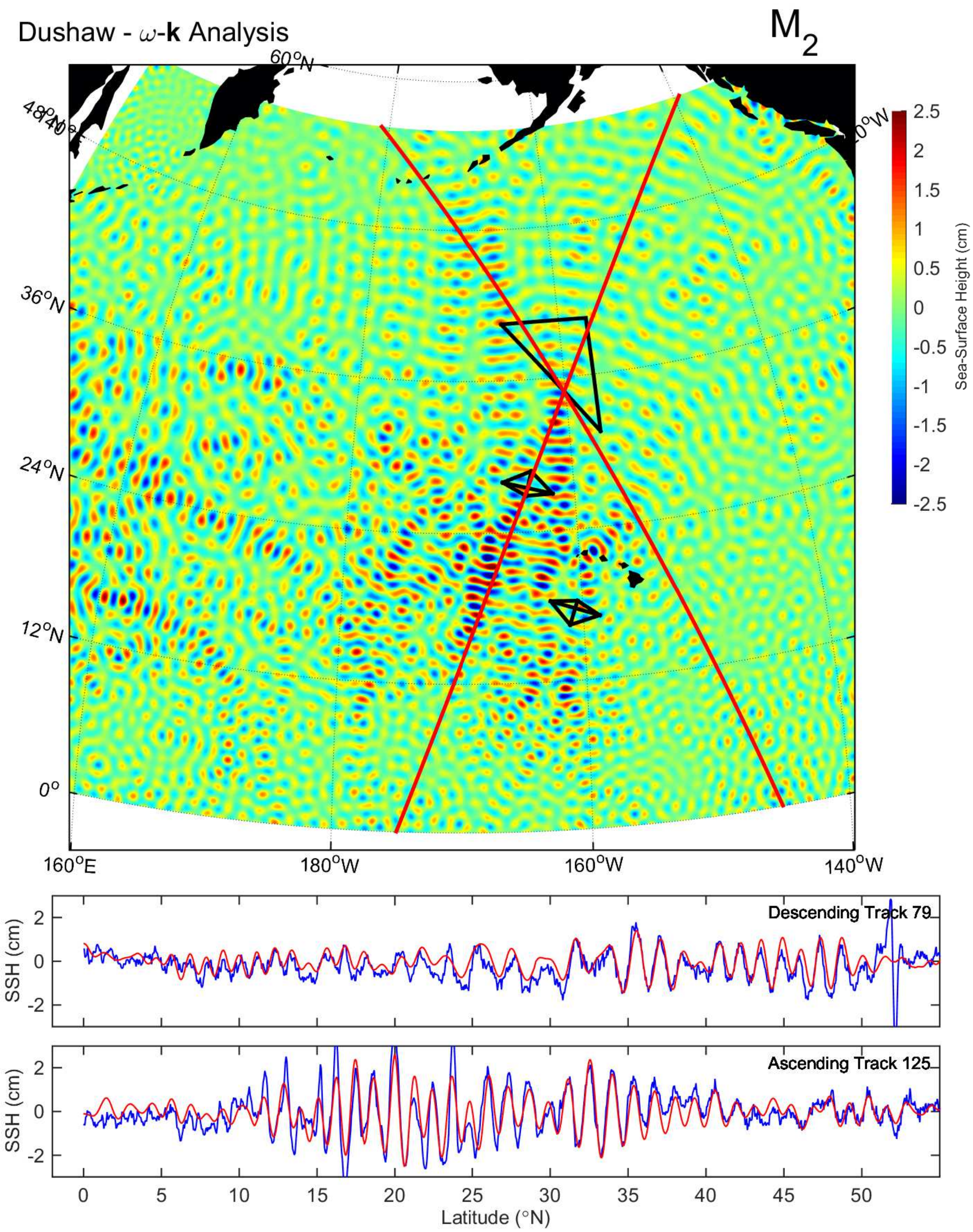

Figure 47. Sea-surface height of the mode-1, M_2 internal tide. The internal tide field is characterized by stable interference patterns extending across the Pacific basin. Ascending track 125 and descending track 79 are indicated by the red lines. Bottom panels compare along track estimates derived by point-wise tidal analyis (blue) and frequency-wavenumber tidal analysis (red). The results from the frequency-wavenumber tidal analysis deviate only slightly from the along-track estimates; they are consistent with the dispersion relation for internal tides. The black triangle and two black diamond shaped arrays denote the RTE87 (1987) and HOME (2001) experiments.

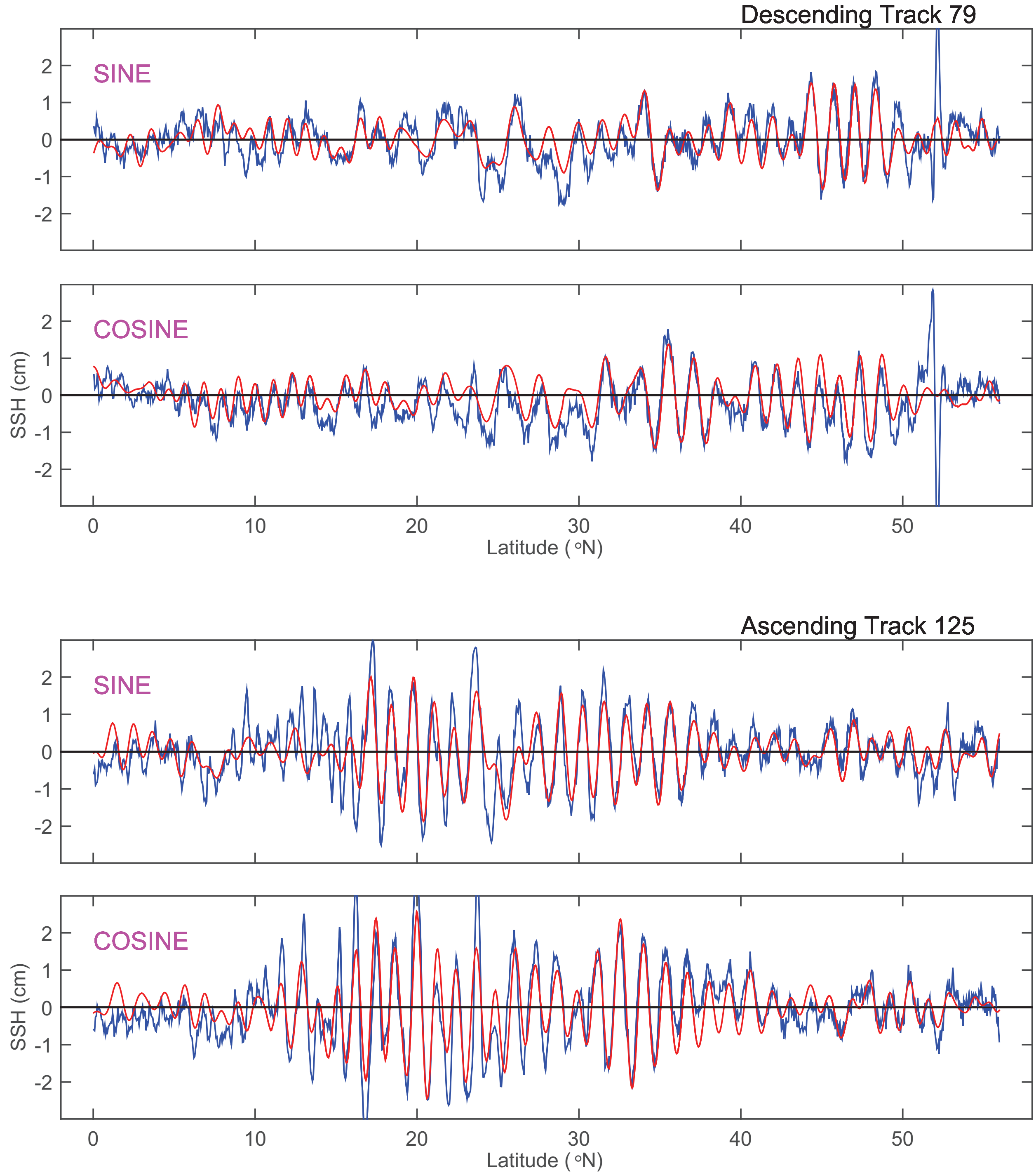

Figure 48. Comparison of along-track and frequency-wavenumber mode-1, M_2 harmonic constants, sine and cosine components, along the two tracks 79 and 125 across the North Pacific, as in Figure 37.

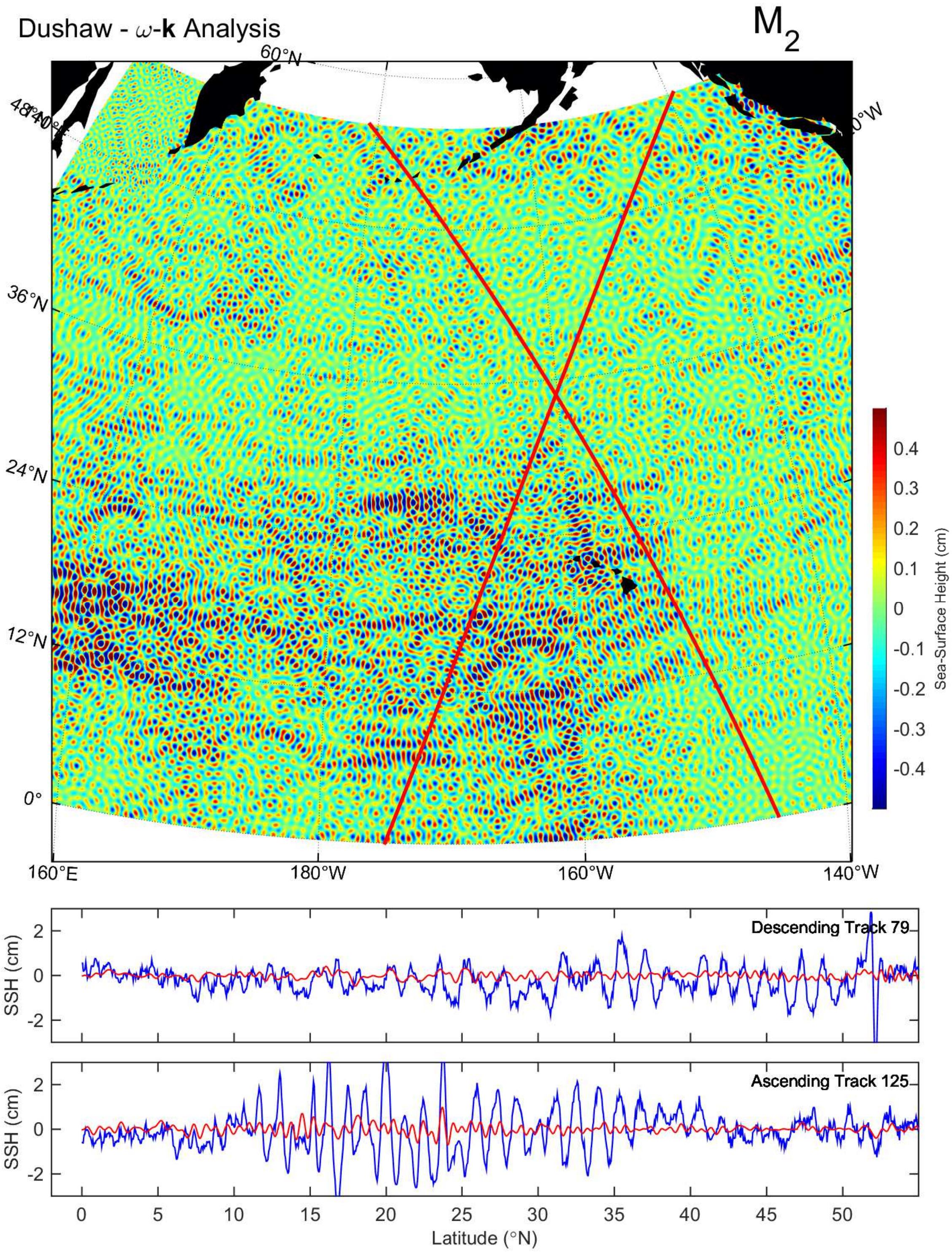

Figure 49. Sea-surface height of the mode-2, M_2 internal tide. As in Figure 47, ascending track 125 and descending track 79 are indicated by the red lines. Bottom panels compare along track estimates derived by point-wise tidal analyis (blue, irrespective of mode number) and frequency-wavenumber tidal analysis (red, mode-2 only). Mode-2 internal tide variations contribute a non-negligible tidal signal in the altimetry data.

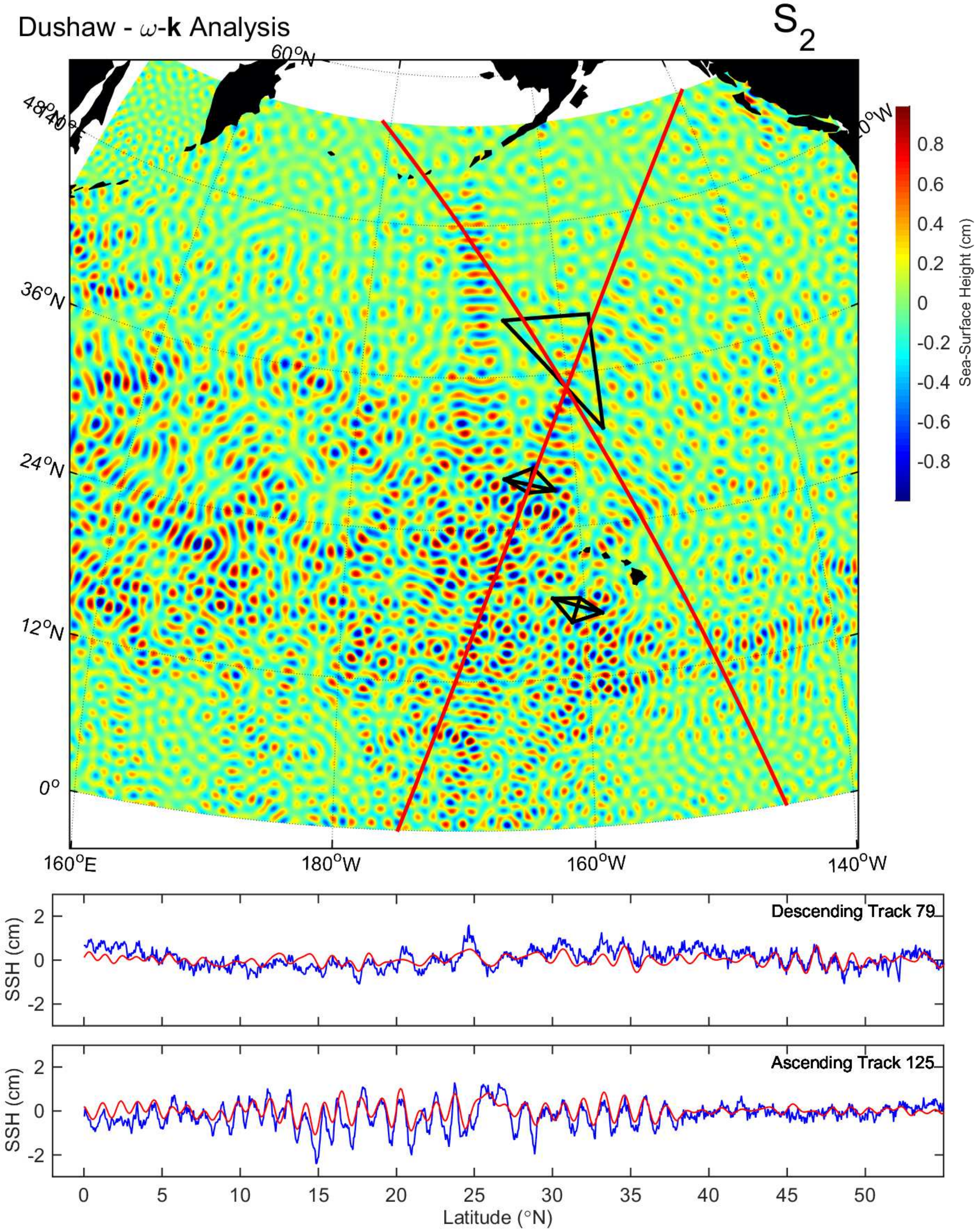

Figure 50. Sea-surface height of the mode-1, S_2 internal tide. Ascending track 125 and descending track 79 are indicated by the red lines. Bottom panels compare along track estimates derived by point-wise tidal analyis (blue) and frequency-wavenumber tidal analysis (red). The S_2 tides are about half the amplitudes of M_2, yet their signals are still apparent in the altimetry data.

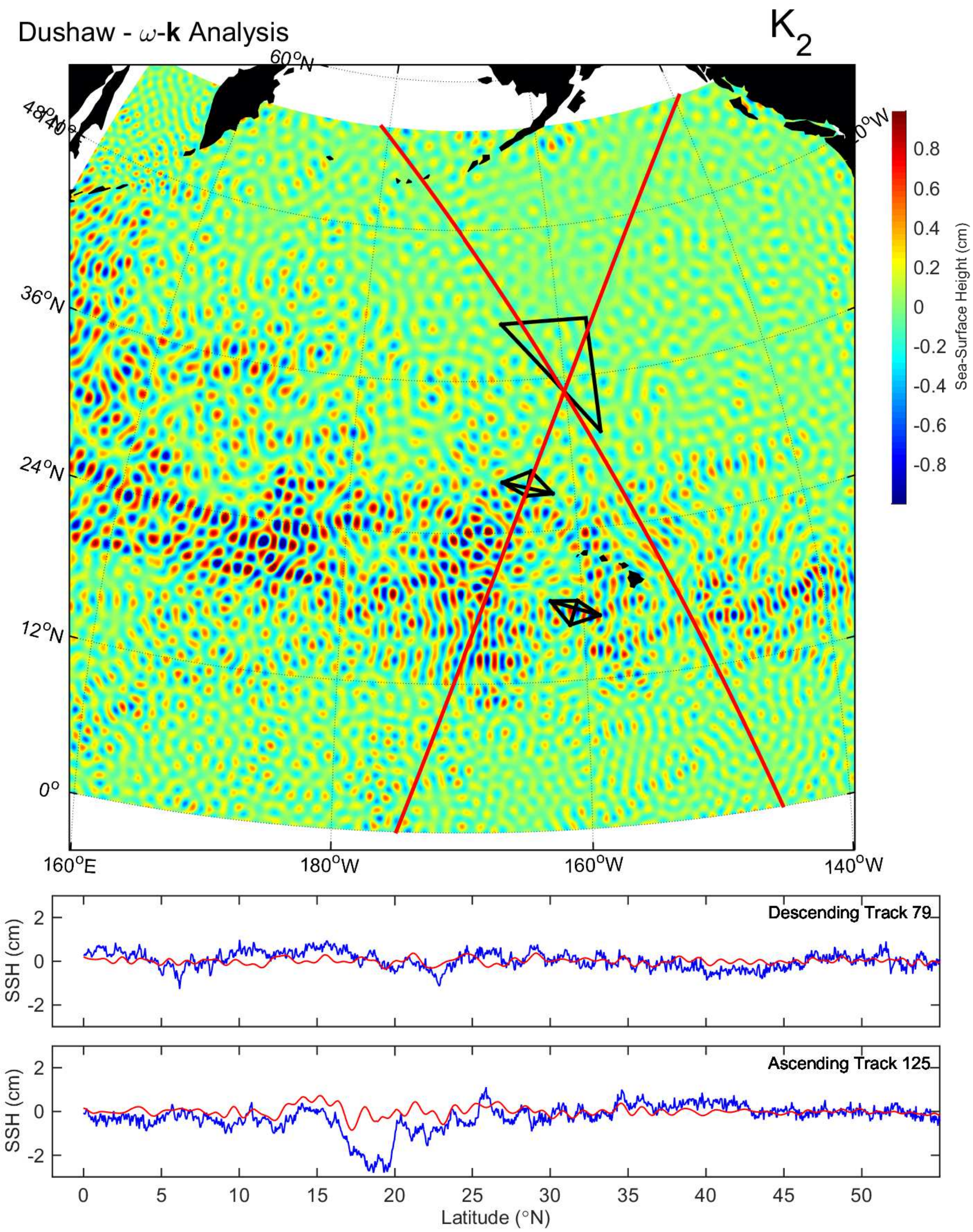

Figure 51. Sea-surface height of the mode-1, K_2 internal tide. Ascending track 125 and descending track 79 are indicated by the red lines. Bottom panels compare along track estimates derived by point-wise tidal analyis (blue) and frequency-wavenumber tidal analysis (red). The K_2 tides do not likely have sufficient signal-to-noise in the altimetry data.

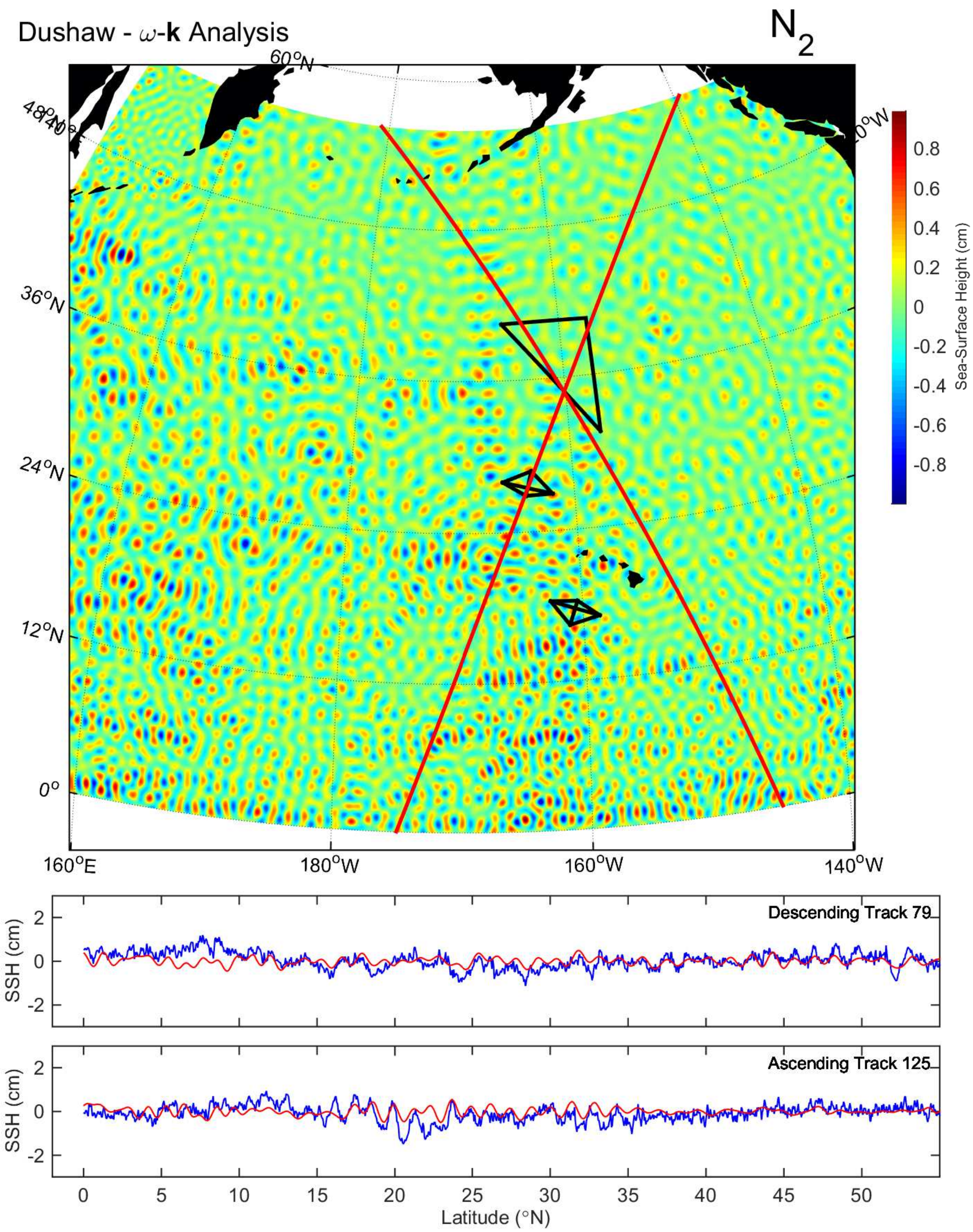

Figure 52. Sea-surface height of the mode-1, N_2 internal tide. Ascending track 125 and descending track 79 are indicated by the red lines. Bottom panels compare along track estimates derived by point-wise tidal analyis (blue) and frequency-wavenumber tidal analysis (red). The N_2 tides do not likely have sufficient signal-to-noise in the altimetry data. Note that the M_2 and N_2 frequencies are similar, yet the N_2 estimates are greatly suppressed relative to M_2. The M_2 internal tide estimates are not likely a result of aliasing of the mesoscale.

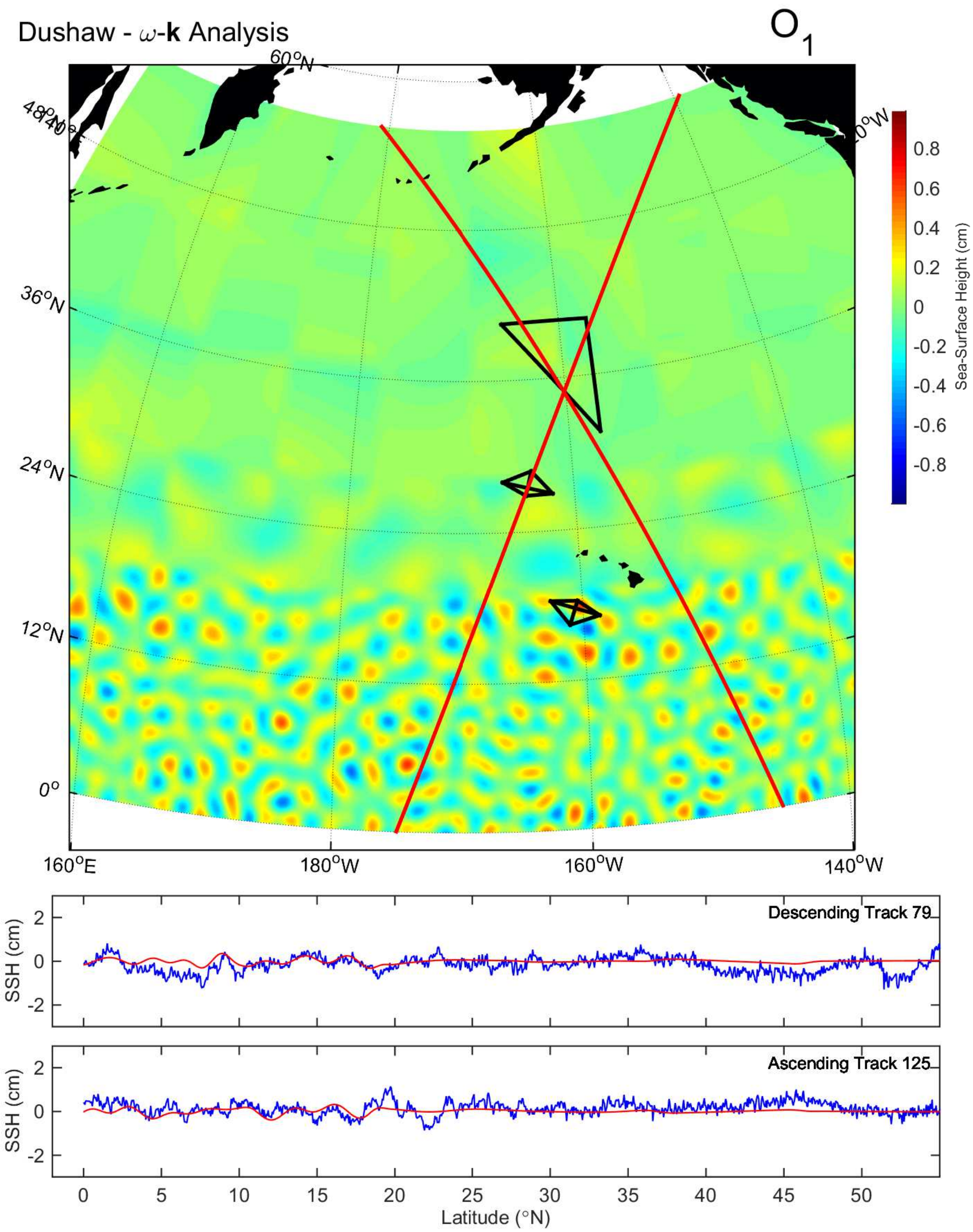

Figure 53. Sea-surface height of the mode-1, O_1 internal tide. Ascending track 125 and descending track 79 are indicated by the red lines. Bottom panels compare along track estimates derived by point-wise tidal analyis (blue) and frequency-wavenumber tidal analysis (red). The O_1 tides do not likely have sufficient signal-to-noise in the altimetry data. Diurnal internal tides cannot freely propagation north of their turning latitude.

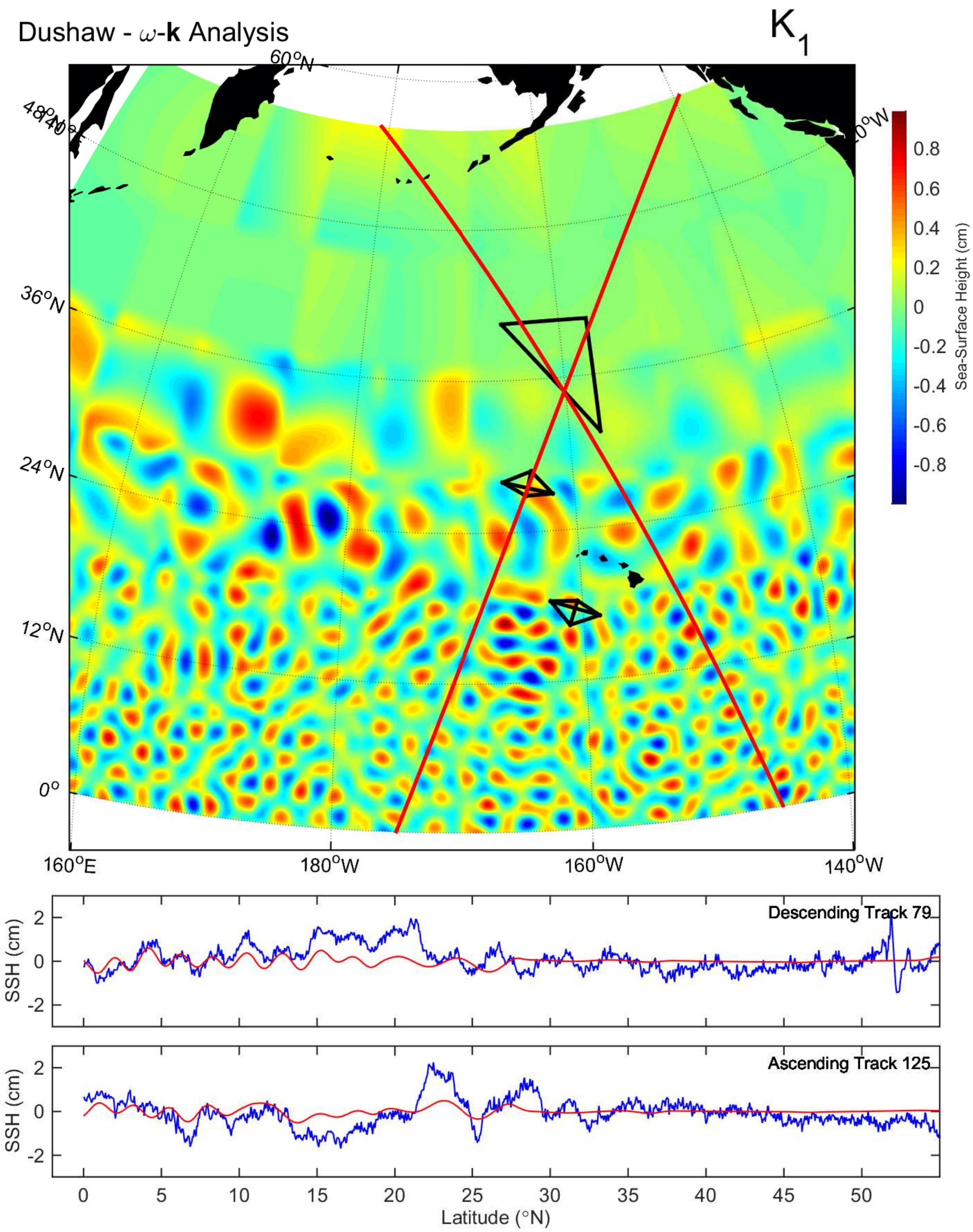

Figure 54. Sea-surface height of the mode-1, K_1 internal tide. Ascending track 125 and descending track 79 are indicated by the red lines. Bottom panels compare along track estimates derived by point-wise tidal analyis (blue) and frequency-wavenumber tidal analysis (red). The K_1 tides do not likely have sufficient signal-to-noise in the altimetry data. Significant tidal variability apparent in the point-wise estimates are not consistent with the dispersion relation for these waves. Predictions from the frequency-wavenumber tidal analysis agree with in situ observations by tomography. Diurnal internal tides cannot freely propagation north of their turning latitude.

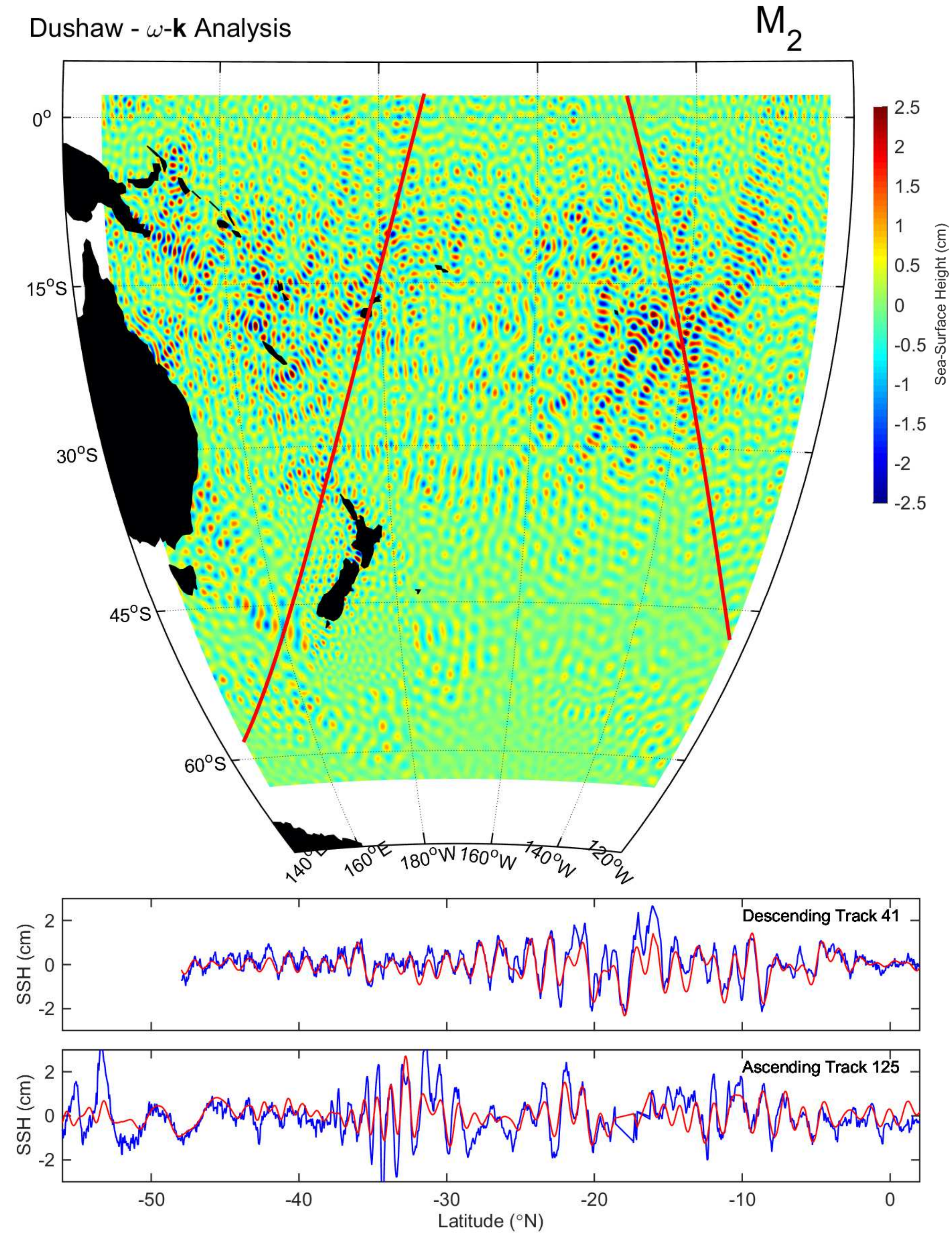

Figure 55. Sea-surface height of the mode-1, M_2 internal tide. The internal tide field is characterized by stable interference patterns extending across the South Pacific basin. Ascending track 125 and descending track 41 are indicated by the red lines. Bottom panels compare along track estimates derived by point-wise tidal analyis (blue) and frequency-wavenumber tidal analysis (red).

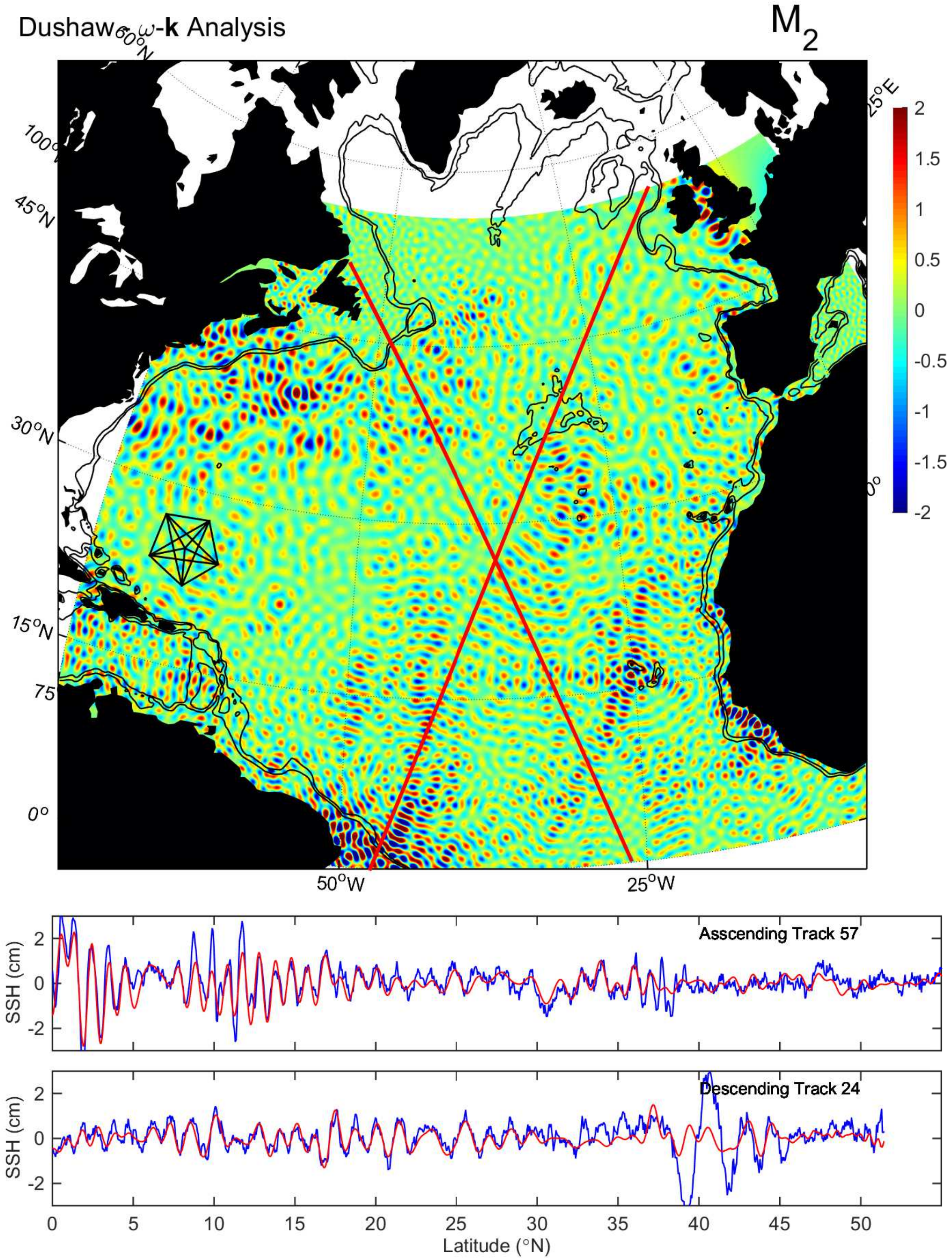

Figure 56. Sea-surface height of the mode-1, M_2 internal tide. The internal tide field is characterized by stable interference patterns extending across the North Atlantic basin. Ascending track 125 and descending track 41 are indicated by the red lines. Bottom panels compare along track estimates derived by point-wise tidal analyis (blue) and frequency-wavenumber tidal analysis (red). The black pentagon north of Puerto Rico denotes the AMODE (1991) experiment.

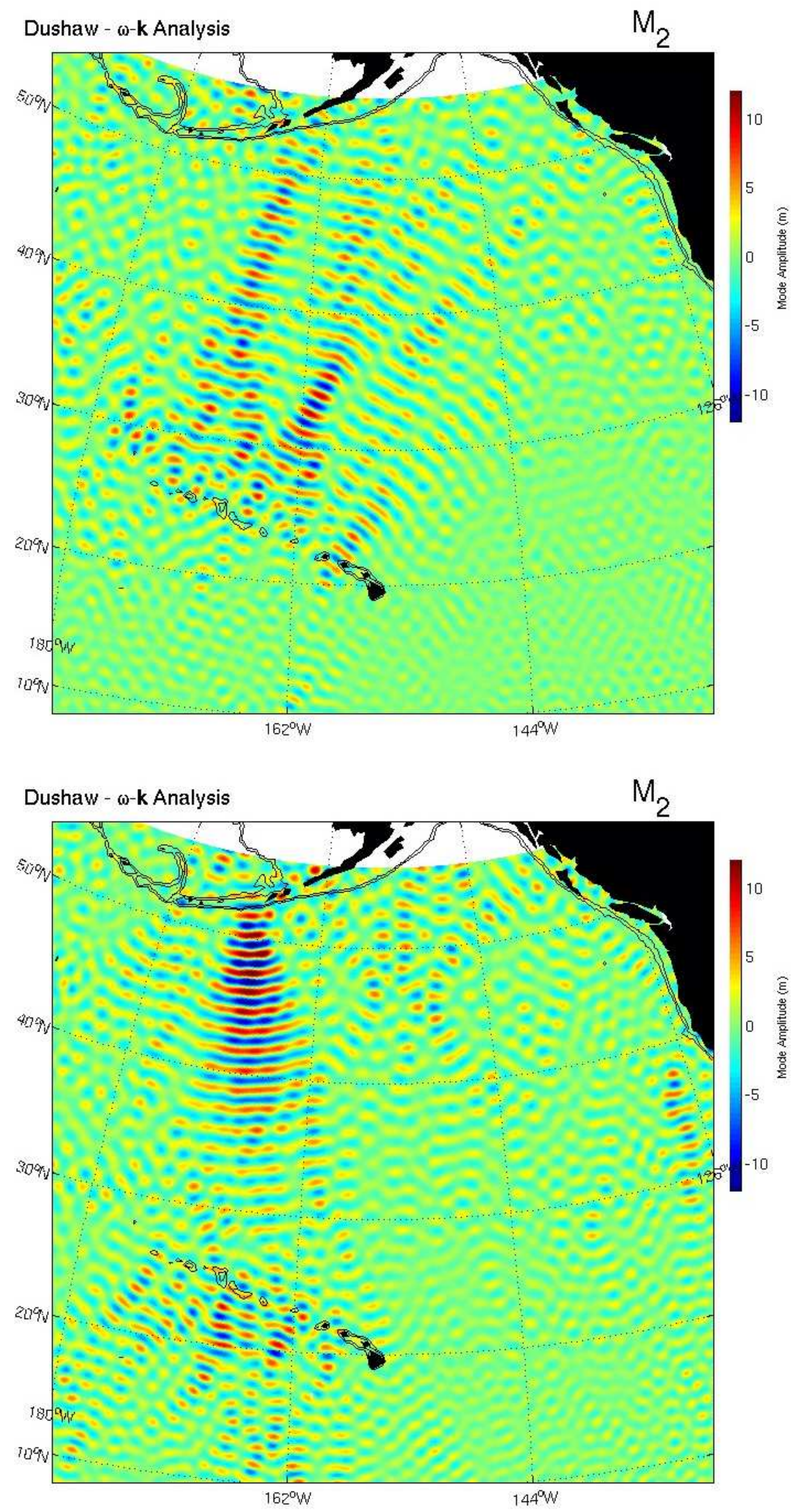

Figure 57. Amplitude of the estimated mode-1, M_2 internal tides of the North Pacific. Top panel: Northward propagating wavenumbers. Bottom panel: Southward propagating wavenumbers. The estimated interference patterns can be decomposed into their underlying wavenumbers, revealing regular wave trains that extend across the Pacific basin. "Beams" extending across the basin are evident, which are a product of extraordinary coherence.

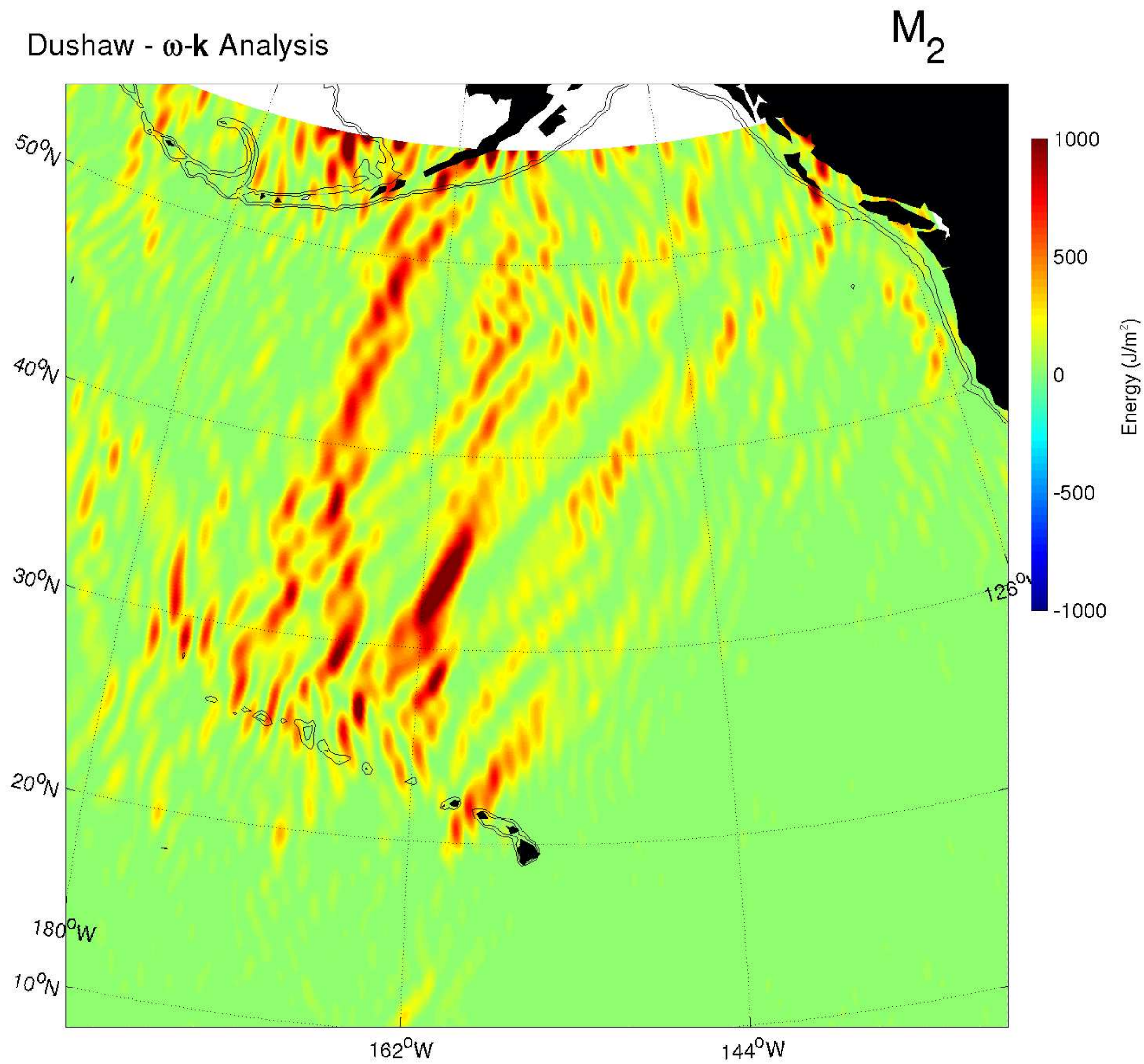

Figure 58. Energy density of the estimated mode-1, M_2 internal tides of the North Pacific. Only northward propagating wavenumbers were used for this computation, hence this energy originates primarily from the Hawaiian Ridge. Allowing for the effects of cylindrical spreading of the wavetrain, little decrease in energy density is evident, indicating little loss of coherence of the northward propagating wavetrain.

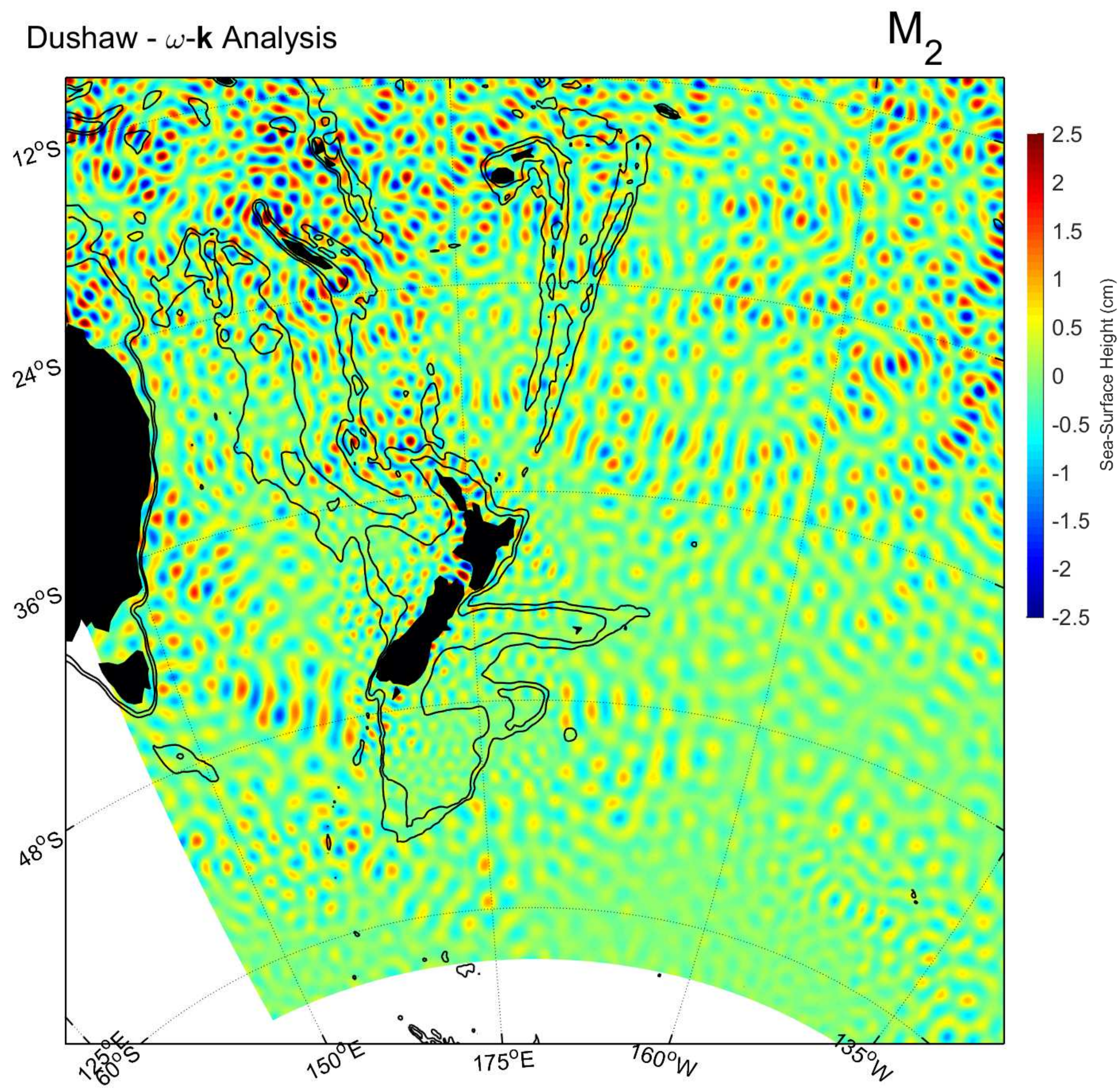

Figure 59. Sea-surface height for the estimated mode-1, M_2 internal tides around New Zealand. Computed with all wavenumbers, the internal tide field is a confused interference patterns with no apparent distinct wavetrains.

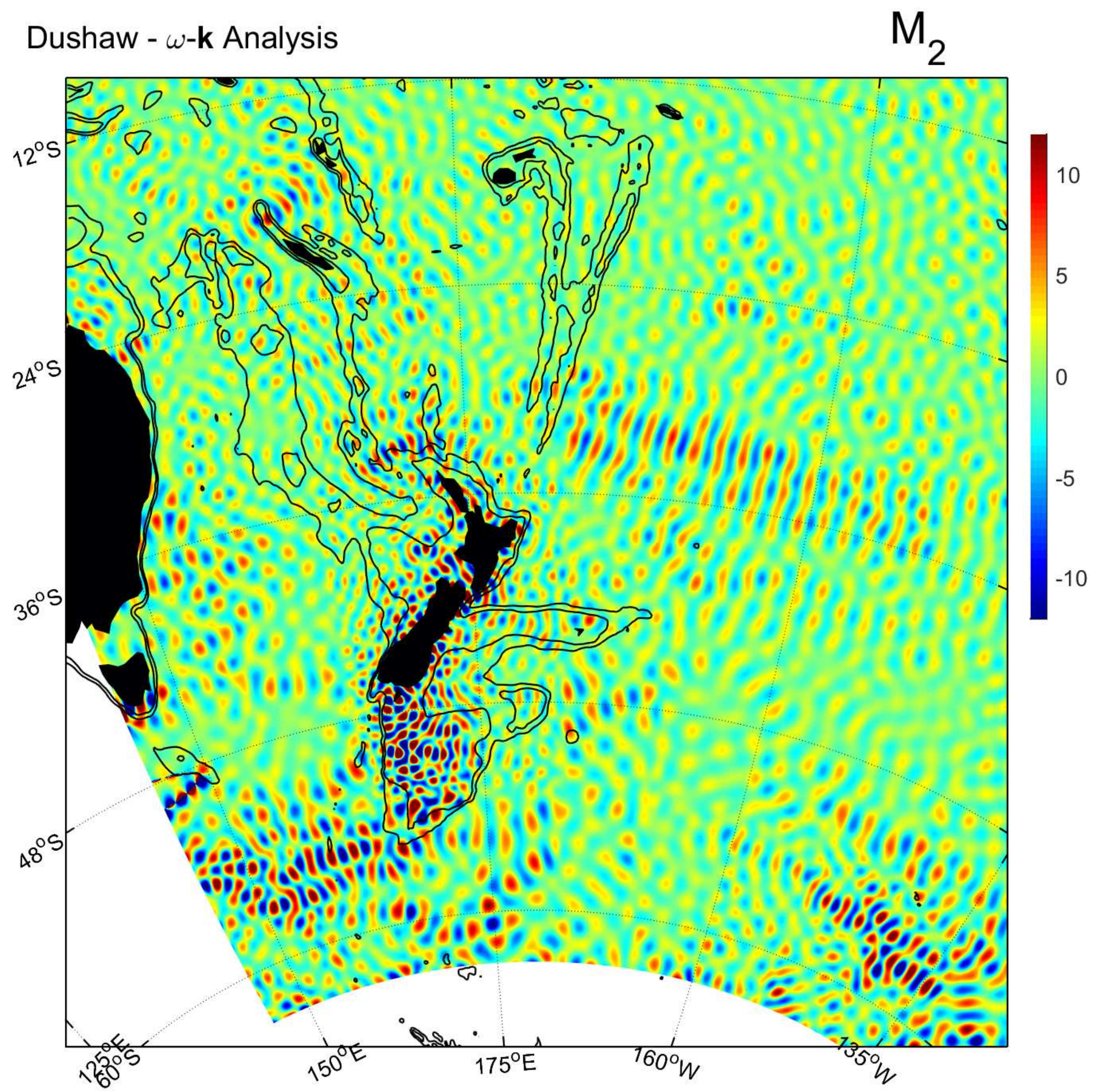

Figure 60. Mode amplitude for the estimated mode-1, M_2 internal tides around New Zealand. In this case, the field was computed using only eastward wavenumbers, which reveals the clear wavetrain emanating from the Kermadec Ridge.

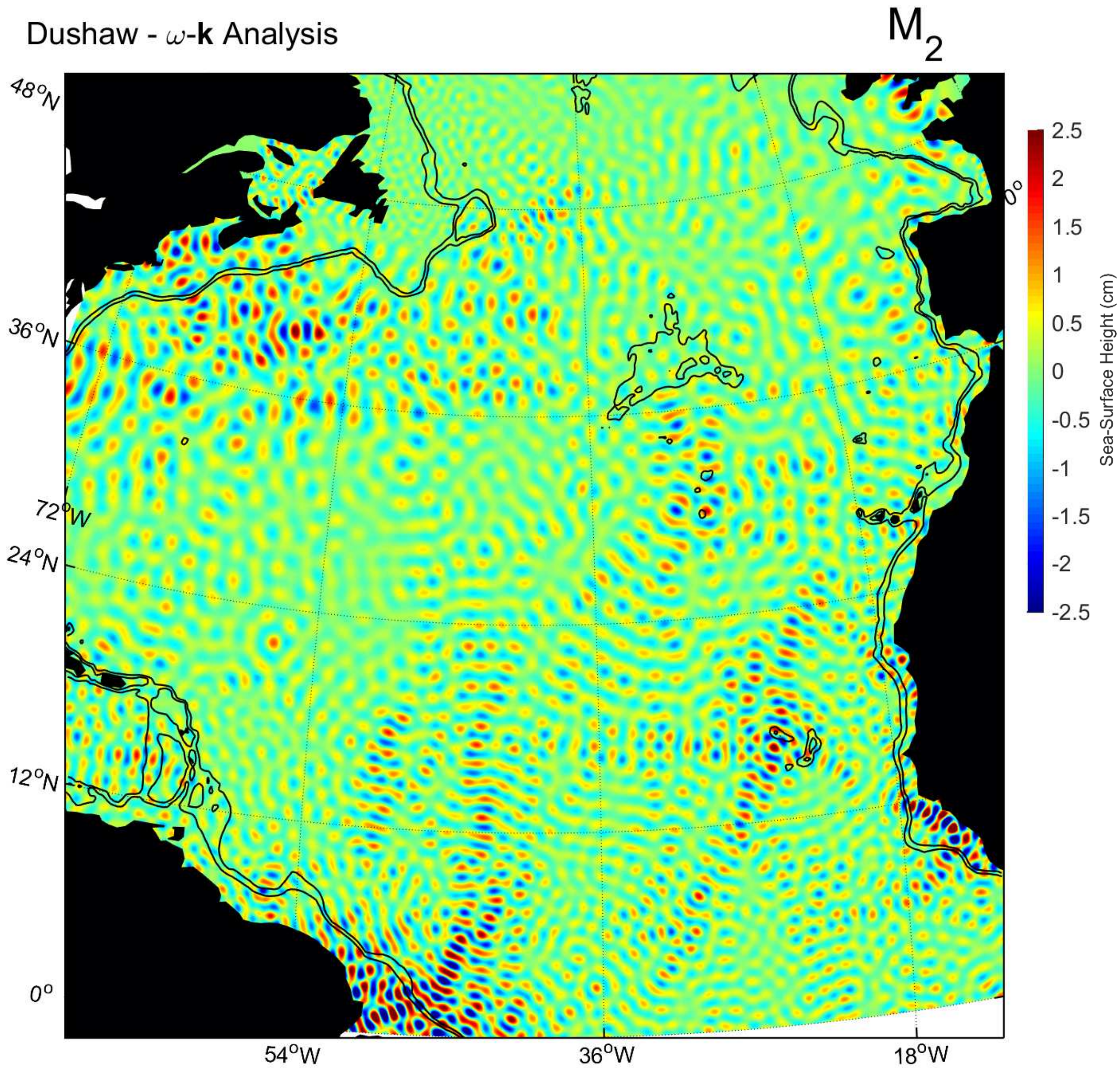

Figure 61. Sea-surface height for the estimated mode-1, M_2 internal tides in the central North Atlantic. Computed with all wavenumbers, the internal tide field is a confused interference patterns with no apparent distinct wavetrains.

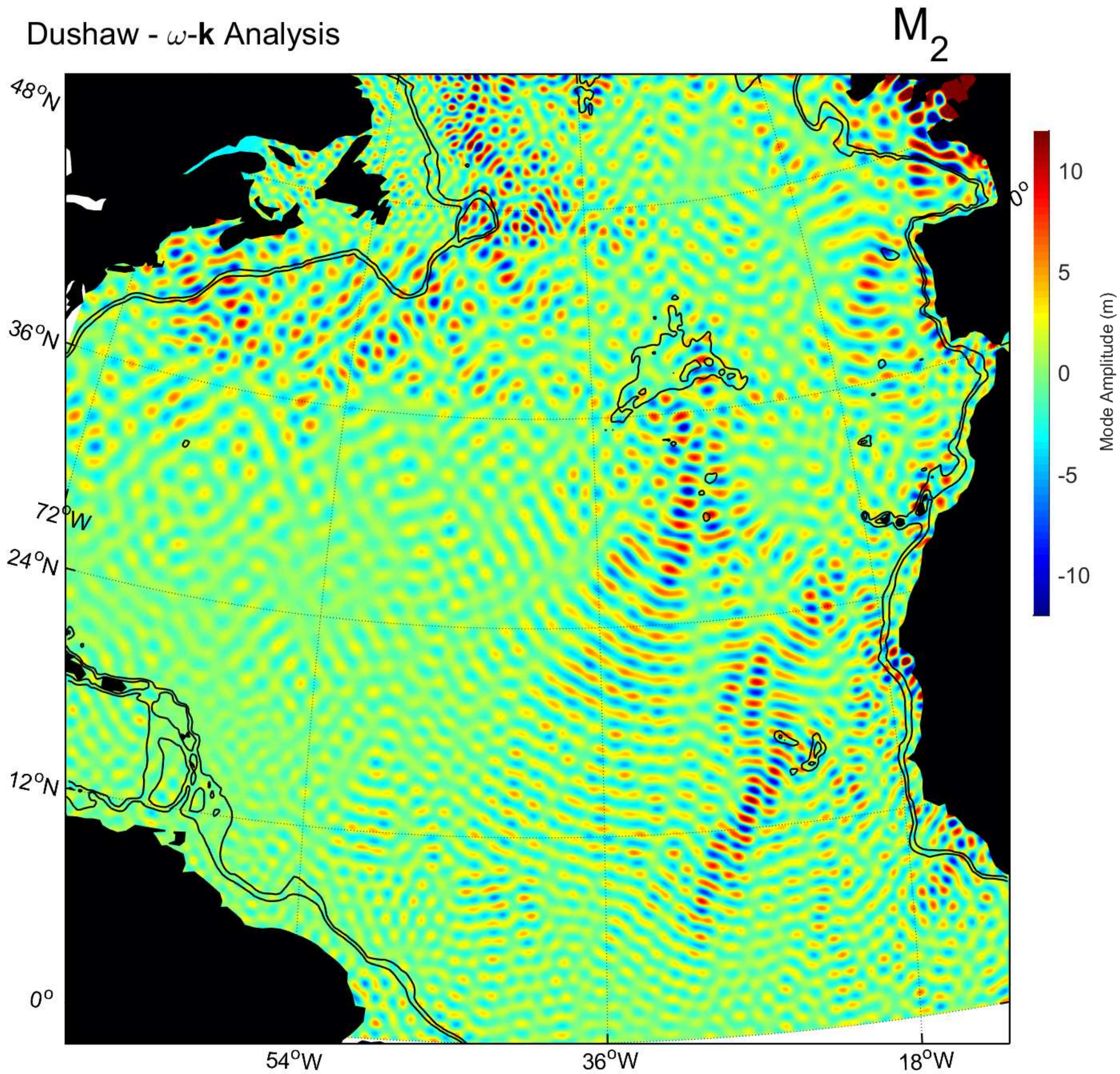

Figure 62. Mode amplitude for the estimated mode-1, M_2 internal tides in the central North Atlantic. In this case, the field was computed using only southward wavenumbers, which reveals the clear wavetrain emanating from the Azores.

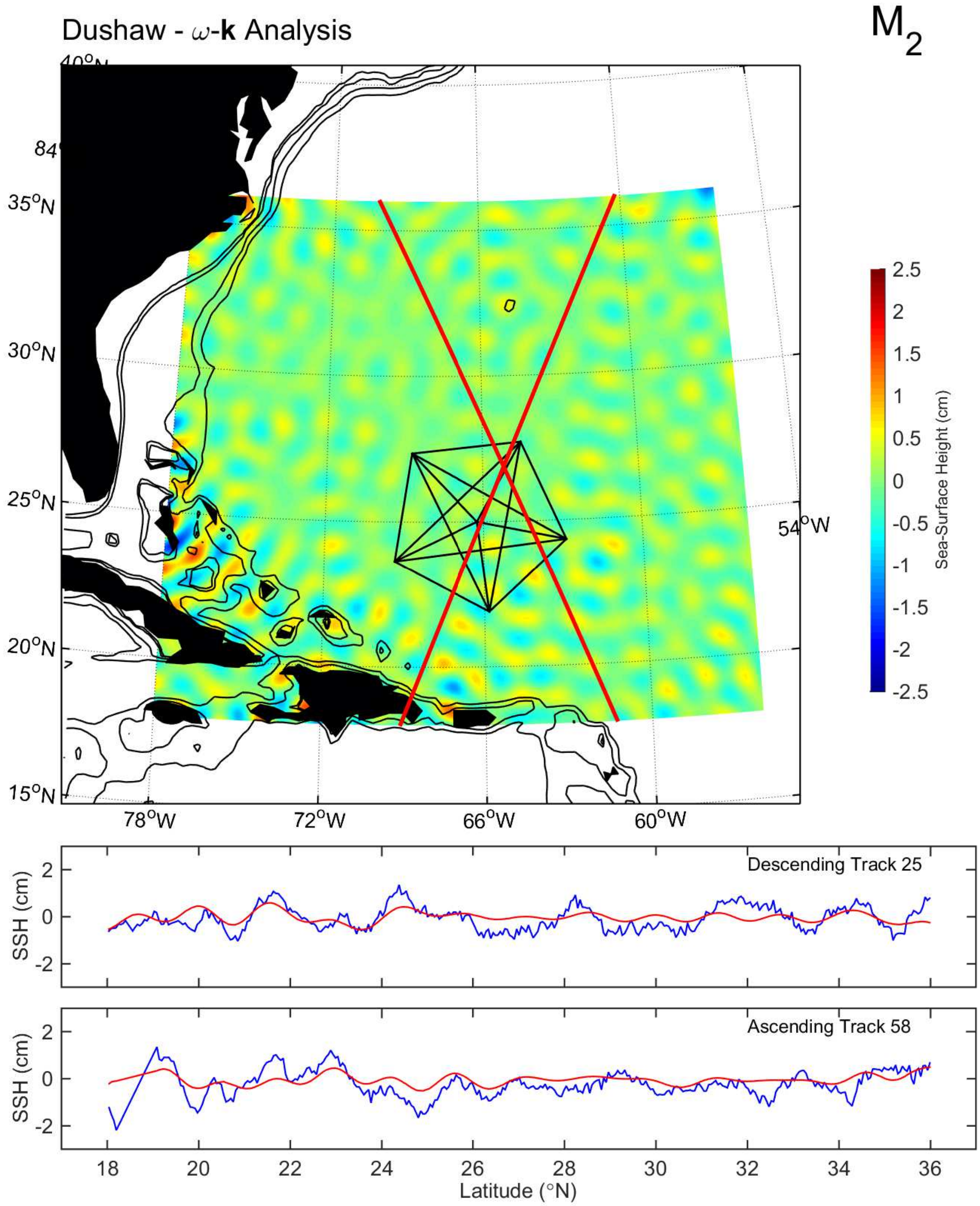

Figure 63. Sea-surface height for the estimated mode-1, M_2 internal tides in Sargasso Sea. In this region the semidiurnal and diurnal internal tides are rather weak. The pentagonal AMODE array (1990-1) is indicated. The bottom panels indicate along-track (blue) and frequency-wavenumber (red) tidal estimations along the ascending and descending tracks indicated in the top panel.

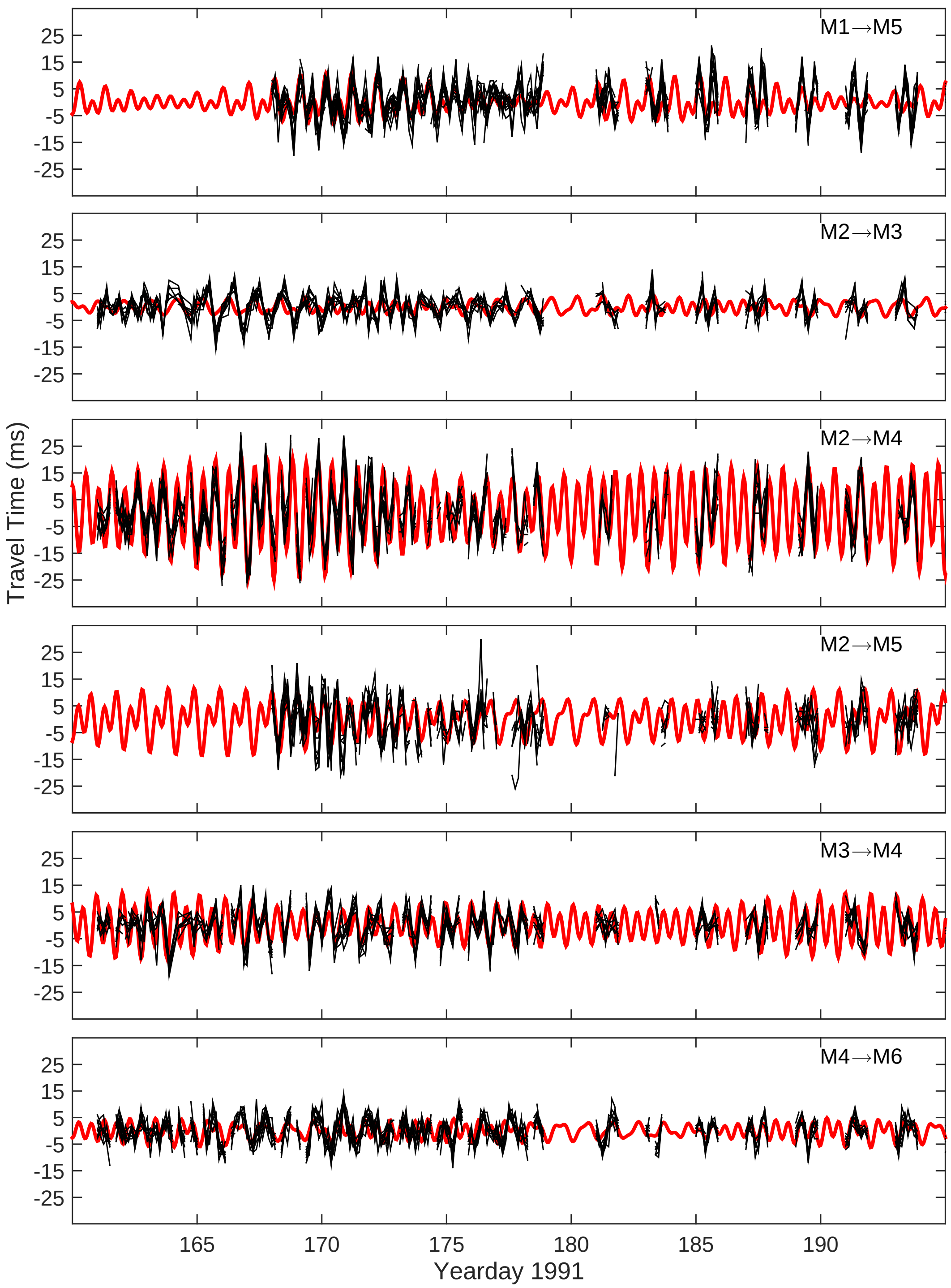

Figure 64. Comparison of measured (black) and predicted (red) travel time variations from mode-1 internal tides during the AMODE experiment. The measured travel times were not filtered, other than a simple high-pass filter to remove mesoscale signals. The predictions were derived using data from 2000-7, hence they represent a hindcast by about 12 years. Given the weakness of the tidal signals and the complex interference pattern from multiple wavetrains traveling through the region, the agreement between observations and predictions is extraordinary. At the upper right of each panel, the acoustic paths are indicated, with M1 being the northeasternmost mooring, mooring number increasing clockwise around the array, and M6 being the center mooring.

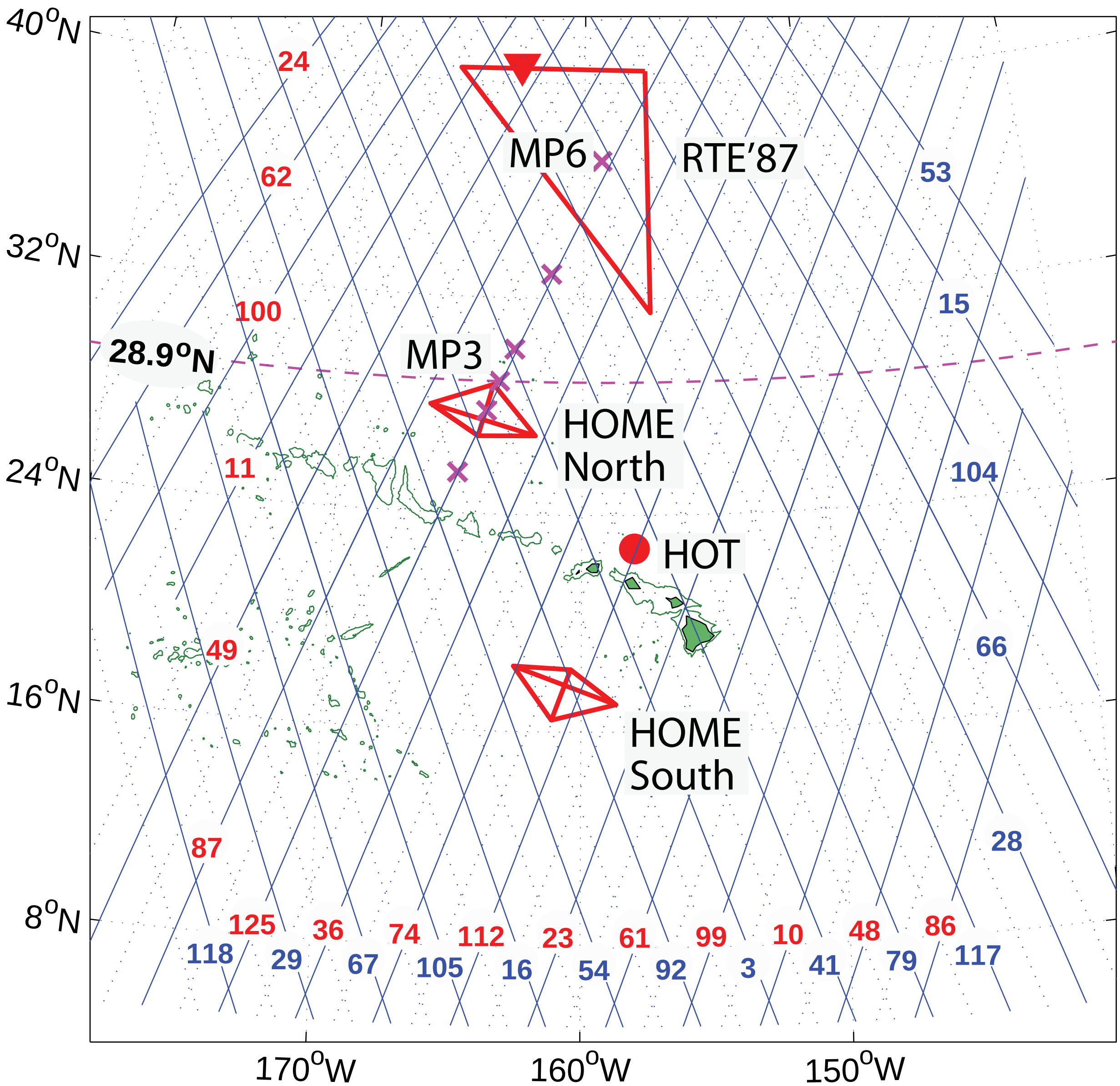

Figure 65. Summary of measurements of the internal tide around the Hawaiian Islands. Altimeter tracks are denoted by the blue lines, with tandem tracks denoted by the blue dotted lines. HOT denotes the Hawaiian Ocean Timeseries site. The large red triangle denotes the 1987 Reciprocal Tomography Experiment (RTE87), with a current meter and thermistor mooring denoted by the small solid red triangle. The two diamond shaped tomography arrays on either side of the Hawaiian Ridge were part of the Hawaiian Ocean Mixing Experiment (HOME) in 2000-2001. The magenta X's denote moorings deployed as part of the Internal Waves Across the Pacific (IWAP) experiment in 2006, labeled MP1–MP6. The dashed line along 28.9°N is the latitude of parametric subharmonic instability (PSI), a latitude at which enhanced dissipation of internal tides has been theoretically predicted.

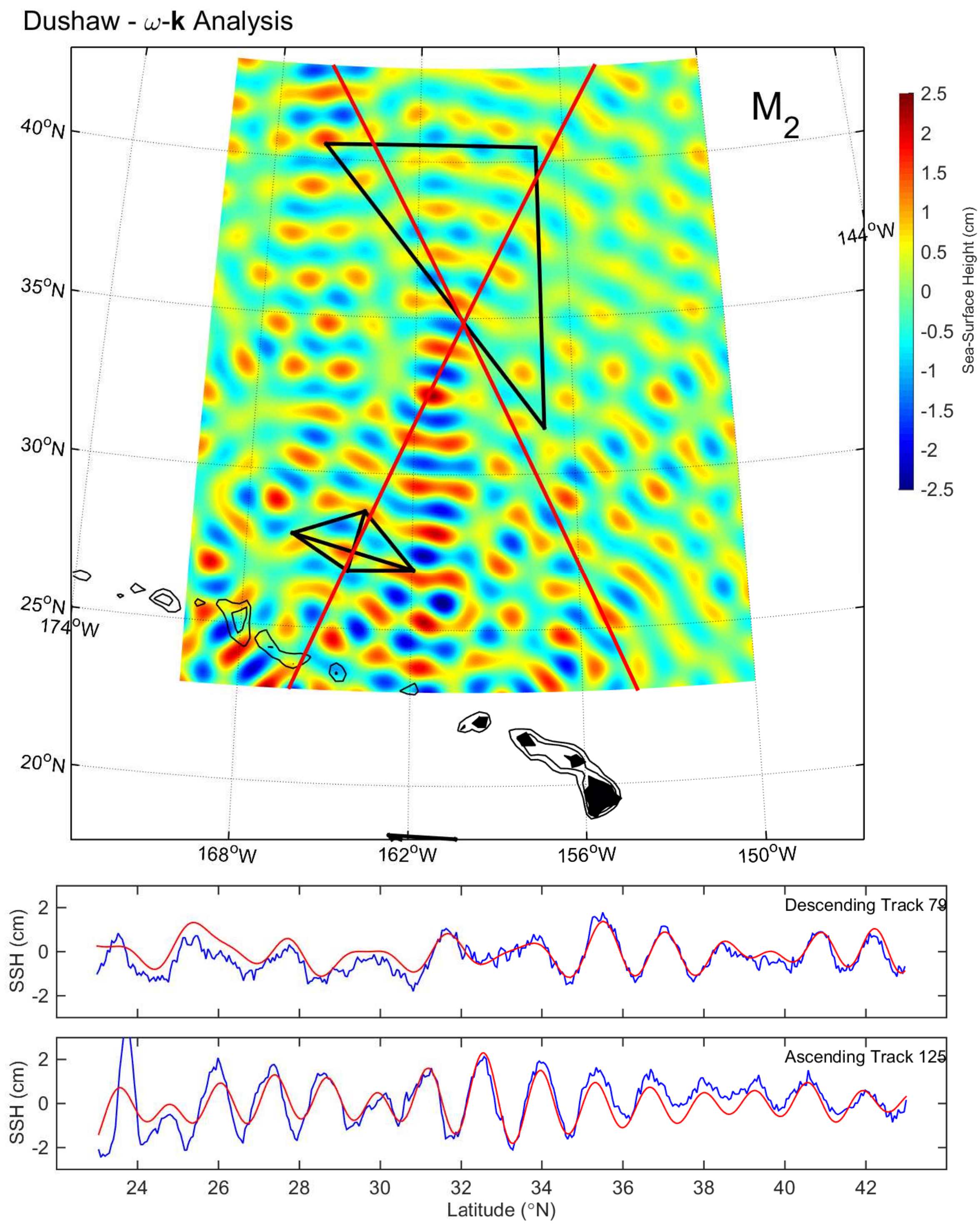

Figure 66. Sea-surface height for the estimated mode-1, M_2 internal tides north of Hawaii. In this region the semidiurnal and diurnal internal tides are about the strongest in the world. The triangular RTE87 array (1987 and the HOME northern array diamond (2001) are indicated. The bottom panels indicate along-track (blue) and frequency-wavenumber (red) tidal estimations along the ascending and descending tracks indicated in the top panel.

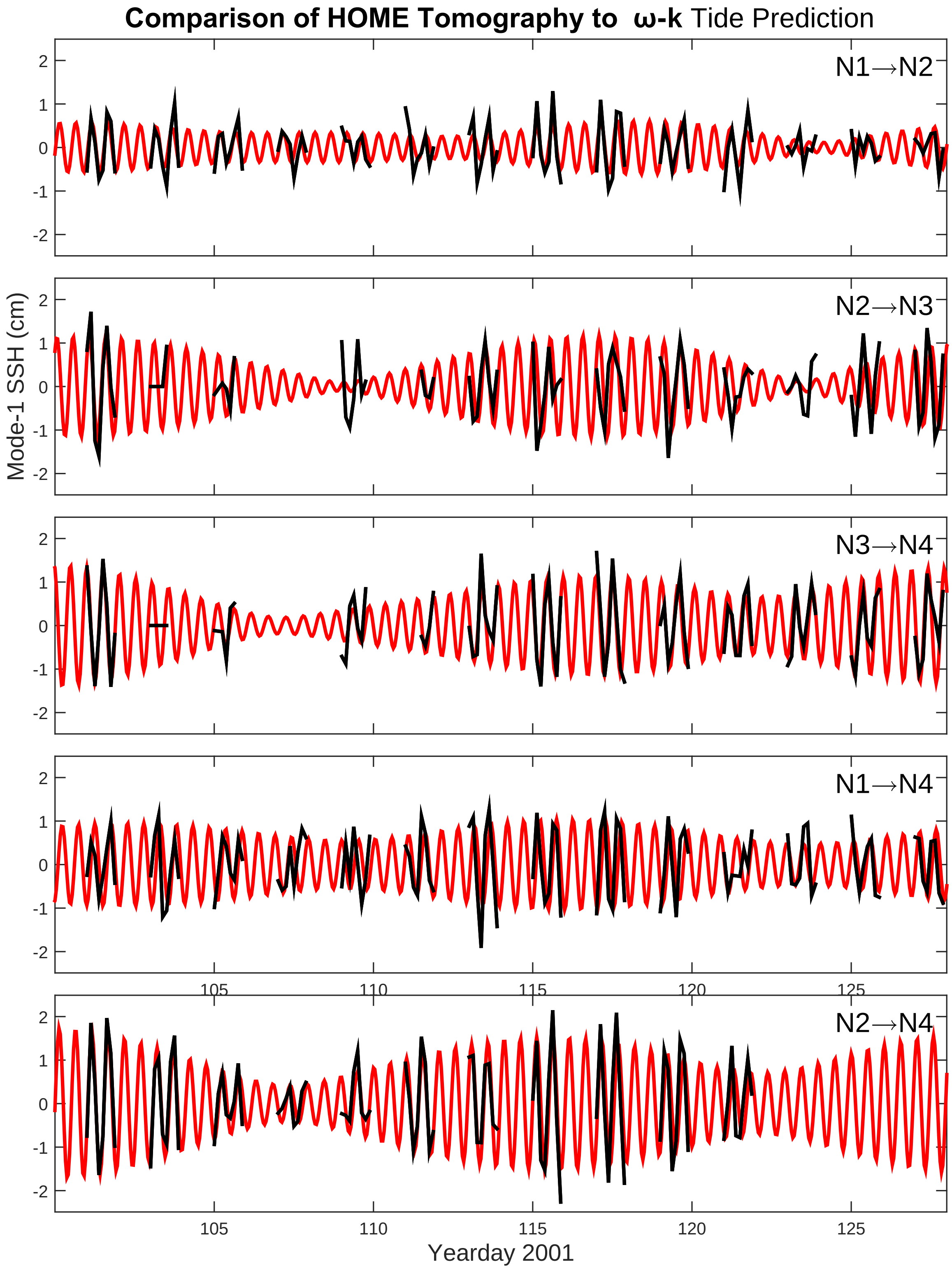

Figure 67. Comparison of measured (black) and predicted (red) sea-surface height variations from mode-1 internal tides during the northern HOME experiment. The measured sea-surface height variations were estimated by inverse of tomography travel times. These travel times were not filtered, other than a simple high-pass filter to remove mesoscale signals. The predictions were derived using data from 2000-7. At the upper right of each panel, the acoustic paths are indicated, with N1 being the northernmost mooring, mooring number increasing clockwise around the array.

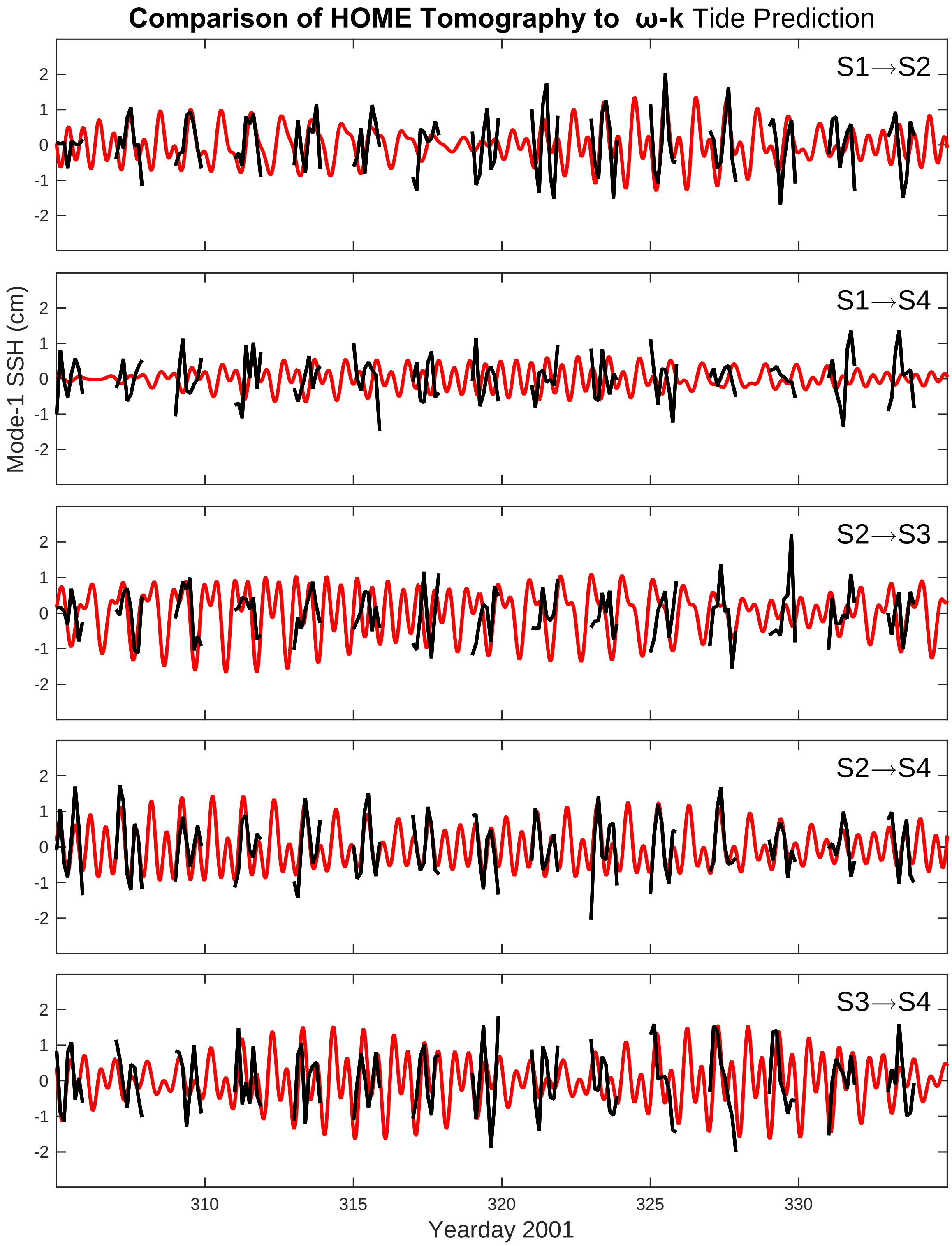

Figure 68. Comparison of measured (black) and predicted (red) sea-surface height variations from mode-1 internal tides during the southern HOME experiment, as in the previous figure. At the upper right of each panel, the acoustic paths are indicated, with S1 being the southernmost mooring, mooring number increasing clockwise around the array. The tidal signals to the south of Hawaii were weak; deriving accurate maps of these weaker signals is challenging.

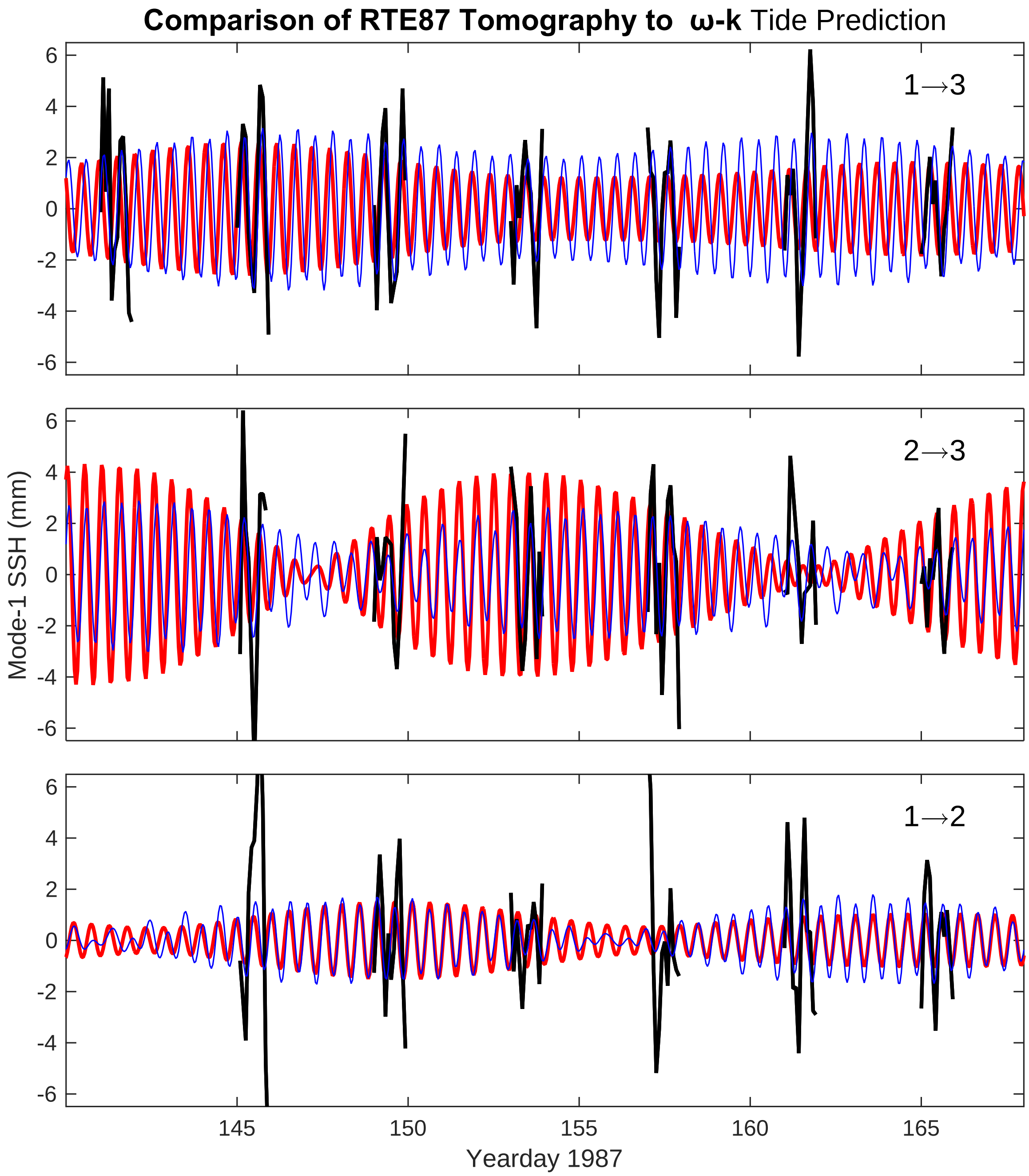

Figure 69. Comparison of measured (black) and predicted (red) sea-surface height variations from mode-1 internal tides during the RTE87 experiment. The measured sea-surface height variations were estimated by inverse of tomography travel times. Blue lines result from a tidal analysis of the tomography data, hence the apples-apples comparison is between the blue (measured) and red (predicted) time series. The predictions were derived using data from 2000-7, so the predictions represent a hindcast by about 15 years. At the upper right of each panel, the acoustic paths are indicated, with 1 being the northeasternmost mooring, mooring number increasing clockwise around the array. Path 1→2 is a meridional path, hence the signal on this path is realtively small. While excellent agreement between predictions and observations is found on path 1→2, a sign change has been applied to the predictions to obtain that agreement (see text).

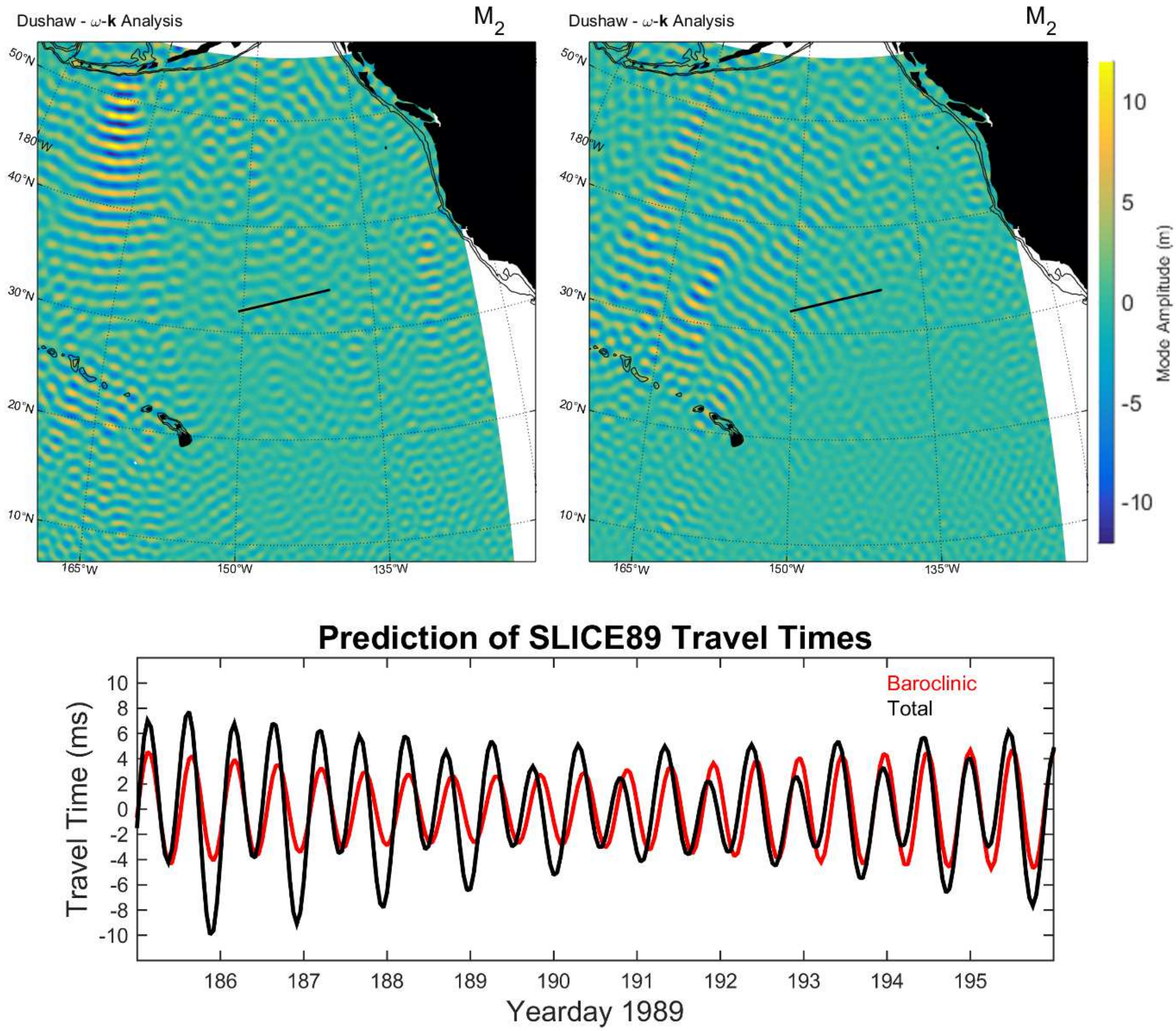

Figure 70. Prediction of tidal signals associated with the 9-day SLICE89 experiment. The top panels show the mapped internal tides using southward (left) and northward (right) wavenumbers. Southward wavenumbers likely contributed to the SLICE89 baroclinic tide signal. The lower panel shows the tidal predictions, with red corresponding to just the baroclinic tide and black corresponding to the total tidal signal. In this case the barotropic tidal signals, arising from ocean currents, contribute a signal comparable to the baroclinic signal.

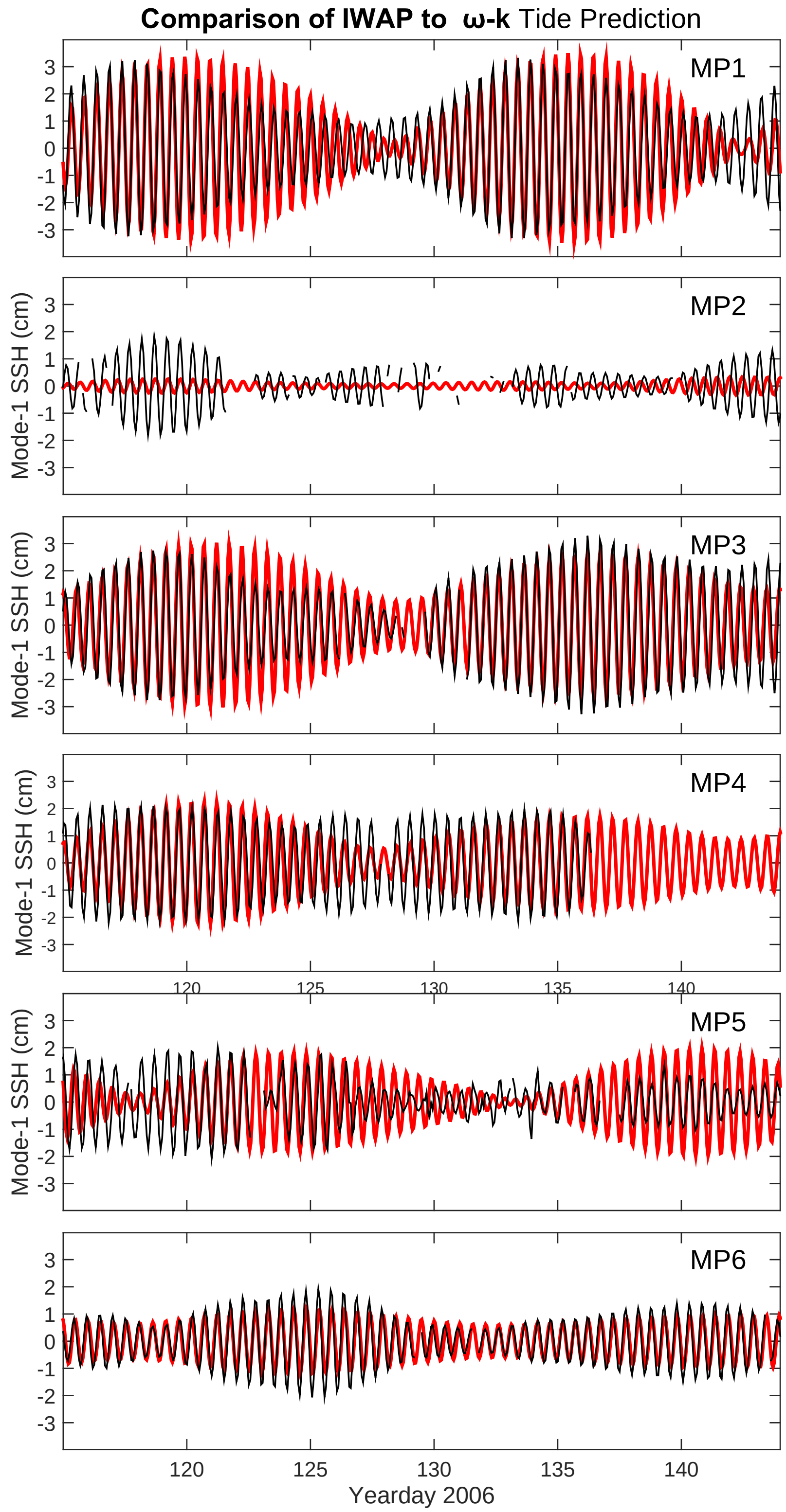

Figure 71. Comparison of measured (black) and predicted (red) sea-surface height variations from mode-1 internal tides during the 2006 IWAP experiment. The measured sea-surface height variations were estimated from moored profiler data by the IWAP collaboration. The IWAP mooring numbers are indicated at the upper right of each panel; MP1 was nearest to the Hawaiian Ridge. The frequency-wavenumber tidal analysis gives a much better prediction for mode-1 internal tides than the pointwise, along-track analysis employed by the IWAP collaboration.

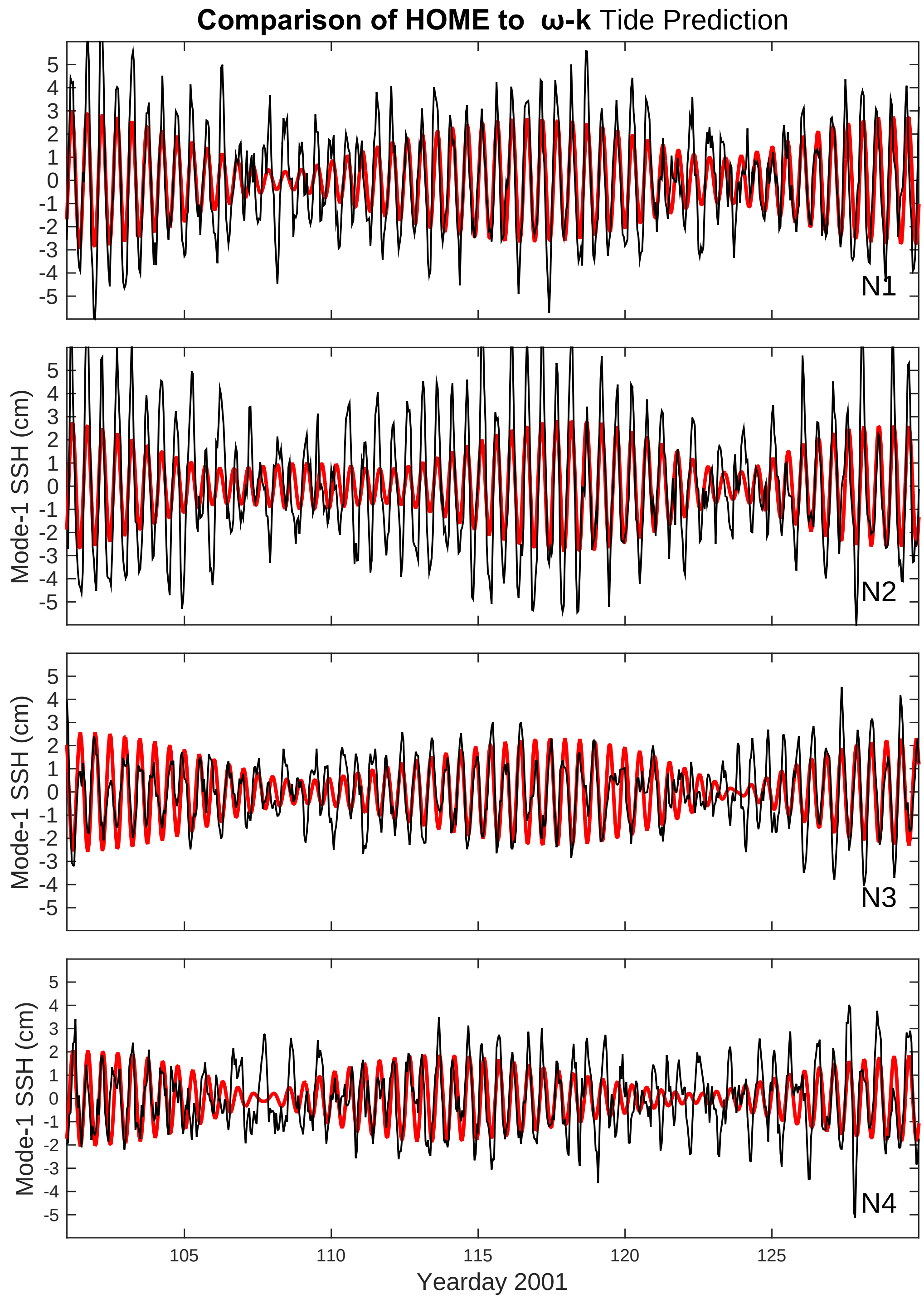

Figure 72. Comparison of measured (black) and predicted (red) sea-surface height variations from mode-1 internal tides during the 2001 HOME experiment. The measured sea-surface height variations were estimated from thermistor data obtained on each northern HOME tomography mooring. The tomography mooring numbers are indicated at the lower right of each panel. As noted by Dushaw et al. (2011), the in situ estimates appear to have larger amplitude than the predictions, unlike the comparisons to tomography. Only mooring N3 had vertical sampling that was adequate for distinguishing mode-1. The comparison here is much better than the earlier prediction of Dushaw et al. (2011), Figure 14.

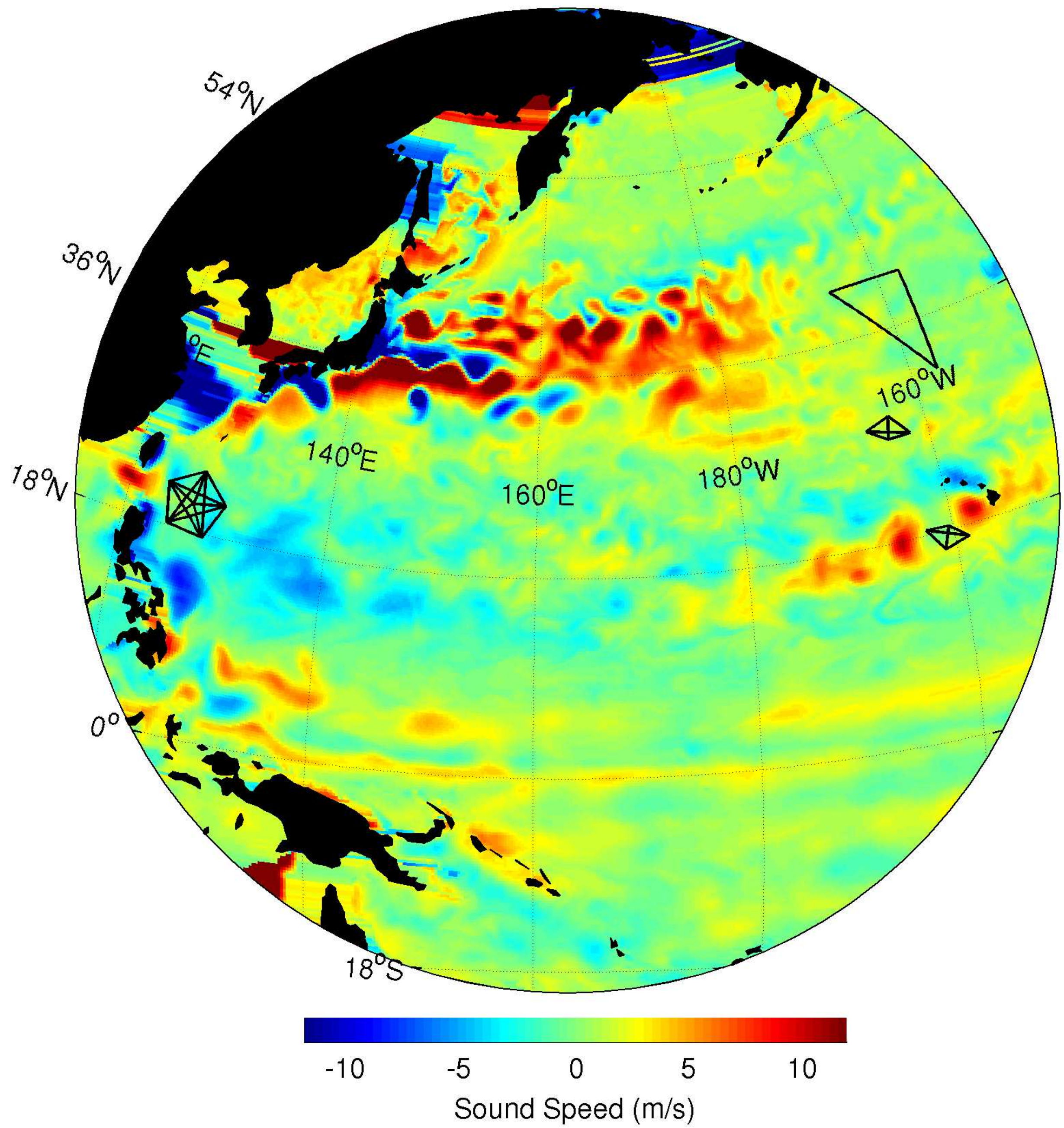

Figure 73. Sound speed at 300 m depth with climatological sound speed subtracted derived from the high resolution ECCO2 numerical ocean model (D. Menemenlis personal communication 2010, Dushaw et al. 2013). Since sound speed depends primarily on ocean temperature, the figure indicates relative mesoscale variabiity in the western Pacific Ocean. The RTE87 triangle and HOME diamond-shaped tomography arrays are indicated near Hawaii at right, while the 2010–2011 Philippine Sea pentagonal tomography array is indicated at left. The Philippine Sea is a region of fairly vigorous mesoscale variability, although this variability is comparable to that experienced south of Hawaii. The RTE87 array was in a region of quiescent mesoscale variability. All of these mesoscale features propagate westward, of course.

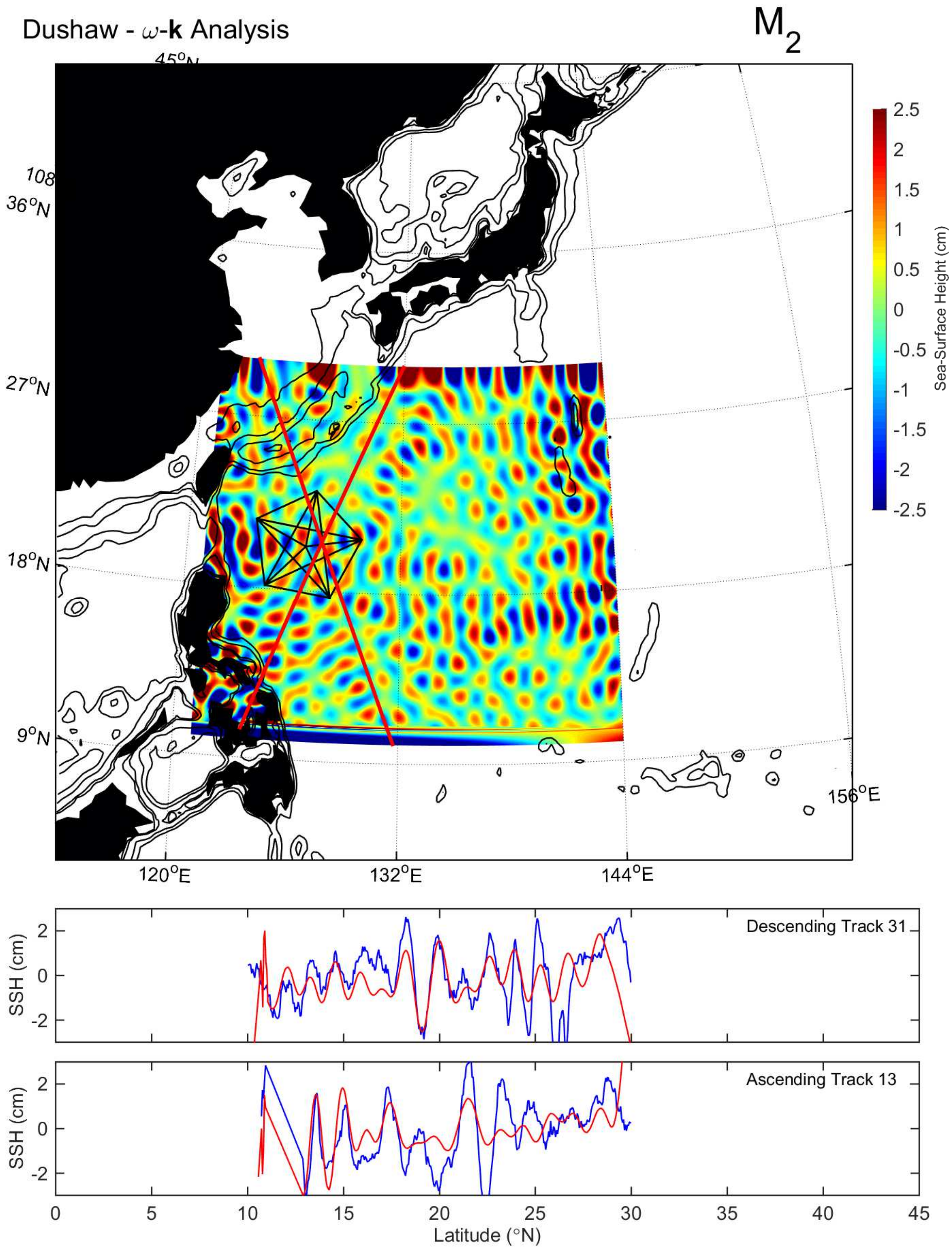

Figure 74. Sea-surface height for the estimated mode-1, M_2 internal tides of the Philippine Sea. In this region the semidiurnal and diurnal internal tides are both strong. The pentagonal tomography array was deployed in 2010–2011. The bottom panels indicate along-track (blue) and frequency-wavenumber (red) tidal estimations along the ascending and descending tracks indicated in the top panel.

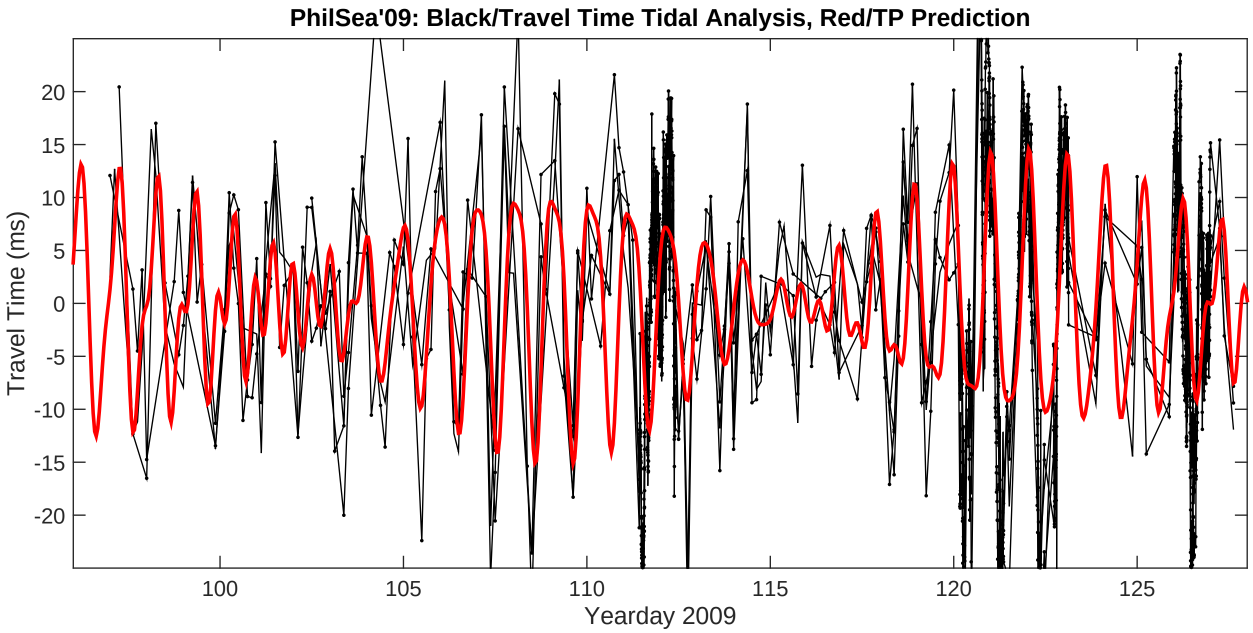

Figure 75. Preliminary comparison of tomography travel times measured in the Philippine Sea in 2009 to a prediction derived from the frequency-wavenumber tidal analysis. Only a single, short tomography path was available in this trial deployment. The tomography travel times are not filtered, other than a simple high-pass filter. Altimeter data from 2000-2007 were used to compute the prediction, hence the prediction is a forecast by about 4 years. This panels shows the complete 32-day record length of the 2009 timeseries. The six dominant tidal constituents are used for this prediction. The diurnal internal tides make significant contributions to the tidal variability in this region.

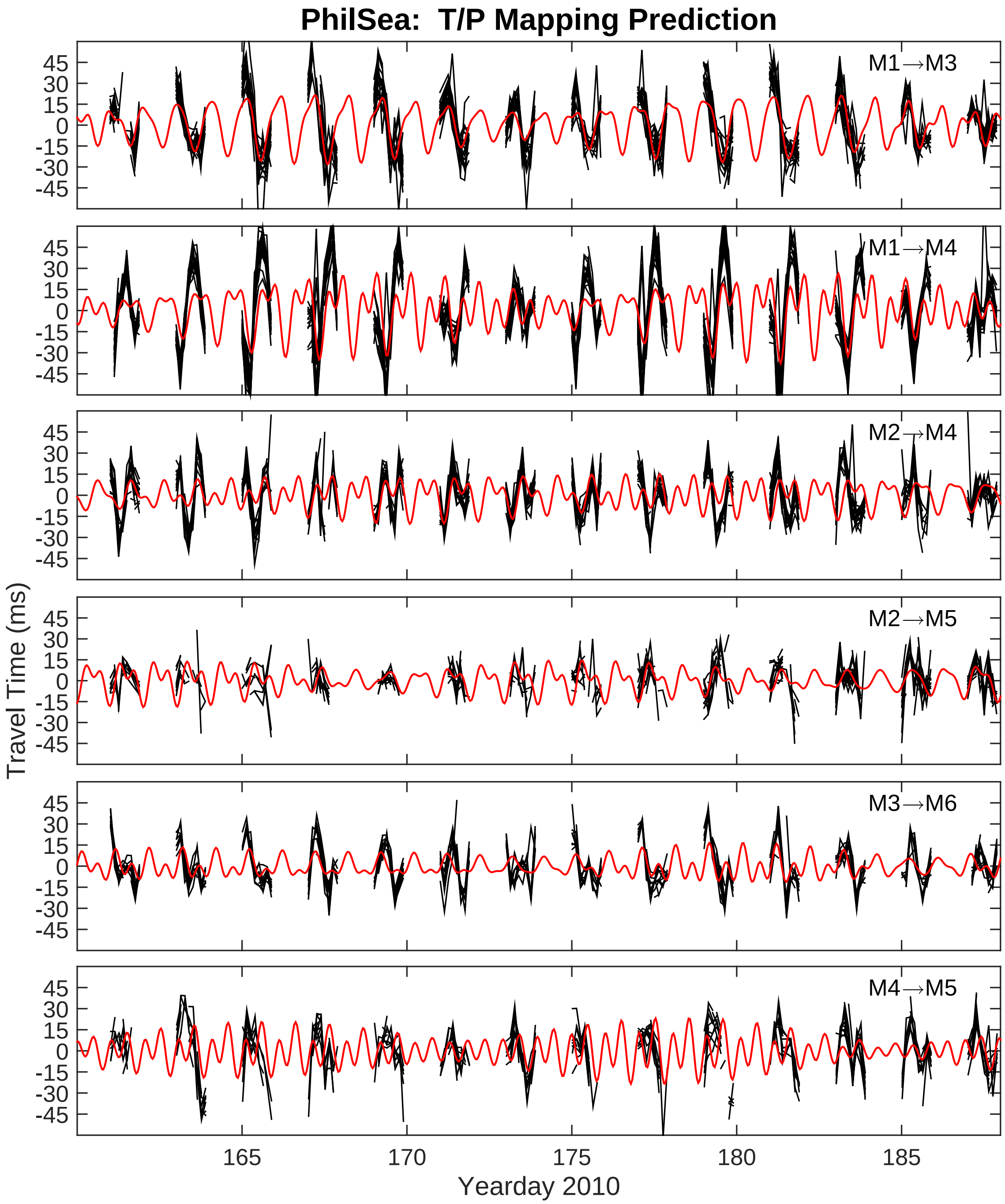

Figure 76. Preliminary comparison of tomography travel times measured in the Philippine Sea in 2010 to predictions derived from the frequency-wavenumber tidal analysis. The tomography travel times are not filtered, other than a simple high-pass filter. Altimeter data from 2000-2007 were used to compute the prediction, hence the prediction is a forecast by about 5 years. These panels show a 28-day time interval of the year long tomography timeseries. The six dominant tidal constituents are used for this prediction. Even in this complicated region the internal tides retain much of their coherence, but deriving accurate estimates from the altimetry data is challenging. At the upper right of each panel, the acoustic paths are indicated, with 1 being the northeasternmost mooring and mooring number increasing clockwise around the array.